This is to certify that the
dissertation entitled

STUDIES OF CURRENT-PERPENDICULAR-TO-PLANE MAGNETORESISTANCE (CPP-MR) AND CURRENT-INDUCED MAGNETIZATION SWITCHING (CIMS)

presented by

HUSEYIN KURT

has been accepted towards fulfillment
of the requirements for the

Ph.D. degree in Physics

Major Professor's Signature

9/29/05

Date

STUDIES OF CURRENT-PERPENDICULAR-TO-PLANE MAGNETORESISTANCE (CPP-MR) AND CURRENT-INDUCED MAGNETIZATION SWITCHING (CIMS)

By

Huseyin Kurt

A DISSERTATION
Submitted to
Michigan State University
in partial fulfillment of the requirements
for the Degree of

DOCTOR OF PHILOSOPHY

Department of Physics and Astronomy

2005

ABSTRACT

STUDIES OF CURRENT-PERPENDICULAR-TO-PLANE MAGNETORESISTANCE (CPP-MR) AND CURRENT-INDUCED MAGNETIZATION SWITCHING (CIMS)

By

Huseyin Kurt

We present two CPP-MR studies of spin-valves based upon ferromagnetic/ non-magnetic/ ferromagnetic (F/N/F) trilayers.

We measure the spin-diffusion lengths of N = Pd, Pt, and Au at 4.2K, and both the specific resistances (sample area A times resistance R) and spin-memory-loss of N/Cu interfaces. Pd, Pt and Au are of special device interest because they give perpendicular anisotropy when sandwiching very thin Co layers. Comparing our spin-memory-loss data at Pd/Cu and Pt/Cu interfaces with older data for Nb/Cu and W/Cu gives insight into the importance of spin-orbit coupling in producing such loss.

We reproduce and extend prior studies by Eid of 'magnetic activity' at the interface of Co and N-metals (or combinations of N-metals), when the other side of the N-metal contacts a superconductor (S). Our data suggest that magnetic activity may require strong spin-flipping at the N/S interface.

We present five studies of a new phenomenon, CIMS, in F1/N/F2 trilayers, with F1 a thick 'polarizing' layer and F2 a thin 'switching' layer.

In all prior studies of CIMS, positive current caused the magnetization of F2 to switch from parallel (P) to anti-parallel (AP) to that of F1– 'normal' switching. By judicious addition of impurities to F-metals, we are able to controllably produce both

'normal' and 'inverse' switching– where positive current switches the magnetization of F2 from AP to P to that of F1. In the samples studied, whether the switching is normal or inverse is set by the 'net polarization' produced by F1 and is independent of the properties of F2. As scattering in the bulk of F1 and F2 is essential to producing our results, these results cannot be described by ballistic models, which allow scattering only at interfaces.

Most CIMS experiments use Cu as the N-layer due to its low resistivity and long spin-diffusion length. We show that Ag and Au have low enough resistivities and long enough spin-diffusion lengths to be useful alternatives to Cu for some devices.

While most technical applications of CIMS require low switching currents, some, like read-heads, require high switching currents. We show that use of a synthetic antiferromagnet can increase the switching current.

Manschot et al. recently predicted that the positive critical current for switching from P to AP could be reduced by up to a factor of five by using asymmetric current leads. In magnetically uncoupled samples, we find that highly asymmetric current leads do not significantly reduce the switching current.

A CIMS equation given by Katine et al. predicts that lowering the demagnetization field should reduce the switching current. To test this prediction, we compare switching currents for Co/Au/Co(t)/Au nanopillars with t = 1 to 4 nm (where the easy axis should be normal to the layer planes at least for t=1 and 2 nm) with those for Co/Cu/Co(t)/Au nanopillars (where the easy axis should be in the layer planes). We do not find significant differences in switching currents for the two systems.

To my parents

ACKNOWLEDGEMENTS

I would like to thank my thesis advisor professor Jack Bass for his professional guidance and assistance. I would also like to thank professor William Pratt Jr. for his assistance in my experiments, technical teachings and instrument designing. I am honored to work with both Dr. Bass and Dr. Pratt.

My special thanks to Dr. Reza Loloee for his help and technical support. I owe most of my experimental and technical expertise in thin films and vacuum systems to Reza.

I would like to thank my friends and colleagues Antonio Zambano, Ion Moraru, Khalid Eid, Michael Crosser, Mustafa Al-Haj Darwish, and Sergei Urazhdin for their friendships, help and suggestions. Each of them made my life in the basement of BPS building enjoyable and memorable.

I want to thank Thomas Palazzolo for setting up a machine shop class, in which I learned the basics of machining and designing. I also want to thank the machine shop crew Thomas Hudson and James Muns for helping me design and make some instruments I built.

Finally I would like to acknowledge the financial support of MSU CFMR, CSM, Keck Microfabrication Facility, NSF Grants No. DMR 02-02476, No. 98-09688 and Seagate Technology for the research presented in this thesis.

Contents

List of Figures

List of Tables

Chapter 1

Introduction

1.1 Homogenous metals

Magnetoresistance (MR) is defined as the percentage change in the resistance of a conductor in response to an external magnetic field H. The MR for a homogenous conductor is usually defined as;

$$MR(\%) = \left[\frac{R(H) - R(0)}{R(0)}\right] \times 100, \tag{1.1}$$

where $R(H)$ is the resistance in H and $R(0)$ is the resistance in zero magnetic field.

For normal (N) metals or alloys, the external magnetic field exerts a Lorentz force on the conduction electrons that gives rise to a change in resistance, in which the resistance increases with increasing H [1, 2]. This effect is known as Lorentz MR. Lorentz MR increases with H^2 at small fields (where the electrons are scattered many times before completing a cyclotron orbit) and can level off or continue to grow at high fields (where electrons complete several cyclotron orbits between scattering events). For N-metals or alloys the MR is typically less than 0.1% at room temperature at $H = 1$T [3]. However, for high purity compensated metals, where the numbers of electrons and holes are the same, the Lorentz MR increases indefinitely with H^2 at very low temperatures[4]. Since it is large only in very pure metals and at very low

temperatures, it is impractical to use in devices.

Ferromagnetic (F) metals or alloys, on the other hand, display a different kind of MR, which depends on the angle between the current and H [5]. This effect is called anisotropic MR (AMR)and arises from the spin-orbit coupling of electrons in F-metals [6]. The AMR for a thin film of the alloy permalloy (Py=$Ni_{0.8}Fe_{0.2}$) is relatively large ($\sim 2\%$) at room temperature in a small field of ~ 10 Oe. Due to this 2% MR, Py films were used in the read heads of hard drives until the introduction of "Giant Magnetoresistive" read heads in 1997 [7].

1.2 Giant Magnetoresistance (GMR) in Magnetic Multilayers

GMR was discovered in 1988 in epitaxially grown, antiferromagnetically coupled, Fe/Cr/Fe trilayers [8] and Fe/Cr multilayers [9], in which the magnetizations of the Fe layers were aligned anti-parallel (AP)(Fig. 1.1(a)) at zero field due to the antiferromagnetic exchange coupling [10]. As shown in Fig. 1.2, the resistances of such Fe/Cr samples decrease as the moments of the Fe layers aligned parallel (P) (see Fig. 1.1(b)) upon applying a high enough field. A dramatic reduction (up to 50% at 4.2K) in the resistances of these samples was observed. This big reduction in the resistances of the Fe/Cr multilayers led to the name "Giant" Magnetoresistance.

GMR depends on the relative orientation of the magnetizations of the F-metals separated by an N-metal and results from spin polarization in the bulk F layers and at the F/N interfaces [11, 12]. The MR for F/N multilayers or F/N/F trilayers is

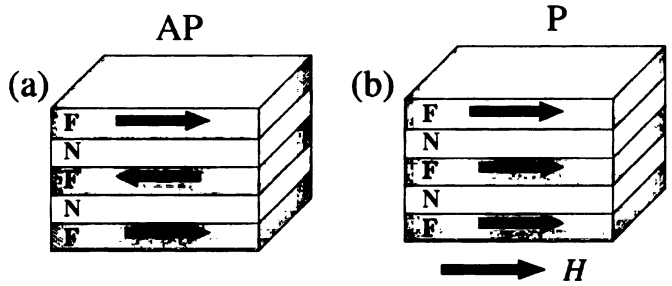

Figure 1.1: (a) Antiferromagnetically coupled F/N multilayer, where the local magnetizations lie antiparallel in the absence of magnetic field H (b) At high H the magnetic moments are aligned parallel along H.

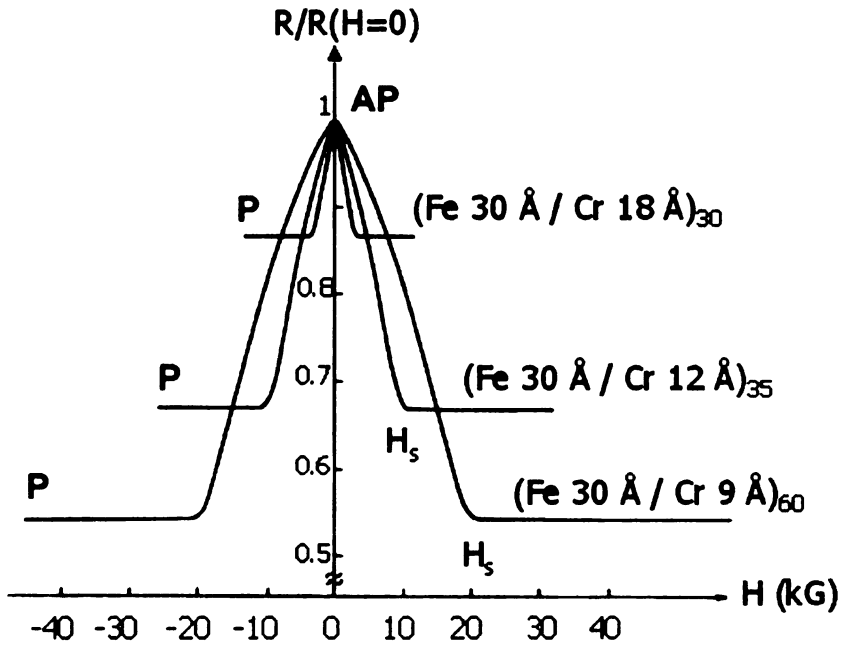

Figure 1.2: The resistance vs. H graph for Fe/Cr multilayers by Baibich et al. [9]. The resistance decreases as the external field increases.

usually defined as;

$$MR(\%) = \left[\frac{R(AP) - R(P)}{R(P)}\right] \times 100, \tag{1.2}$$

where $R(AP)$ is the resistance in the anti-parallel (AP) state, and $R(P)$ is the resistance in the parallel (P) state. GMR is usually positive (normal) i.e. the resistance is higher in the AP state, but, as we shall see below, there are cases in which GMR

can be negative (inverse). Theoretical explanations for the sign of GMR will be given in Chapter 2.

1.2.1 Producing P and AP states

P states can be easily achieved by increasing the external magnetic field H to above the saturation field(s), H_s, of the F-metals or alloys. AP states however are harder to achieve for wide ranges of thicknesses of both F and N-metals. For AP states to be achieved, either adjacent F-layers must be antiferromagnetically coupled or their switching fields must be different. This can be done in 3 ways:

1. Using antiferromagnetically coupled F-metals. The exchange coupling between two F-metals separated by an N-metal oscillates with increasing N-metal thicknesses between ferromagnetic coupling (which aligns the magnetizations of the two F-metals in the same direction) and antiferromagnetic coupling (which aligns the magnetizations in opposite directions). The strength of the coupling decreases with increasing thickness of N and becomes negligible beyond a certain thickness [13, 14].

2. Using an exchange-biased spin valve (EBSV) in which one of the F-metals is in contact with an antiferromagnetic (AF) metal. A simple EBSV has the form AF/F1/N/F2, where F1 and F2 can be same or different and N is thick enough so that exchange coupling between F1 and F2 is negligible. Heating the sample to above Néel temperature of the AF-metal and cooling in the presence of a high enough external field H can pin F1 due to the strong exchange interaction between AF and F1 . The hysteresis loop of the pinned F1 shifts away from

$H = 0$, changing its switching field dramatically [15, 16]. Therefore F1 and F2 can have very different switching fields. This configuration enables the free layer to switch back and forth over many cycles while the pinned layer stays fixed. For this reason, EBSVs are used in read heads of hard drives.

3. Using a hybrid spin valve, with two F-metals separated by a thick N-metal layer, one can achieve an AP state in two ways:

   - Using different F-metals with different switching fields.
   - Using one type of F-metal with different thicknesses, giving different switching fields.

1.2.2 Current directions in multilayers

There are two main geometries for current flow direction used in GMR experiments.

- Current-in-plane (CIP), in which the current flows parallel to the plane of the layers as in Fig. 1.3. The MR for this geometry is called "CIP-MR".
- Current-perpendicular-to-plane (CPP) geometry, in which the same current flows through every layer as in Fig. 1.3. The MR for this geometry is called "CPP-MR".

Both in the CIP-MR and CPP-MR experiments the external magnetic field is usually applied in the plane of the samples as shown in Fig. 1.3.

Consider a metallic thin film with dimensions of $l = 1$ cm, $w = 1$ mm and $t = 100$ nm and resistivity of 200 nΩm. If the current flows through the area wt, the CIP

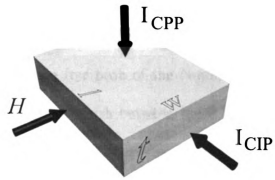

Figure 1.3: Different current flow directions for multilayers, H is applied in-plane. CIP current flows through area $A = wt$ and CPP current flows through area $A = wl$.

resistance is;

$$R_{CIP} = \rho\frac{l}{wt} = 200\text{n}\Omega\text{m} \cdot \frac{10^7\text{nm}}{10^6\text{nm} \times 100\text{nm}} = 20\Omega \tag{1.3}$$

and the CPP resistance is;

$$R_{CPP} = \rho\frac{t}{wl} = 200\text{n}\Omega\text{m} \cdot \frac{100\text{nm}}{10^7\text{nm} \times 10^6\text{nm}} = 2\text{n}\Omega \tag{1.4}$$

The CIP resistance of this film is much larger than its CPP resistance. Resistances of ohms can easily be measured using a current source and either a lock-in amplifier or a digital voltmeter. On the other hand, measuring resistances of nanoohms requires a sophisticated measurement setup including a superconducting quantum interference device (SQUID) [17] or a low temperature ac amplifier [18]. The CPP resistance of a metallic sample can be on the order of ohms if the sample area is reduced to smaller than $0.01\mu\text{m}^2$, which can be done using lithography (see Section 3.2) or making F/N multilayer nanowires [19, 20, 21] . The early studies of GMR were done using the CIP geometry [9, 8], because CIP resistances are easier to measure for thin films. For the same reason, today's GMR devices use CIP geometry.

Theoretically CIP-MR is more complex than CPP-MR due to the complications in the distribution of current through the layers and there are more parameters involved, including especially the mean free path of the N-metal [11]. GMR is only possible if the electrons are able to distinguish between the P and AP states of the F-layers, which requires the electrons to travel between different F-layers without losing their spin polarization. Thus, for CIP-MR the thicknesses of the N-layers separating the F-layers should not be much longer than their respective mean free paths. Current flow in the CIP geometry is non-uniform and also complicated, i.e. more current passes through lower resistivity layers. Since our research doesn't involve CIP-MR we won't go into further details, referring the interested reader to Ref. [11].

Since the same current passes through every layer in the CPP geometry, there turn out to be fewer parameters involved, making it easier to analyze the experimental data and derive the underlying physics [22, 23, 12, 24]. The first CPP-MR experiments were done by our group by using crossed superconducting Nb strips as leads to get a uniform current flow through a sample [25]. All measurements in this thesis are done using CPP currents. We can divide the theories of CPP-MR into two categories.

1. Free-Electron Based Models: Semi-classical models neglecting Fermi surface effects in F and N layers and at F/N interfaces.

2. Realistic Fermi Surface Models, which take the different Fermi surfaces of the constituents of an F/N system into account.

These theoretical models will be reviewed in Chapter 2.

1.2.3 GMR device applications

The discovery of GMR stimulated great interest in spin-dependent electronics and physics, nowadays called "spintronics", which has the potential to change the present technology based on only charge transport.

Different uses of GMR sensors include determining the speed and position of electric motor shafts, general field detection in implantable medical devices, and wheel speed sensing for ABS brake applications [26]. But their biggest industrial application is as the read heads of hard drives, where they opened a new era in the field of high density magnetic storage. In 1997 IBM introduced the first GMR read head in hard drives [27] with 6% MR which replaced the AMR (2% MR) read heads. Higher MR of these first GMR read heads allowed higher areal densities (3 Gbits/in^2) of bits on a hard disk. Further increases in the areal densities are achieved by improving the MR of the GMR read heads.

Conventionally, the magnetic bits are recorded in the plane of the disk (Fig. 1.4 (a)). A new method of magnetic recording suggests storing the bits in perpendicular magnetic domains which allows more dense packing of bits (see Fig. 1.4 (b)). In December 2004 Toshiba announced the first commercial hard drive using perpendicular recording with an areal density of 133 Gbits/in^2 [28]. More research is under way to increase the areal densities beyond 1 Tbits/in^2 [29, 30, 28].

As the areal densities on a hard disk continue to increase, more sensitive read heads are needed to detect weaker magnetic fields from smaller bits. Today's modern hard drives use CIP-MR read heads. It has been shown that CPP-MR could be

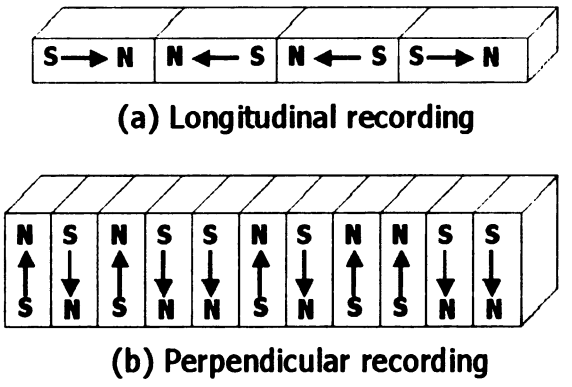

Figure 1.4: A representative cartoon of (a) longitudinal and (b) perpendicular recording. Perpendicular recording allows much higher areal densities.

several times larger than the CIP-MR of the same structures [25, 31, 32], and thus could be used for more sensitive read heads. However, for the CPP-MR devices with standard metals or alloys to have big enough resistances for read heads, the area of the devices should be smaller than $0.01\mu m^2$.

1.3 Spin Transfer Torque & Current-Induced Magnetization Switching

In 1996 Slonczewski [33] and Berger [34] independently predicted that a polarized high-density CPP current could produce a spin-transfer-torque (STT) on the magnetization of a nanomagnet (a thin (1-10 nm thick) ferromagnet with $\lesssim$ 100 nm lateral dimensions). Such STT acting on the magnetization of a nanomagnet is predicted to produce a steady precession of magnetization upon applying a high enough current in a high enough external magnetic field, and a novel type of magnetization switching upon applying a current higher than the threshold. Slonczewski focused on switching of that layer's magnetization and Berger focused upon excitation of coherent magnons, but subsequent works showed that their models were almost equivalent

[35, 36]. For simplicity, we focus mostly on the Slonczewski analysis and outgrowths thereof.

Slonczewski [33] proposed a trilayer system of F1/N/F2, where F1 is a thick ferromagnet with magnetization $\mathbf{M_1}$ (therefore its magnetization doesn't flip with current), N is a nonmagnetic spacer thinner than its spin-diffusion length, and F2 is a thin nanomagnet with magnetization $\mathbf{M_2}$ with $\lesssim 100$ nm lateral dimensions. When electrons pass through F1 they get polarized, therefore carry angular momentum. If $\mathbf{M_2}$ is non-collinear with $\mathbf{M_1}$, the electrons polarized by F1 and transmitted into F2 exert a torque (spin-transfer-torque or STT) on $\mathbf{M_2}$ in an azimuthal direction to align or anti-align $\mathbf{M_2}$ with $\mathbf{M_1}$. If a current greater than a threshold ($\sim 10^{7-8}$ A/cm^2) is applied, $\mathbf{M_2}$ flips. For the current applied in the opposite direction, the electrons transmitted into F1 cannot flip $\mathbf{M_1}$ because F1 is thick, but the electrons reflected from the F1/N interface can flip $\mathbf{M_2}$ when they are injected back into F2. This gives an asymmetric switching because only $\mathbf{M_2}$ can be flipped. Due to the relative alignments of $\mathbf{M_1}$ and $\mathbf{M_2}$ (P or AP), the resistance of the trilayer system changes as the alignments change from P to AP or vice versa, just like in the case of GMR, but with a different switching mechanism, in which the relative alignments of magnetizations are determined by the direction of the current flow. This phenomenon is now called "Current-Induced Magnetization Switching (CIMS)".

In 1998, Tsoi et al. for the first time, experimentally observed the effect of STT by measuring the variations in the resistance of a Co/Cu multilayer, induced by a high current density $\approx 10^8$ A/cm^2 injected into the multilayer through a mechanical point contact [37]. The precession of magnetization by STT has opened a new field of dc-

generated GHz spin waves, which has potential uses in high-frequency communication devices. We won't go into details of the microwave studies, as they are irrelevant to the present thesis, referring the interested reader to some appropriate papers [38, 39, 40, 41, 42, 43].

In 1999, Sun reported the first magnetic switching in a trilayer manganite junction [44] and then Myers et al. reported the first measurements showing a magnetization reversal using lithographically defined point contacts to a Co/Cu/Co trilayer [45]. In 2000, Katine et al. [46] reported the first magnetization reversal in Co/Cu/Co nanopillar devices fabricated by electron beam lithography. Later, several groups fabricated nanopillars, reproducing and extending the results of Katine et al. (see e.g. refs. [47] and [36]). At MSU we fabricate our nanopillars in such a way that both dipolar and exchange couplings are minimal, which are referred to as 'magnetically uncoupled nanopillars' in this thesis. The details of the fabrication of our nanopillars are given in Chapter 3.

The discussion so far has neglected any applied magnetic field, H. In the absence of H, the magnetization of the switching layer F2 reverses at a positive current I_s^+ from parallel (P) to that of F1 to AP to that of F1, and at a (not necessarily the same magnitude) negative current I_s^- from AP to P. A large H in either direction tends to drive the F1/N/F2 nanopillar to the P state. Increasing-magnitude negative H and negative I reinforce each other in driving the system to a P state. As shown schematically in Fig. 1.5, for increasing-magnitude negative I, the switching fields gradually decrease in magnitude until a certain value of I, after which the system stays in the P state for all larger-magnitude I and all H. For increasing positive I,

in contrast, the current and field tend to oppose each other. For a given H, large enough I should eventually drive the system to the AP state. But for large fixed I, increasing H beyond a certain value is found to drive the system from the AP state to a 'between' (B) state involving excitation of one or more magnons. Urazhdin et al. [48] showed that, in the vicinity of the AP to B transition, the system displays telegraph noise, and a peak in dV/dI that is located approximately where the rates for switching from the AP to B state and vice versa become equal.

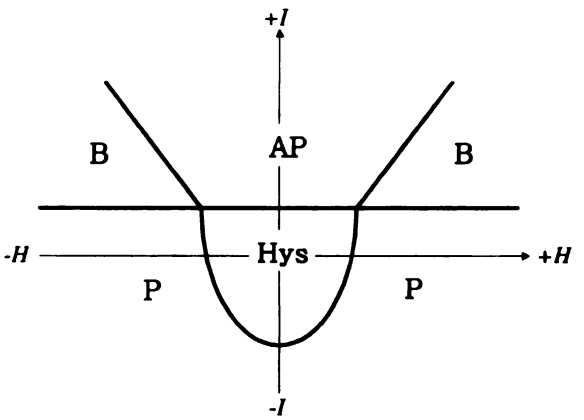

Figure 1.5: A schematic phase diagram of a magnetically uncoupled nanopillar. The regions of hysteretic switching (Hys), parallel (P), antiparallel(AP) and 'between'(B) are labeled.

A phase diagram of H vs. I is obtained by measuring MR at different currents and measuring CIMS at different external fields. This diagram allows one to easily distinguish between the regions of no switching, switching and precession. In this thesis we only studied the MR at zero current and CIMS at zero (or very low) field.

All of the CIMS experiments in this thesis use the F1/N/F2 trilayer geometry just described, in which F1 generates the polarized current that exerts a torque on the magnetization of F2, thereby generating magnetic excitations. In 2001, Heide [49, 50, 51] predicted that such excitations could be produced without the polariz-

ing ferromagnet, albeit only at larger exciting currents. Using a mechanical point contact, Ji et al. [52] observed spin-wave excitations in single Co layers for electrons flowing only from the tip into the Co film in the presence of very high (2-9 Tesla) external fields applied perpendicular to the layers for currents $\sim 5 \times 10^9$ A/cm^2. However, their critical currents were higher for thicker F-layers, inconsistent with Heide's model. Ji et al. explained their excitations adapting Slonczewski's model to a single F-layer [38], defining two regions in the F-layer, a region near the contact where serves as the free layer and the rest of the layer which remains aligned with the external field and serves as the fixed layer. Polianski and Brouwer [53] and Stiles et al. [54] subsequently argued that an unpolarized current injected from an N-metal into an F-metal can produce STT excitations for one polarity of current, provided that the nonmagnetic contacts to the F-layer are asymmetric. Ozyilmaz et al. [55] reported current-induced excitations in single Co layer nanopillars with asymmetric (Cu(thin)/Co/Cu(thick)) leads for only one current polarity, currents $\sim 10^9$ A/cm^2, and fields > 1.5 T perpendicular to the sample plane. Similar currents produced no excitations in nanopillars with symmetric leads. Excitations in single F-layers are also outside the scope of the present thesis.

We conclude this introduction by noting that CIMS has several potential technological applications, mainly in non-volatile magnetic random access memories (MRAMs). Using CIMS devices in MRAMs has the advantage that they don't require an external magnetic field for switching. However, the high critical switching currents of present devices make them inappropriate for MRAMs due to self-heating. For CIMS devices to be used in MRAMs, the switching currents should be reduced to $\sim 10^{5-6}$ A/cm^2

[56]. Therefore much of the research on CIMS aims to reduce the switching currents. Another possible technological application is to use nanopillars as read heads of hard drives. Since the nanopillars are very small, the current used to measure the resistance of a nanopillar might switch the magnetization of the free layer or at least generate noise. This problem can be solved by increasing the currents needed for switching. Chapter 8 discusses a means of increasing the switching currents by reducing the net spin polarization of the polarizing layer.

1.4 This thesis

We briefly describe the theoretical models of CPP-MR and CIMS in Chapter 2. Chapter 3 describes the experimental techniques and procedures we used to fabricate and measure our samples. The fabrication of nanopillars is given in detail.

In Chapter 4 we describe CPP-MR experiments involving spin-memory-loss at 4.2K in sputtered Pd, Pt, Au and at their interfaces with Cu to see whether these materials could be used in devices without significant spin-memory-loss. We also compare our results with previously published data to understand the effect of spin-orbit interaction in spin-memory loss.

In Chapter 5 we describe a new phenomenon initially observed by Eid [57], which involves changes in magnetic scattering anisotropy at a ferromagnetic/superconducting (F/S) interface. We extend his measurements to include new metals and alloys, and combinations of metals and alloys to try to understand the source of such changes in the scattering anisotropies.

In Chapter 6 we describe experiments involving normal and inverse CIMS or MR

to investigate the effect of positive and negative bulk and interface anisotropies.

In Chapter 7 we compare the switching currents and MRs of nanopillars with Cu, Ag and Au spacers to see if Ag and Au are potential competitors of Cu for nonmagnetic spacers.

In Chapter 8 we discuss the effect of a synthetic antiferromagnet (SAF) polarizing layer on the net polarization and switching currents of nanopillars, to get an insight on how the switching currents and MR are affected by reduction in the spin polarization.

In Chapter 9 we test a recent prediction by Manschot et al. [58] that the positive switching current of a nanopillar (from P to AP state) could be reduced by up to a factor of 5 by using asymmetric nonmagnetic leads to a nanopillar.

In Chapter 10 we study the effect of lower demagnetizing fields on the switching currents of a nanomagnet by spin transfer torque to see whether a lower demagnetizing field noticeably reduces the switching currents as predicted by Katine et al. [46].

Chapter 2

Theory

In this chapter we briefly review those theoretical models of CPP-MR in magnetic multilayers that are relevant to our data. Earlier theses from our group [59, 60, 57] and reviews [24, 61, 2] cover CPP-MR theory more completely. We also briefly review the theory of spin-transfer and current-induced magnetization switching (CIMS) in section 2.6. The theoretical models of STT are given in more detail in the review by Stiles and Miltat [36].

2.1 Origin of GMR

GMR is a result of the spin-dependent scattering of electrons within bulk F-metals and also at F/N interfaces. Such scattering occurs in F-metals due to the spin imbalance of electrons in their 3d sub-bands. Spin imbalance occurs in F-metals because their energy levels are shifted, resulting in unequal filling of energy bands (Fig. 2.1), which is the source of non-zero net magnetization. Therefore F-metals can be used as a source of spin-polarized currents. Whereas in N-metals the energy levels are not shifted and therefore the filling of the energy levels is the same for both spins, which gives zero net magnetic moment. In F/N structures, it is the spin-polarization of the

F-metals that gives rise to GMR.

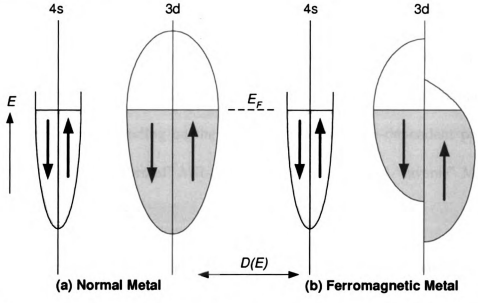

Figure 2.1: A representative diagram of density of states that are available to electrons in (a) a normal metal and (b) a ferromagnetic metal whose spin-up and spin-down states are not equally filled giving a non-zero net magnetization. E is the energy of the electron, E_F is the Fermi level, and $D(E)$ is the density of states.

2.2 Spin-polarized transport

Since the F-metals have a net magnetization, the conduction electrons entering the F-metals will be affected differently depending on the relative orientations of their moments and the local magnetization of the ferromagnet. The resistivity for electrons with moments along (opposite) the local magnetization is denoted by $\rho^{\uparrow}$ ($\rho^{\downarrow}$) using the Valet-Fert notation [12]. Depending on the ferromagnet, $\rho^{\uparrow}$ can be larger than $\rho^{\downarrow}$ or vice-versa. In different papers and reviews [61] spin-up is sometimes used instead of moment-up. In reality the spin of an electron is opposite to its moment because of the negative charge of the electron. More appropriate terms are majority and minority electrons. Majority electrons ($\uparrow$) have their moments along the local magnetization

and minority electrons ($\downarrow$) have their moments opposite to local magnetization.

For F/N/F trilayers and F/N multilayers, the total resistance changes as the magnetizations of F layers switch from parallel (P) to anti-parallel (AP) alignments. The change in resistance is defined as $\Delta R = R(AP) - R(P)$. This change can be positive or negative depending on the bulk and interface spin-dependent properties. If $\Delta R > 0$, it is called "normal" MR and if $\Delta R < 0$, it is called "inverse" MR.

2.2.1 Normal MR

Consider a simple picture of a F/N/F trilayer where the minority electrons scatter more strongly than the majority electrons ($\rho^{\uparrow} < \rho^{\downarrow}$) in the F-metal. To simplify the process of spin dependent scattering we assume only bulk scattering in F layers. If we assume no spin-flipping throughout the sample we can treat the transport with two independently propagating channels of moment up and down electrons (two-current model). Current-mixing due to scattering from magnons and phonons becomes negligible at low temperatures. Therefore the assumption of no current-mixing is valid at low temperatures.

In the **AP** state (Fig. 2.2(a)) the moment-up electrons scatter weakly in the first F layer and strongly in the second, whereas the moment-down electrons scatter strongly in the first F layer but weakly in the second. Therefore the total scattering rates for each channel are the same in the **AP** state. On the other hand, in the **P** state (Fig. 2.2(b))the moment-up electrons scatter weakly in each F layer, whereas moment-down electrons scatter strongly in each F-layer. Therefore in the up-channel we have two weak scattering events and in the down-channel we have two strong scattering events.

A weak scattering represents a low resistance and a strong scattering represents a high resistance. Since we have two different channels of transport, we can treat these channels as two resistors in parallel. The resistance of the trilayer is higher in **AP** state in this case. This type of MR is known as "normal" MR. Although we assumed only bulk scattering, the interface scattering is also important in determining MR. A more detailed analysis will be given in Sections 2.3 and 2.3.1.

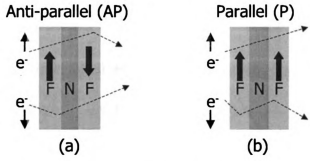

Figure 2.2: Normal MR: A schematic representation of spin-dependent scattering in a F/N/F trilayer with $\rho_F^{\uparrow} < \rho_F^{\downarrow}$. (a) In the AP state the net scattering in both spin channels is the same. (b) In the P state the net scattering in the down-channel is greater than the one in the up-channel. Therefore the resistance in the AP state is higher. Breaks in the dashed lines indicate strong scattering.

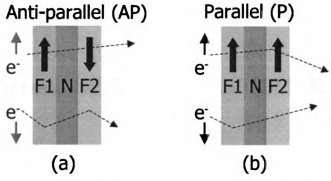

Figure 2.3: Inverse MR: A schematic representation of spin-dependent scattering in a F1/N/F2 trilayer with $\rho_{F1}^{\uparrow} < \rho_{F1}^{\downarrow}$ and $\rho_{F2}^{\uparrow} > \rho_{F2}^{\downarrow}$. (a) In the AP state the net scattering in the down-channel is greater than the one in the up-channel. (b) In the P state the net scattering in both channels is the same. Therefore the resistance in the P state is higher. Breaks in the dashed lines indicate strong scattering.

2.2.2 Inverse MR

Consider a more complex trilayer of F1/N/F2 where F1 and F2 are different F-metals. We assume that $\rho_{F1}^{\uparrow} < \rho_{F1}^{\downarrow}$ and $\rho_{F2}^{\uparrow} > \rho_{F2}^{\downarrow}$. Again we assume only bulk scattering in F-layers and no spin flipping.

In the **AP** state (Fig. 2.3(a)), the moment-up electrons scatter weakly in F1 and as well as in F2 because $\rho_{F2}^{\uparrow} > \rho_{F2}^{\downarrow}$, whereas moment-down electrons scatter strongly in F1 and also strongly in F2 due to the same reason. Therefore we have two weak scattering events in the up-channel and two strong scattering events in the down-channel. On the other hand, in the **P** state (Fig. 2.3(b)) the moment-up electrons scatter weakly in F1 and strongly in F2, whereas moment-down electrons scatter strongly in F1 and weakly in F2. Using the same idea of resistors in parallel we can see that the resistance in the **P** state is higher in this case. This type of MR is known as "inverse" MR. Although we assumed only bulk scattering the interface scattering is also important in determining MR. A more detailed analysis will be given in Sections 2.3 and 2.3.1.

2.3 Two-Current Series Resistor (2CSR) model

The first phenomenological explanation of GMR was given by Baibich et al. [9] using a two-current model. Zhang and Levy [22] developed the first theoretical model for CPP transport in F/N multilayers, assuming diffuse scattering and no spin flipping. In this model the electrons with up and down moments are divided into two parallel channels and the resistance of each channel is merely the series resistor sum of the resistances of bulk and interfaces constituting the multilayer.

Later, Lee et al. [23] and Valet and Fert [12] wrote the first 2CSR equations using:

- Bulk scattering anisotropy parameter β_F
- Interface scattering anisotropy parameter $\gamma_{F/N}$
- Renormalized resistivity of ferromagnet ρ_F^*
- Renormalized interface specific resistance $AR_{F/N}^*$, where A is the area through which the current flows.

All of these parameters in the 2CSR model are independent of the layer thicknesses, which are the only lengths in the 2CSR model. β_F determines the relation between the resistivities for electrons with moments along ($\rho_F^\uparrow$) and opposite ($\rho_F^\downarrow$) to the local magnetization and is defined as

$$\beta_F = \frac{\rho_F^\downarrow - \rho_F^\uparrow}{\rho_F^\downarrow + \rho_F^\uparrow}. \tag{2.1}$$

$\gamma_{F/N}$ determines the relation between the interface specific resistances for electrons with moments along ($AR_{F/N}^\uparrow$) and opposite ($AR_{F/N}^\downarrow$) to the local magnetization and is defined as

$$\gamma_{F/N} = \frac{AR_{F/N}^\downarrow - AR_{F/N}^\uparrow}{AR_{F/N}^\downarrow + AR_{F/N}^\uparrow}. \tag{2.2}$$

The renormalized resistivity for F-metals is defined as

$$\rho_F^* = \frac{\rho_F^\uparrow + \rho_F^\downarrow}{4} = \frac{\rho_F}{1 - \beta_F^2}. \tag{2.3}$$

The renormalized interface specific resistance for a F/N interface is defined as

$$AR_{F/N}^* = \frac{AR_{F/N}^\uparrow + AR_{F/N}^\downarrow}{4} = \frac{AR_{F/N}}{1 - \gamma_{F/N}^2}. \tag{2.4}$$

2.3.1 Analysis of a F1/N/F2 trilayer in AP and P states using 2CSR model

Consider a simple trilayer with two different F-metals separated by a N-metal, F1 and F2 with different thicknesses t_{F1} and t_{F2} as shown in Fig. 2.4 and the CPP current is passing through an area A. The total specific resistance of each channel is given by the series resistor sum of bulk and interfaces.

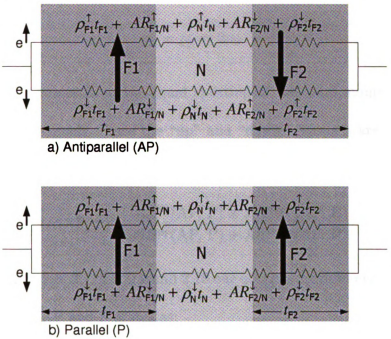

Figure 2.4: A schematic drawing of a F1/N/F2 trilayer showing two channels of electron flow in a) AP alignment b) P alignment. Block arrows represent the direction of local magnetization in each ferromagnetic layer. $\rho_N^{\uparrow(\downarrow)}$ is the resistivity for electrons with moment up (down).

The total specific resistances of the "up" and "down" channels in the AP state are given by

$$AR^{up}(\mathrm{AP}) = \rho_{F1}^{\uparrow} t_{F1} + AR_{F1/N}^{\uparrow} + \rho_N^{\uparrow} t_N + AR_{F2/N}^{\downarrow} + \rho_{F2}^{\downarrow} t_{F2} \tag{2.5}$$

$$AR^{down}(\mathrm{AP}) = \rho_{F1}^{\downarrow} t_{F1} + AR_{F1/N}^{\downarrow} + \rho_N^{\downarrow} t_N + AR_{F2/N}^{\uparrow} + \rho_{F2}^{\uparrow} t_{F2}. \tag{2.6}$$

Similarly, the total specific resistance of the "up" and "down" channels in the P state are given by

$$AR^{up}(\mathrm{P}) = \rho^{\uparrow}_{\mathrm{F1}} t_{\mathrm{F1}} + AR^{\uparrow}_{\mathrm{F1/N}} + \rho^{\uparrow}_{\mathrm{N}} t_{\mathrm{N}} + AR^{\uparrow}_{\mathrm{F2/N}} + \rho^{\uparrow}_{\mathrm{F2}} t_{\mathrm{F2}} \tag{2.7}$$

$$AR^{down}(\mathrm{P}) = \rho^{\downarrow}_{\mathrm{F1}} t_{\mathrm{F1}} + AR^{\downarrow}_{\mathrm{F1/N}} + \rho^{\downarrow}_{\mathrm{N}} t_{\mathrm{N}} + AR^{\downarrow}_{\mathrm{F2/N}} + \rho^{\downarrow}_{\mathrm{F2}} t_{\mathrm{F2}}. \tag{2.8}$$

The electron scattering in an N-metal is spin-independent. Therefore

$$\rho^{\uparrow}_{\mathrm{N}} = \rho^{\downarrow}_{\mathrm{N}} = 2\rho_{\mathrm{N}} \tag{2.9}$$

where the factor 2 comes from the equal splitting of the total number of electrons into up and down channels. Since the "up" and "down" channels are in parallel the equivalent resistances of the trilayer in the AP and P states are given by;

$$AR(\mathrm{AP,\ P}) = \frac{AR^{up}(\mathrm{AP,\ P}) \times AR^{down}(\mathrm{AP,\ P})}{AR^{up}(\mathrm{AP,\ P}) + AR^{down}(\mathrm{AP,\ P})} \tag{2.10}$$

Using Eqns. 2.5, 2.6, 2.7, 2.8, 2.9 and 2.10 one obtains the difference in the specific resistances between AP and P states as:

$$A\Delta R = AR(\mathrm{AP}) - AR(\mathrm{P}) =$$

$$\frac{[AR^{\downarrow}_{\mathrm{F1/N}} - AR^{\uparrow}_{\mathrm{F1/N}} + (\rho^{\downarrow}_{\mathrm{F1}} - \rho^{\uparrow}_{\mathrm{F1}}) t_{\mathrm{F1}}][AR^{\downarrow}_{\mathrm{F2/N}} - AR^{\uparrow}_{\mathrm{F2/N}} + (\rho^{\downarrow}_{\mathrm{F2}} - \rho^{\uparrow}_{\mathrm{F2}}) t_{\mathrm{F2}}]}{(\rho^{\uparrow}_{\mathrm{F1}} + \rho^{\downarrow}_{\mathrm{F1}}) t_{\mathrm{F1}} + (\rho^{\uparrow}_{\mathrm{F2}} + \rho^{\downarrow}_{\mathrm{F2}}) t_{\mathrm{F2}} + 4\rho_{\mathrm{N}} t_{\mathrm{N}} + AR^{\uparrow}_{\mathrm{F1/N}} + AR^{\downarrow}_{\mathrm{F1/N}} + AR^{\uparrow}_{\mathrm{F2/N}} + AR^{\downarrow}_{\mathrm{F2/N}}} \tag{2.11}$$

Substituting renormalized resistivities ρ^* (Eqn. 2.3), interface specific resistances AR^* (Eqn. 2.4), bulk anisotropy parameters β (Eqn. 2.1) and interface anisotropy parameters γ (Eqn. 2.2) for F1 and F2 in Eqn. 2.11, one obtains:

$$A\Delta R = 4\frac{(\beta_{\mathrm{F1}} \rho^*_{\mathrm{F1}} t_{\mathrm{F1}} + \gamma_{\mathrm{F1/N}} AR^*_{\mathrm{F1/N}})(\beta_{\mathrm{F2}} \rho^*_{\mathrm{F2}} t_{\mathrm{F2}} + \gamma_{\mathrm{F2/N}} AR^*_{\mathrm{F2/N}})}{\rho^*_{\mathrm{F1}} t_{\mathrm{F1}} + \rho^*_{\mathrm{F2}} t_{\mathrm{F2}} + \rho_{\mathrm{N}} t_{\mathrm{N}} + AR^*_{\mathrm{F1/N}} + AR^*_{\mathrm{F2/N}}} \tag{2.12}$$

where the denominator of Eqn. 2.12 equals $AR(AP)$.

One can make the sign of $A\Delta R$ and therefore MR negative by making one of the parentheses in the numerator of Eqn. 2.12 negative. If for an F-metal $\beta_F > 0$ and for the interface of this F-metal with an N-metal $\gamma_{F/N} < 0$ or vice-versa, then one can adjust t_F to make the MR negative.

Assume that this trilayer is sandwiched between two superconducting (S) leads. Experiments showed that the S/F interfaces are spin independent [61], thefore $AR^{\uparrow}_{S/F} = AR^{\downarrow}_{S/F} = 2AR_{S/F}$. Then, the S/F1 and F2/S interfaces add only a constant term to each channel. Such constant terms only appear in the denominators of Eqns. 2.11 and 2.12, reducing $A\Delta R$.

If F1=F2=F and $t_{F1} = t_{F2} = t_F$ then Eqn. 2.12 becomes

$$A\Delta R = 4\frac{(\beta_F \rho^*_F t_F + \gamma_{F/N} AR^*_{F/N})^2}{2\rho^*_F t_F + \rho_N t_N + 2AR^*_{F/N} + 2AR_{S/F}} = 4\frac{(\beta_F \rho^*_F t_F + \gamma_{F/N} AR^*_{F/N})^2}{AR(AP)}, \quad (2.13)$$

where for completeness we now include the $2AR_{S/F}$ term.

2.3.2 Validity of 2CSR model

For an F/N multilayer with N bilayers, $A\Delta R$ is

$$A\Delta R = \frac{N^2[\beta_F \rho^*_F t_F + 2\gamma_{F/N} AR^*_{F/N}]^2}{AR(AP)}, \quad (2.14)$$

which can also be rewritten as

$$\sqrt{[A\Delta R][AR(AP)]} = N[\beta_F \rho^*_F t_F + 2\gamma_{F/N} AR^*_{F/N}] \quad (2.15)$$

This equation predicts that for fixed t_F a plot of $\sqrt{[A\Delta R][AR(AP)]}$ vs. N should be a straight line passing through origin. Since the N-metal resistivity doesn't appear in

Eqn. 2.15, data for alloys of a given host metal should fall on the same line, so long as the spin-diffusion length in the alloy is long (i.e. the impurity has a weak spin-orbit interaction in the host). Demonstrations that data for Ag and AgSn [23] (and later for Cu and CuGe [62]) fell on the same line to within experimental uncertainties, although their residual resistivities differed by factors of 20, led to acceptance of the 2CSR model as at least a good first approximation.

2.4 Valet-Fert (VF) model

2.4.1 Overview

Valet and Fert (VF) developed the first theoretical model of CPP-MR that includes spin-flipping in the layers of a F/N multilayer [12]. Using a Boltzmann equation model VF showed that the CPP-MR transport equations reduce to macroscopic transport equations if the spin-diffusion length (the distance an electron diffuses before its spin flips) is much longer than the mean free path $l_{sf} \gg \lambda$ (independent of the ratio of the layer thicknesses to the λ).

To simplify the analysis, VF assumed single parabolic conduction bands for F and N layers with the same effective mass and Fermi velocity throughout the F/N multilayer. The VF analysis is valid at low temperature, where electron-magnon and electron-phonon scattering are weak, leaving spin-orbit interaction, defects or impurities and exchange interaction by paramagnetic moments diluted in N-layers as the active sources of scattering. In the limit $\lambda \ll l_{sf}$, which generally holds for metals, the macroscopic transport equations, independent of the layer thicknesses, reduce to:

$$\frac{e}{\sigma_s}\frac{\partial J_s}{\partial z} = \frac{\overline{\mu}_s - \overline{\mu}_{-s}}{l_{sf}^2}, \tag{2.16}$$

$$J_s = \frac{\sigma_s}{e}\frac{\partial \overline{\mu}_s}{\partial z} \tag{2.17}$$

where e is the electron charge, σ_s is the conductivity for spin s, $\overline{\mu}_{s,(-s)}$ is the chemical potentials for spins $s, (-s)$, J_s is the current density and z is the direction of current flow. Eqn. 2.16 states that, in the steady state, the spin-accumulation (i.e. the difference between the spin-up and spin-down Fermi energies) due to the spin-current divergences is balanced by spin-flipping and Eqn. 2.17 is just the Ohm's law [12].

2.4.2 VF equations for an F/N multilayer

VF derived the total specific resistances of an F/N multilayer with N bilayers in P and AP magnetic configurations as

$$AR^{(P,AP)} = N(r_0 + 2AR_{SI}^{(P,AP)}), \tag{2.18}$$

where $r_0 = (1-\beta^2)\rho_F^* t_F + \rho_N t_N + 2(1-\gamma^2)AR^*_{F/N}$,

$AR_{SI}^P =$

$$\frac{\frac{(\beta-\gamma)^2}{\rho_N l_{sf}^N}\coth\left[\frac{t_N}{2l_{sf}^N}\right] + \frac{\gamma^2}{\rho_F^* l_{sf}^F}\coth\left[\frac{t_F}{2l_{sf}^F}\right] + \frac{\beta^2}{AR^*_{F/N}}}{\frac{1}{\rho_N l_{sf}^N}\coth\left[\frac{t_N}{2l_{sf}^N}\right]\frac{1}{\rho_F^* l_{sf}^F}\coth\left[\frac{t_F}{2l_{sf}^F}\right] + \frac{1}{AR^*_{F/N}}\left[\frac{1}{\rho_N l_{sf}^N}\coth\left[\frac{t_N}{2l_{sf}^N}\right] + \frac{1}{\rho_F^* l_{sf}^F}\coth\left[\frac{t_F}{2l_{sf}^F}\right]\right]} \tag{2.19}$$

and $AR_{SI}^{AP} =$

$$\frac{\frac{(\beta-\gamma)^2}{\rho_N l_{sf}^N}\tanh\left[\frac{t_N}{2l_{sf}^N}\right] + \frac{\gamma^2}{\rho_F^* l_{sf}^F}\coth\left[\frac{t_F}{2l_{sf}^F}\right] + \frac{\beta^2}{AR^*_{F/N}}}{\frac{1}{\rho_N l_{sf}^N}\tanh\left[\frac{t_N}{2l_{sf}^N}\right]\frac{1}{\rho_F^* l_{sf}^F}\coth\left[\frac{t_F}{2l_{sf}^F}\right] + \frac{1}{AR^*_{F/N}}\left[\frac{1}{\rho_N l_{sf}^N}\tanh\left[\frac{t_N}{2l_{sf}^N}\right] + \frac{1}{\rho_F^* l_{sf}^F}\coth\left[\frac{t_F}{2l_{sf}^F}\right]\right]} \tag{2.20}$$

In the limit, where $l_{sf}^N \gg t_N$ and $l_{sf}^F \gg t_F$ these VF equations reduce to the 2CSR equations [12].

2.4.3 Finite spin-diffusion-length effects in a trilayer

The 2CSR equations do not include effects of spin-flipping anywhere. The only lengths appearing in Eqn. 2.12 are the thicknesses of the F- and N-layers. If $t_F \gg l_{sf}^F$ then the 2CSR equation should be corrected by replacing the t_F with l_{sf}^F because the spin dependent scattering within F-layers happens up to the spin diffusion length of F-layer and the remaining thickness of the F-layer ($t_F - l_{sf}^F$) is treated as a constant spin-independent term, which drops out of $A\Delta R$. If $t_F < l_{sf}^F$ then Eqn. 2.12 remains approximately valid. Assuming both $t_{F1} \gg l_{sf}^{F1}$ and $t_{F2} \gg l_{sf}^{F2}$ the 2CSR equation 2.12 becomes (see e.g. ref. [61])

$$A\Delta R = 4\frac{(\beta_{F1}\rho_{F1}^* l_{sf}^{F1} + \gamma_{F1/N} AR_{F1/N}^*)(\beta_{F2}\rho_{F2}^* l_{sf}^{F2} + \gamma_{F2/N} AR_{F2/N}^*)}{\rho_{F1}^* l_{sf}^{F1} + \rho_{F2}^* l_{sf}^{F2} + \rho_N t_N + AR_{F1/N}^* + AR_{F1/N}^*} \tag{2.21}$$

2.5 Real Fermi Surface models of CPP-MR

We noted in Sections 2.3 and 2.4 that the 2CSR and VF models were derived assuming identical spherical Fermi surfaces for both the F- and N-metals. Some CPP-MR models have expanded the 2CSR model to include effects of real Fermi surfaces. Such effects might, or might not, modify the parameters of the 2CSR and VF models. For example, interfacial specific resistances derived using the VF model can agree well with values independently calculated based upon the real Fermi surfaces (see Section 4.7). Of more importance are claims that incorporating real Fermi surfaces can cause the CPP-MR to show 'mean-free-path' effects, i.e., behaviors that vary with the ratios of the mean-free-paths to layer thicknesses of the F- or N-layers [63,

64]. As noted in Section 2.3.2, the initial search for such mean-free-path effects, by comparing square-root plots for Ag and AgSn and for Cu and CuGe, did not show any to within experimental uncertainties. Subsequent claims of observations of mean-free-path effects [65, 66, 67] have been disputed on experimental grounds [68, 69]. At the present time, one cannot rule out mean-free-path effects on the borderline of experimental uncertainties. But we do not know of any data that cannot also be explained by including plausible spin-flipping without any mean-free-path effects ([69, 70], and references therein).

2.6 Spin Transfer Torque & Current-Induced Magnetization Switching

2.6.1 Overview

The spin-transfer phenomenon is treated theoretically assuming either ballistic (in which only the interface scattering is important) or diffusive transport (in which scattering in the bulk and spin accumulation at F/N interfaces are also included). Initial theories assume a macro-spin (single domain) structure for the nanomagnets. Micromagnetic (multi-domain) simulations also describe the underlying physics of the spin transfer excitations.

The original circuit theory of Slonczewski [33] assumed ballistic transport. Slonczewski [33] assumed that upon injection of polarized current into a nanomagnet the transverse component of the electron spin is absorbed by the free layer, providing the source of the torque. By adding this torque term to the Landau-Lifshitz-Gilbert (LLG) equation, Slonczewski solved for the motion of magnetization of a single do-

main nanomagnet, from which he predicted a steady precession of magnetization and a new type of magnetic switching.

On the other hand, assuming diffusive transport, Berger [34, 71] predicted that upon injection of polarized current, coherent magnons are created due to spin accumulation at an F/N interface so that a spin can flip from minority to majority giving rise to the torque and excite a spin wave while conserving energy and angular momentum. Berger showed that the total spin current and spin accumulation are in fixed ratio showing that the Slonczewski model [33] based on spin current and Berger model [34, 71] based on spin accumulation are more or less equivalent [35, 72].

Later, Heide et. al [50, 51, 49] using diffusive transport equations argued that it is the non-equilibrium exchange interaction between s- and d-electrons driven by the current that promotes the torque. In Heide's s-d model the similarities of Fermi surfaces greatly reduces or even eliminates the spin transfer effect. In this case the transverse spin current is not absorbed by the nanomagnet but a transverse spin accumulation develops in the nanomagnet. This transverse spin accumulation precesses relatively slowly around the magnetization giving rise to a torque on the magnetization.

Stiles et al. [73], using a matrix Boltzmann equation formalism, also solved the LLG equation for a nanomagnet. Fert et al. [74] and later Barnas et al. [75] showed that the LLG equations can be solved using diffusive transport for the entire nanopillar structure using Boltzmann equation formalism, which was also used in the theory of CPP-MR [12]. All of these semiclassical models describing the spin transfer phenomenon give qualitatively the same results [36].

The theories described above ignored temperature. Stimulated by their experimental results on dynamical responses of nanopillars, including telegraph noise, Wegrowe et al. [76, 77], Myers et al. [78] and Urazhdin et al. [48, 79], proposed thermally activated pictures of magnetic excitations (Wegrowe and Urazhdin with the dc current I producing incoherent magnons, the effects of which they described via an effective temperature equal to the sum of the ambient temperature and a current dependent temperature). Urazhdin et al. [80] subsequently used a thermally activated model to explain differences in switching behaviors of magnetically uncoupled, ferromagnetically coupled, and antiferromagnetically coupled trilayers. Li and Zhang [81] and Apalkov and Visscher [82, 83] showed that the temperature dependence of the STT could be described as an activated process with an effective temperature that depends upon the exciting current I, but their effective temperatures were proportional to the ambient temperature. Micromagnetic simulations by Lee et al. [84] provided qualitative support for an effective temperature as an approximate way to describe the broad range of excitations generated by the STT current. Krivorotov et al. [85] subsequently argued that the switching rates in their samples depended only upon the true sample temperature, adding support for a simple proportionality of effective and ambient temperatures.

2.6.2 Ballistic transport equations

The initial theoretical model of STT by Slonczweski assumed ballistic transport throughout the magnetic trilayer structure, i.e. the mean free paths of each layer are much longer than their respective thicknesses, therefore bulk scattering is neglected.

Let's consider an F1/N/F2 elliptical nanopillar structure with $\sim$ 100 nm lateral dimensions (see Fig. 2.5). Conventionally the positive CPP current indicates electron flow from the thin F2 (with magnetization $\mathbf{M_2}$) to thick F1 (with magnetization $\mathbf{M_1}$). The equation of motion of $\mathbf{M_2}$ is given by the LLG equation, which is modified to include the STT term.

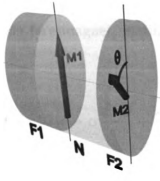

Figure 2.5: A representative cartoon of an elliptical nanopillar, where F1 is a thick (fixed) ferromagnet, N is a nonmagnetic spacer thinner than its spin diffusion length, and F2 is a thin (free) ferromagnet. The angle between the magnetizations **M1** and **M2** is θ.

Slonczewski [33] derived the STT as

$$\frac{d\mathbf{M_2}}{dt} = \left(\frac{Jg(\theta)}{e}\right)[\hat{\mathbf{M}}_\mathbf{2} \times (\hat{\mathbf{M}}_\mathbf{2} \times \hat{\mathbf{M}}_\mathbf{1})] \tag{2.22}$$

where $\hat{\mathbf{M}}_\mathbf{i}$ is a unit vector along $\mathbf{M_i}$, J is the current density, and θ is the angle between $\mathbf{M_1}$ and $\mathbf{M_2}$. The scalar function $g(\theta)$ is given by

$$g(\theta) = \left[-4 + (1+P)^3 \frac{(3+\cos\theta)}{4P^{3/2}}\right]^{-1}. \tag{2.23}$$

Here P is the polarizing factor of the ferromagnet which is defined by

$$P = \frac{n^\uparrow - n^\downarrow}{n^\uparrow + n^\downarrow} \tag{2.24}$$

where $n^{\uparrow(\downarrow)}$ is the Fermi level majority (minority) spin densities in a ferromagnet. Notice that in Eqn.2.22 and 2.23 there is no thickness dependence. This arises from averaging the fluxes with respect to the phase of the exponent e^{ikt} occurring therein, involving phase differences across the thickness (t) of the nonmagnetic spacer layer.

Consider an effective uniaxial anisotropy field H_u, which includes the effect of magnet shape and the phenomenological Gilbert damping coefficient α. The LLG equation for such a single domain ferromagnet, modified to include the torque term (Eqn. 2.22) is [33]

$$\frac{d\mathbf{M_2}}{dt} = \hat{\mathbf{M}}_\mathbf{2} \times \left(\gamma H_u \hat{\boldsymbol{c}} \cdot \mathbf{M_2} \hat{\boldsymbol{c}} - \alpha \frac{d\mathbf{M_2}}{dt} + \frac{Jg(\theta)}{e} (\hat{\mathbf{M}}_\mathbf{1} \times \hat{\mathbf{M}}_\mathbf{2}) \right) \tag{2.25}$$

where γ is the gyromagnetic ratio and a fixed frame is defined by orthogonal unit vectors $\hat{\boldsymbol{a}}$,$\hat{\boldsymbol{b}}$ and $\hat{\boldsymbol{c}}$ of which $\hat{\boldsymbol{c}}$ is the symmetry axis of anisotropy. In the case of $H_u > 0$, $\pm\hat{\boldsymbol{c}}$ are the easy directions for $\mathbf{M_2}$.

The motion of nanomagnet F2 is found by substituting the solution

$$\hat{\mathbf{M}}_\mathbf{2} = (\sin\theta)(\hat{\boldsymbol{a}} \cos wt + \hat{\boldsymbol{b}} \sin wt) + \hat{\boldsymbol{c}} \cos\theta \tag{2.26}$$

into the LLG equation in 2.25 under the assumption of weak damping. Applying the condition $|\dot{\theta}| \ll |w|$ yields the lowest order relations $w = \gamma H_u \cos\theta$ and

$$\dot{\theta} = -(\alpha\gamma H_u \cos\theta + \frac{Jg(\theta)}{M_2 e}) \sin\theta \tag{2.27}$$

where $g(\theta)(> 0)$ is given by Eqn. 2.23 with $\hat{\mathbf{M}}_\mathbf{1} \cdot \hat{\mathbf{M}}_\mathbf{2} = \cos\theta$.

Under some conditions , time dependent solutions to the LLG equation 2.25 describe switching with $\theta(t)$ varying between orientations near easy directions $\theta = 0$ and $\theta = \pi$.

Based on this first theory of Slonczewski, Katine et al. [46] derived the critical currents for switching (assuming I^+ flows from fixed to free layer) from parallel (P) to antiparallel (AP) states as

$$I_c^+ = \frac{\alpha\gamma eS}{g(0)}[H_{eff}(0) + 2\pi M] \tag{2.28}$$

and from AP to P as

$$I_c^- = \frac{\alpha\gamma eS}{g(\pi)}[H_{eff}(\pi) - 2\pi M] \tag{2.29}$$

where M is the magnetization of the switching layer, S is the total spin of the switching layer, and $H_{eff} = H_{an}\cos(\theta) + H_{ext} - H_{exc}$ is the sum of anisotropy, external and exchange (but not demagnetizing) fields. $g(0)$ and $g(\pi)$ depend on the spin-dependent transmission probabilities of the F/N interfaces, the relative orientation (0=parallel, π=antiparallel) of the nanomagnet and any spin-flip scattering that may occur in the system.

2.6.3 Diffusive transport equations

Although the circuit theory of Slonczewski [33] describes much of the experimental data obtained at least qualitatively, the ballistic transport assumed in his theory does not explain all the data. In 2002, Slonczewski [86] extended his model to include diffusive transport in the ferromagnetic layers, with the spacer still treated as ballistic because it is usually thin compared to its mean-free-path. In the diffusive transport calculations an additional phenomenon 'spin-accumulation' enters the transport equations [12]. At an F/N interface, far from the interface to the F side the incoming electrons are polarized, where there are more majority electrons and far from the interface to the N side the outgoing electrons are unpolarized. This implies that within

the F and N spin diffusion lengths of the F/N interface majority electrons must flip their spins to give equal majority and minority channels well into the N-metal. The splitting between the chemical potentials (Fermi energies) of majority and minority channels, is called "spin-accumulation" [87].

Later Xiao et al. [88] derived the torque using matrix Boltzmann equation formalism assuming diffusive transport. The torque exerted on the magnetization $\mathbf{M_2}$ using micromagnetic simulations is expressed as

$$\frac{d\mathbf{M_2}}{dt}|_{st} = -\frac{|g|}{2}\frac{\mu_B}{M_S^2}\frac{1}{d}\frac{J}{e}\mathcal{P}[\mathbf{M_2} \times (\mathbf{M_2} \times \hat{\mathbf{M}}_\mathbf{1})], \tag{2.30}$$

where μ_B is the Bohr magneton, J is the charge current density normal to the interfaces, M_S is the saturation magnetization [36] and d is the thickness of the nanomagnet. One evident difference of this torque term is that it includes the thickness of the switching layer which is inversely proportional to the torque. $\mathbf{M_2}$ is the magnetic moment of the nanomagnet and $\hat{\mathbf{M}}_\mathbf{1}$ is a unit vector in the direction of the magnetic moment of the fixed layer (see Fig. 2.5). By convention g_e is negative for free electrons. Since the orbital moment in transition metals is small, the Lande' g-factor for transition metals is close to -2. $\mathcal{P}$ is a polarization function that contains all the information originating from the structure of the sample and depends on the relative orientations of the magnetizations and is given by.

$$\mathcal{P} = \frac{q_+}{B_0 + B_1 \cos\theta} + \frac{q_-}{B_0 - B_1 \cos\theta}, \tag{2.31}$$

where $\cos\theta = \hat{\mathbf{M}}_\mathbf{1} \cdot \hat{\mathbf{M}}_\mathbf{2}$. The parameters B_0, B_1, q_+ and q_- depend on the geometry of the sample and the physical properties of the bulk and interfaces including the spin accumulations in the N spacer layer at both F1/N and N/F2 interfaces. In particular

they depend on the effective spin-dependent resistances from the spacer layer in either direction over one spin diffusion length [88, 36]. $\mathcal{P}$ is usually positive but as we will show later in Chapter 6, it can be made negative using judicious choice of materials [89]. Inserting this STT into the LLG equation one obtains the equation of motion of $\mathbf{M_2}$ as

$$\begin{aligned}\frac{d\mathbf{M_2(r)}}{dt} &= -\gamma[\mathbf{M_2(r)} \times \mathbf{H_{eff}(r)}] - \frac{|g|}{2}\frac{\mu_B}{M_S^2}\frac{1}{d}\frac{J}{e}\mathcal{P}(\mathbf{r})[\mathbf{M_2(r)} \times (\mathbf{M_2(r)} \times \hat{\mathbf{M}}_1)] \\ &\quad +\alpha\left(\mathbf{M_2(r)} \times \frac{d\mathbf{M_2(r)}}{dt}\right). \end{aligned} \tag{2.32}$$

Fig. 2.6 shows a comparison of the torques calculated using Slonczewski's diffusive model [86] with Boltzmann equation model and Slonczewski's ballistic model [33]. As it is clear from Fig. 2.6 the Boltzmann equation model of Xiao et al. [88] agree very well with Slonczewski's diffusive circuit theory [86] but not so well with the ballistic Slonczewski model [33].

Fert et al. [74] and Barnas et al. [75] derived the STT at small angle assuming diffusive transport for the entire nanopillar structure including spin-accumulation and spin-current as

$$\begin{aligned}\tau^{P(AP)} &= -\hbar\left[\left(\frac{v_F m_{\mathrm{N}}^{P(AP)}}{8} + \frac{j_{m,\mathrm{N}}^{P(AP)}}{2}\right)(1 - e^{-t_{\mathrm{N}}/\lambda_{\mathrm{N}}})\right. \\ &\quad \left. + \left(\frac{v_F m_{\mathrm{F1}}^{P(AP)}}{4} + j_{m,\mathrm{F1}}^{P(AP)}\right)e^{-t_{\mathrm{N}}/\lambda_{\mathrm{N}}}\right]\hat{\mathbf{M}}_2 \times (\hat{\mathbf{M}}_2 \times \hat{\mathbf{M}}_1) \end{aligned} \tag{2.33}$$

where $\hat{\mathbf{M}}_1$ and $\hat{\mathbf{M}}_2$ are unit vectors along the magnetizations of fixed and free layers respectively, t_{N} is the thickness of N-spacer, λ_{N} is the mean-free-path in the N-metal, and v_F is the Fermi velocity. $m_{\mathrm{N}}^{P(AP)}$ and $j_{m,\mathrm{N}}^{P(AP)}$ are the spin-accumulation density and spin current density in the N spacer layer at the N/F2 interface, whereas $m_{\mathrm{F1}}^{P(AP)}$ and

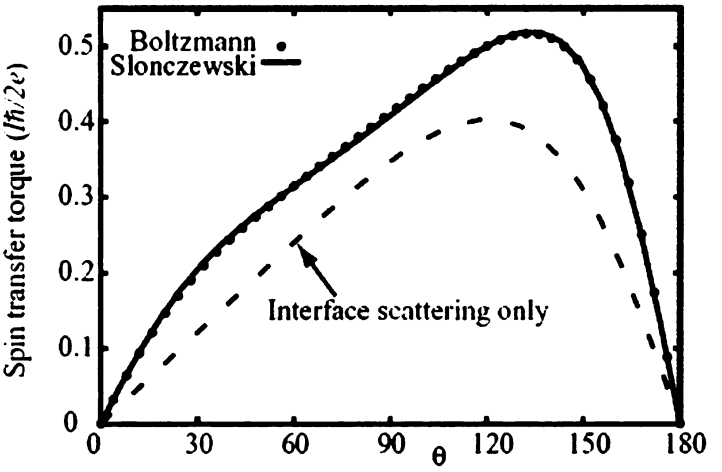

Figure 2.6: Spin-transfer torque acting on the magnetization of a 1 nm thick nanomagnet as a function of θ. Solid circles are Boltzimann equation results. The solid curve is the torque derived from Slonczewskis later theory [86] including bulk scattering. The dashed curve is the torque with all bulk scattering removed. The figure is taken from ref. [88].

$j_{F1}^{P(AP)}$ are the spin-accumulation density and spin-current density in F1 at the N/F1 interface. The first parenthesis in Eqn. 2.33 dominates in the limit $t_N \gg \lambda_N$, and the second parenthesis in Eqn. 2.33 dominates in the limit $t_N \ll \lambda_N$. One advantage of this Fert equation for torque is that it directly includes the spin-accumulation and spin-current terms, which would provide a more straightforward analysis using the parameters obtained from CPP-MR experiments.

2.6.4 Summary

In the simple ballistic picture described in the introduction, F1 polarized the current and the component of that polarized spin-current perpendicular to $\mathbf{M_2}$ of F2 exerted a torque on $\mathbf{M_2}$. In the more complex picture arising from analysis of diffusive scattering, both spin-current and spin-accumulation play important roles in STT, and both must be determined self-consistently for the whole sample– i.e., taking into

account the properties of all components of the sample-layers F1, N, F2, the leads to both F1 and F2, and the interfaces between these layers.

Chapter 3

Sample Fabrication and Measurement

3.1 Overview

In this chapter, we describe the experimental procedures used to make and measure the samples for both CPP-MR and CIMS studies. For the CPP-MR studies we make Nb-sandwiched magnetic multilayers. To get a uniform current density through the multilayer, we sandwich the multilayer between two crossed Nb leads, which superconduct at our measuring temperature of 4.2K [59]. For CIMS studies we fabricate magnetically uncoupled elliptical nanopillars of $\sim 130 \times 70$ nm lateral dimensions. Since both studies involve sputtering, our sputtering procedures are described under CPP-MR sample fabrication (in section 3.2.2) and then referenced for nanopillar fabrication (section 3.4), in which sputtering is only one step in a complex fabrication process.

3.2 Making and measuring Nb-sandwiched magnetic multilayers for CPP-MR studies

3.2.1 Preparation

We begin with 3″ diameter (100) Si wafers, which have insulating SiO_2 layers on top. For CPP-MR studies we dice the wafer into 0.5″ × 0.5″ square substrates. We clean these Si substrates in a dilute alconox solution and rinse them thoroughly with deionized (DI) water, then in acetone and ethanol respectively using ultrasonic agitation in each step. Then, we blow-dry the substrates with pure nitrogen gas to get rid of any residues from ethanol.

We clean the substrate holders, masks and the sputtering gun parts by washing them in a nitric acid solution to remove any previously deposited metals. These parts are then cleaned with acetone and ethanol using ultrasonic agitation in each step, and then we dry them using a heat gun.

Clean substrates are loaded into sample holders and placed on a rotating sample positioning and movement assembly (SPAMA) plate [59]. The SPAMA plate has two computer-controlled film thickness monitors (FTM) placed opposite to each other and 8 circular openings for sample holders and masks. The SPAMA plate can hold 8 substrates for Nb-sandwiched CPP samples or 16 substrates for single film samples [59, 31].

3.2.2 Sputtering

We make the samples by sputtering metal or alloy targets. Four triode and two dc-magnetron guns allow us to make complex multilayers. The vacuum chamber is

pumped down by first a mechanical and then a cryo pump. To lower the pressure and partly eliminate the water vapor inside the chamber, the chamber is baked for 8 hours right after closing the system. It takes 2 nights to pump down to $3-4\times10^{-8}$ Torr base pressure for the first run. If we want to make more samples using the same targets, we just load new substrates into the sample holders and close the chamber. In this case it takes 1 night to pump down to $3-4\times10^{-8}$ Torr.

Before starting-up the sputtering guns, we fill a cold trap in the sputtering chamber with liquid nitrogen. The flow rate of the liquid nitrogen is adjusted to maintain a constant cold trap temperature of 82K (we cannot reach 77K because of the pressure we apply for the liquid nitrogen to flow). This allows us to freeze most of the water vapor inside the chamber and get $2-3\times10^{-8}$ Torr base pressure. An argon gas purifier is used to get ultra pure argon gas for sputtering. We sputter the metals or alloys in 2.5 mTorr argon pressure.

While all masks and the shutter are closed, we pre-sputter all targets inside the chamber (except Au and Pt because they don't oxidize) for 10-20 minutes to remove oxide surface layers and to stabilize their surfaces. Each target has a chimney to collimate the sputtered atoms and prevent contamination from nearby targets.

The deposition rates of sputtering targets are individually measured just before making each sample. Table 3.1 shows typical sputtering rates for some materials. The actual sputtering rates will be given with the experiments. A computer controls the shutter and the SPAMA plate. The computer initially moves the sample over the chosen target by rotating the SPAMA plate, opens the shutter, and leaves the sample over the target for a time calculated by the computer using the deposition rate from

a FTM reading. After the deposition is completed, the shutter is closed or kept open depending on the next target's position in the chamber. Then the sample is moved to the next target in the multilayer sequence and so on.

Target	Nb	Cu	Py	Au	Co
Deposition rate (Å/s)	4.5-5	9-11	4.5-5	4-5	2-4

Table 3.1: Typical sputtering rates for Nb, Cu, Py, Au and Co.

During the sputtering of multilayers, the substrate temperature is kept between -30 and +30°C. Making one CPP sample usually takes 25-30 minutes and this causes the substrate temperature to increase by only a few degrees centigrade. To achieve this approximately constant substrate temperature during sputtering, we cool the SPAMA plate constantly by a capillary tube that is in contact with both the liquid nitrogen cold trap and the SPAMA plate. We run pressurized nitrogen gas at 1000 psi through the capillary tube to enable the necessary heat exchange between the cold trap and the SPAMA plate [59].

Each substrate has its own rotary CPP mask, attached to the sample holder [59]. A CPP mask has 4 positions as shown in Fig. 3.1(a), which is initially in the closed position (1). We turn the mask manually (using a vacuum-sealed wobble stick) to: first, position (2) and sputter 150-200 nm Nb as a bottom lead, then we turn the mask to position(3) and sputter the multilayer and then we turn it to position (4) and sputter 150-200 nm Nb as the top lead. Finally, the mask is turned to position (1) to protect it from contamination during the sputtering for other substrates in the chamber. A finished CPP sample is shown in Fig. 3.1(b).

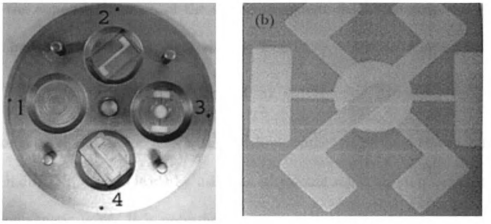

(a) (b)

Figure 3.1: (a) A rotary CPP mask: position (1) is closed to protect the sample before and after sputtering, position (2) is for the bottom Nb contact, position (3) is for the multilayer and position (4) is for the top Nb contact. (b) A finished CPP sample. The width of each Nb contact is $\sim$ 1.1 mm.

3.3 Measuring the Resistances of CPP samples

The CPP samples for this thesis have two different structures as described earlier:

1. Exchange-Biased Spin Valves (EBSV).

2. Hybrid spin valves.

3.3.1 Pinning

In an exchange-biased spin valve (EBSV) one of the ferromagnetic (F) layers is sputtered next to an antiferromagnetic (AF) layer (FeMn in our samples). To pin the magnetization of this F layer, we heat the sample to above the Néel temperature of the antiferromagnet in a vacuum chamber and cool the sample back to room temperature in an external magnetic field. This process pins the magnetization of the F layer that is next to the AF layer. Pinning a ferromagnetic metal shifts its hysteresis curve

toward the opposite direction of the applied magnetic field, changing its switching field dramatically.

3.3.2 Resistance measurement at 4.2K

To make good electrical contacts with very low contact resistances to the Nb leads, we put indium on the Nb leads by using an ultrasonic soldering iron before pinning the ferromagnetic layer. It is necessary to use an ultrasonic soldering iron to make a good electrical contact to Nb, because Nb oxidizes very quickly. The sample is mounted on a measurement stick (quick dipper) and the current and voltage leads are pressed on indium at room temperature. We avoid using any hot soldering to connect the leads because it can unpin the pinned ferromagnetic layer in an EBSV.

All CPP samples are measured at 4.2K in liquid helium, where the Nb leads become superconducting. Since the top and bottom Nb contacts superconduct at 4.2K, our standard CPP measuring current of 100 mA passes uniformly through a big area A$\sim$ 1.2 mm^2 like a parallel plate capacitor (see Figure 3.2). The area A, is the product of the widths of two Nb strips. The widths of Nb strips are measured using a Dektak surface profilometer [59, 60]. The uncertainties in the areas of the samples are $\sim$ 5%.

The resistances of these CPP samples are in the order of $10^{-8}\Omega$ because the samples are very thin ($t \sim$ 100 nm) and the areas of the samples are large (A$\sim$ 1.2 mm^2). To measure these very small resistances, we use a Superconducting Quantum Interference Device (SQUID) based circuit. The details of this 4-probe measurement are described elsewhere [59, 31]. The sample is placed inside a 1″ diameter superconduct-

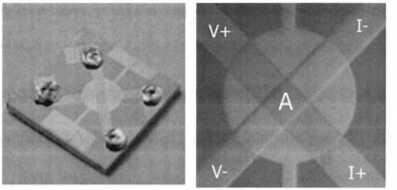

Figure 3.2: (a) A CPP sample with lumps of indium on Nb contacts. (b) Center of a CPP sample; The current passes only through the area of intersection of two Nb leads at 4.2K.

ing solenoid magnet, which is capable of producing fields up to 1.5 T. The sample is positioned in the center of the solenoid in such a way that the field produced is parallel to the sample plane. Then, the stick is slowly lowered in a liquid helium storage dewar, until the sample and the SQUID are under the liquid helium surface. It takes $\sim$ 20 minutes to cool down to 4.2K and $\sim$ 20 minutes to warm up to room temperature. Due to this very short time for cooling of the sample compared to other methods [90], the measurement stick is called "quick-dipper". At 4.2K we measure the resistances of CPP samples at different external magnetic fields produced by the superconducting solenoid. For Py-based EBSVs we sweep the field in steps between -300 Oe and +400 Oe, and for Py-Co hybrid spin valves we sweep the field in steps between -1 kOe to +1 kOe. Resistance vs. magnetic field plot gives us the change in resistances between parallel and anti-parallel states of the sample.

3.4 Making and measuring nanopillars for CIMS studies

Making nanopillars is a multi-step process, which requires a lot of care and patience. Starting from scratch it takes about a week to fabricate nanopillars, assuming no problems. We make magnetically uncoupled F1/N/F2 elliptical nanopillars of $\sim$ 130 $\times$ 70 nm lateral dimensions, where F1 is a thick and wide (fixed under CIMS) polarizing ferromagnet, N is a normal metal thinner than its spin diffusion length but thick enough ($\sim$ 10 nm) to minimize exchange coupling and F2 is a thin (free under CIMS) nanomagnet. In this system, since F1 is several microns wide and F2 is a nanomagnet, the dipolar coupling between F1 and F2 is minimal. We make 5 nanopillars (with the same structure) on a single 0.5″ $\times$ 0.5″ Si substrate. In a single run we process 4-8 substrates and therefore 20-40 nanopillars. Following is an outline of the fabrication of nanopillars.

1. Preparation of substrates using photolithography and evaporation.

2. Electron beam lithography (EBL) for the multilayer and sputtering.

3. EBL for nanopillars and evaporation of Al.

4. Ion-milling and insulation.

5. Low-angle ion-milling.

6. Top contacts.

Photolithography and EBL steps are done in a class-100 clean room.

3.4.1 Preparation of substrates using photolithography and evaporation

We start with single crystal 3″ diameter (100) Si wafers. Because the Si wafers are packed in a clean room environment, and we open the wafer box in a clean room, they usually don't need further cleaning. However, if the wafer is visibly dirty, it is cleaned in acetone, isopropyl alcohol (IPA) using ultrasonic agitation in each step. Then the wafer is immediately blow-dried.

Photolithography

Before sputtering the multilayer, Au current and voltage leads must be evaporated onto the wafer. Photolithography is used to open the areas on the wafer for the leads. Following is a recipe for photolithography.

1. Spin S1805 (propylene glycol monomethyl ether acetate) photoresist (PR) on a Si wafer at 3500 rpm for 40 seconds to get a uniform PR thickness of $\sim$ 500 nm.

2. Bake the wafer at 90°C for 1 hour to evaporate the solvent and harden the PR layer.

3. Place the wafer on a vacuum chuck in a mask aligner and align with the photomask, which has the shape of the leads transparent to ultraviolet (UV) light and the rest coated with Cr to block UV light (see Fig. 3.3). Bring the wafer and the mask into complete contact leaving almost no air between them and expose the wafer to the UV light for 2.5 seconds. UV light breaks chemical bonds in the PR polymer by allowing the exposed PR to be dissolved in photo developer (KOH)

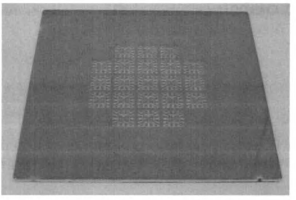

Figure 3.3: A picture of the photomask. The open areas have the shape of the leads and the rest of the mask is coated with Cr to block UV light.

4. Harden the surface of the PR by dipping the exposed wafer in chlorobenzene for 20 seconds . Immediately after taking out the wafer from chlorobenzene, rinse the wafer under running DI water for 3-5 minutes until the wafer is completely free of chlorobenzene residues. Then blow-dry the wafer with pure nitrogen gas. Hardening the surface of PR is crucial to get a good undercut after developing. This process makes the PR layer behave like a bilayer i.e. the surface of the unexposed PR reacts with KOH slower than the rest of the PR giving a good undercut (see Figure 3.4). A good undercut ensures a trouble-free lift-off. If the undercut is not very good, the lift-off is irregular because acetone (the chemical used for lift-off) cannot easily penetrate into the PR layer.

5. Finally, we develop the wafer in photo-developer (452, KOH) for $\sim$ 45 seconds, until the entire exposed area of PR is dissolved.

Evaporation of leads

1. Load the wafer into a thermal evaporator within the clean room and close the chamber to pump down to $1 - 2 \times 10^{-7}$ Torr. Fill the cold trap with liquid

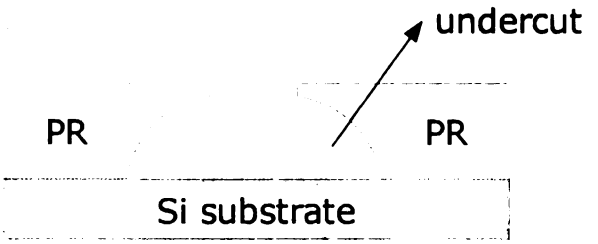

Figure 3.4: A cartoon of a good undercut after developing. The top part of the PR reacts very slowly with KOH.

nitrogen to get to $1 - 2 \times 10^{-7}$ Torr faster.

2. First, evaporate 3 nm Ti to get a strong adhesion to the Si wafer, then evaporate 80 nm Cu to decrease the resistance of the leads and finally, evaporate 100 nm Au to protect it from oxidation. A 100nm thick Au top layer is crucial to see the leads better in SEM during electron beam lithography.

3. Take the wafer out of the evaporator and place it in acetone facing the evaporated side down to lift-off. PR dissolves in acetone and since the PR is everywhere on the wafer except the areas for leads, all excess metal layers will be removed in acetone leaving the metals in the areas for the leads created by photolithography.

4. Rinse the wafer with IPA and DI water respectively immediately after taking it out of acetone and then blow-dry it with pure nitrogen gas. Fig. 3.5 shows a 3″ Si-wafer after lift-off with the leads evaporated.

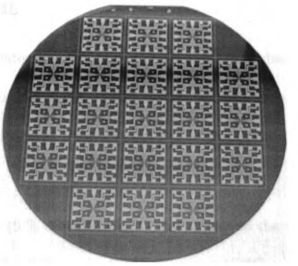

Figure 3.5: A picture of a 3″ wafer after lift-off, which has 21 0.5″ × 0.5″ square substrates.

3.4.2 EBL for the multilayer and sputtering

E-beam Lithography (EBL)

EBL works much the same way as photolithography except the resists are different and there is no mask involved. In EBL, a computer controlled electron beam in an SEM scans the desired shape and the e-beam resist in the scanned area becomes soluble in e-beam developer, which is 1:3 mixture of MIBK (4-methyl-2-pentanone) and IPA). Using EBL one can make features smaller than 50 nm, depending on the type and thickness of the e-beam resist [91]. For EBL we use a modified SEM (JEOL 840A with tungsten hairpin electron source)with a beam blanker. The SEM is connected to a computer through an interface which allows the computer to control the e-beam using NPGS (Nano Pattern Generation System) software. NPGS software scans the e-beam over the shape and size of our desired feature, which we draw using DesignCAD software.

Preparation for EBL

To prepare the substrate for EBL we have to coat it with e-beam resists. To achieve a uniform thickness of the resist we spin the wafer during coating. To get a good undercut we spin a bilayer of e-beam resists. Following are the steps for preparation for EBL:

1. Spin 9 % MMA (9 % ethyl lactate) e-beam resist on the wafer at 4000 rpm for 40 seconds and bake the wafer for 5 minutes at 170°C.

2. Spin 2 % PMMA (2 % chlorobenzene) e-beam resist on top of MMA layer at 4000 rpm for 40 seconds and bake the wafer for 30 minutes at 170°C.

We bake the wafers to evaporate the solvent in the e-beam resists. Then we dice the wafer along the boundaries of the individual $0.5'' \times 0.5''$ substrates. We get 21 substrates out of a $3''$ Si wafer. Fig. 3.6 shows a single substrate and its center. The crosses are the alignment marks used to align the sample in a Scanning Electron Microscope (SEM) for EBL.

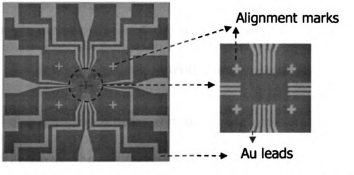

Figure 3.6: A single substrate (left) and its center (right) with the gold leads evaporated.

EBL for the multilayer

We need to open a window for the multilayer at the center of our substrate, which is totally covered with an e-beam resist bilayer. The following is a recipe of EBL for the multilayer.

1. Load the substrate into the SEM and write the pattern in Figure 3.7. The beam current is 25 pA. The area dose is $130\mu C/cm^2$ for the inner pattern and $70\mu C/cm^2$ for the outer one. Therefore the outer shape is exposed to less e-beam than the inner shape. This gives us a bigger undercut which is needed for sputtering, because sputtered atoms go in every direction unlike the more collimated evaporated ones.

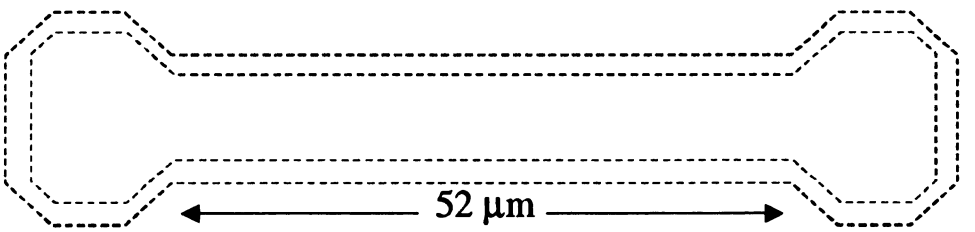

Figure 3.7: The DesignCAD drawing for the shape of the multilayer.

2. Take the sample out of SEM and dip it in the e-beam developer for 30 seconds to develop. The developing time depends on the beam current and dose.

3. Take the substrate of the e-beam developer and immediately dip it in IPA for 10 seconds to remove the residues from the developer. Then take it out of the IPA and blow-dry immediately.

4. Check the development using an optical microscope.

If the feature does not develop perfectly within the first 30 seconds develop 5 seconds more and so on until it is fully developed. Fig. 3.8 shows a developed area for the multilayer.

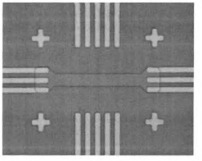

Figure 3.8: An opening for the multilayer created by EBL. Scale as in Fig. 3.7.

Sputtering

We load these substrates into the sample holders behind stainless steel masks, which have small circular holes at their centers to prevent excess heating of the e-beam resists. The details of our sputtering procedure are the same as described in section 3.2.2 of this chapter, except we use different sample holders and rotary masks that have only open and closed positions.

For the present current-induced magnetization switching (CIMS) studies, we usually make a trilayer structure of F1/N/F2. The polarizing F1 layer is thick enough so that current doesn't flip its magnetization. The N layer is thick enough to eliminate exchange coupling but thinner than its spin diffusion length. The F2 layer is thin enough so that a high enough dc current can flip its magnetization.

To get a nearly uniform current through a nanopillar, the sheet resistance, ρ/t, of the contacts should be small compared to the resistance of the sample. For this reason we sputter 80nm Cu as a bottom contact which has 0.25Ω sheet resistance at room

temperature whereas the resistance of a typical nanopillar is $\sim 1\Omega$. Then, we sputter a F1/N/F2 trilayer, and then sputter 15-20nm Au to protect it from oxidation. Since we will do several more processes on this multilayer, it is important to keep it from oxidation. After the sputtering, we put the samples in acetone to lift-off. Fig. 3.9 shows a multilayer after this step.

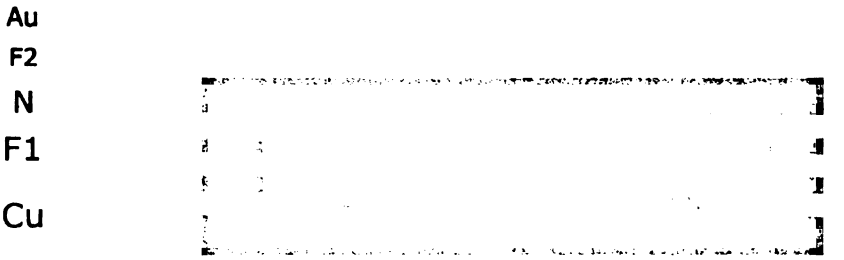

Figure 3.9: (a) A cross-sectional cartoon of a multilayer. (b) An SEM image of a multilayer after lift-off.

3.4.3 EBL for nanopillars and evaporation of Al

EBL for nanopillars

Now we have our multilayer sputtered, and we need to create 5 nanopillars on this "big" sample ($\sim 8 \times 50\mu$m). The following is a recipe for opening nano-sized holes in the e-beam resist.

1. Spin 9% MMA at 6000 rpm for 30 seconds and bake it for 5 minutes at 170°C.

2. Spin 2% PMMA at 6000 rpm for 30 seconds and bake it for 30 minutes at 170°C.

3. Load the sample into SEM and write 5 ellipses ($\sim 130 \times 70$ nm lateral dimensions) 6μm apart from each other on the midline of the multilayer (see Fig. 3.10 (a)). The beam current is 9 pA and the area dose for the features is 475μC/cm^2.

4. Develop the ellipses in e-beam developer as described in section 3.4.2.

5. Check the development using an optical microscope. This step in the fabrication is very crucial to get a well defined elliptical nanopillar. Since their dimensions are below optical resolution, it is impossible to see the details of these ellipses using an optical microscope. However, when these features develop it is possible to see some light coming out of them. There is no way of seeing whether these ellipses are over or under developed, therefore there is always an uncertainty in the dimensions of these holes. Fig. 3.10 (a) shows an optical image of the multilayer with 5 elliptical openings after this step.

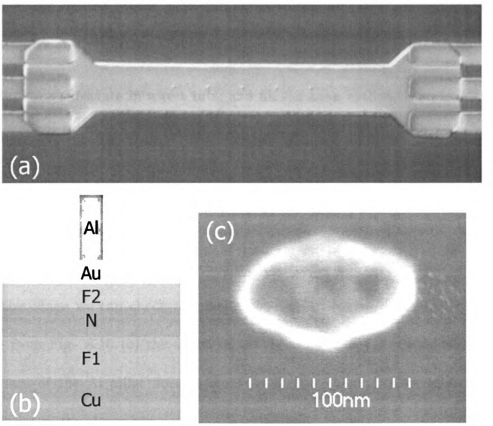

Figure 3.10: (a) An optical image of 5 elliptical openings fabricated using EBL, the rest of the substrate is covered with e-beam resist. Since the dimensions of ellipses are below optical resolution we only see some light coming out of these holes. Scale as in Fig. 3.9. (b) A cartoon of the cross-section of multilayer + Al mask (c) An SEM image of an elliptical Al mask (top view).

Evaporation of Al

Now we have to evaporate Al into these elliptical openings to serve as a mask for ion-milling.

1. Load the substrates into a thermal evaporator in a class-10000 clean room and close the chamber to pump down to $1 - 2 \times 10^{-7}$ Torr. Fill the cold trap with liquid nitrogen to get to $1 - 2 \times 10^{-7}$ Torr faster.

2. Evaporate 60 nm of Al. When Al is evaporated, it goes through the elliptical openings created by the EBL and sticks to the Au layer, making an elliptical Al mask on the surface of the multilayer.

3. Put each substrate in a test tube and fill the tube with acetone to lift off. To speed up the process of lift-off, heat the test tube on a hot plate at 80°C. It takes about half an hour to lift-off. Fig. 3.10 (b) shows a cartoon of the cross-section of the multilayer + Al mask after lift-off and Fig. 3.10 (c) shows a top view SEM image of an Al elliptical mask on top of the sputtered Au layer.

At this stage we can check the shape of Al pillar masks using an SEM. As we can see from Fig. 3.10 (c) the shape of the Al mask is not perfectly elliptical and the surface of the Al pillar doesn't seem to be flat. The possible reasons for the inaccuracies in the shape are:

- The resolution of EBL is comparable to the size of our nanopillar.

- It is impossible to check the development using an optical microscope.

All of our Al masks appear like the one in Fig. 3.10(c), i.e. we don't see a flat surface. We also made Au and Ag pillars of the same dimensions and checked them with an SEM to see whether they give a similar surface roughness. It seems from Fig. 3.11 that if we evaporate Au or Ag in to the $\sim 130 \times 70$ nm elliptical openings they tend to have a flat surface. But Au and Ag are not good candidates to be used as a mask for ion-milling because their ion-milling rates are much larger than the ion-milling rate of Al (see Table 3.2). Although the surfaces of our Al masks are very rough, this shouldn't affect the ion-milling of the multilayer because the Al mask is thick enough so even thinner parts don't mill completely through.

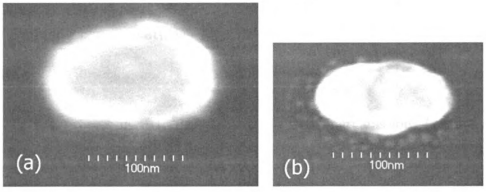

Figure 3.11: (a) An SEM image of a Au pillar. (b) An SEM image of a Ag pillar.

3.4.4 Ion-milling and Insulation

EBL for Ion-milling

To ion-mill through the multilayer, we need to open a window over the multilayer using EBL, because we don't want to ion-mill the leads. The following is a recipe for opening a window using EBL.

1. Spin 9% MMA at 4000 rpm for 30 seconds and bake for 5 minutes at 170°C.

2. Spin 2% PMMA at 4000 rpm for 30 seconds and bake for 30 minutes at 170°C.

3. Load the sample in the SEM and write the pattern in Fig. 3.12. The beam current is 25 pA. The area dose is $130\mu C/cm^2$ for the inner pattern and $70\mu C/cm^2$ for the outer one.

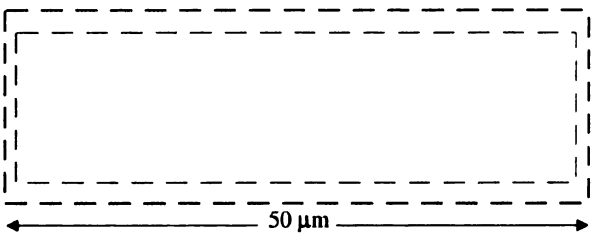

Figure 3.12: The DesignCAD drawing of a window for ion-milling. Outer rectangle is exposed to less e-beam than the inner one to get a good undercut.

4. Develop the sample as described in section 3.4.2. Fig.3.14 (a) shows an image of a window over a multilayer after development.

Ion-milling

Ion-milling is a process used to dry-etch metals with inert gas ions (we use argon). The process is the opposite of sputtering, in which the target atoms are knocked off by accelerated argon ions and deposited on a substrate. We ion-mill our samples using a different vacuum chamber, which has a broad-beam ion source, a dc-magnetron sputtering gun, an evaporation boat to evaporate silicon monoxide (SiO), and a film thickness monitor (FTM). This vacuum system also has a load-lock, which allows us to insert and take out samples without venting the chamber.

Since we ion-mill through a multilayer of different materials, we need to estimate the ion-milling rates of different materials from the ion-milling rate of Au. To measure the ion-milling rate for Au, we:

1. Sputter $\sim$ 400Å Au on the FTM crystal.

2. Turn-on the ion-mill and let it run for 5 minutes to stabilize.

3. Move the FTM over the ion-mill and read the Au removal rate from the FTM controller.

Once the ion-milling rate for Au is measured, we estimate the rates for other metals using Table 3.2 and calculate the total time needed to ion-mill. Then the sample is moved over the ion-mill and kept there for the duration calculated.

Metal	Al	Fe	Co	Ni	Py	Ru	Ag	Cu	Au
Rate (Å/min.)	730	530	550	660	634	610	2200	1100	1700

Table 3.2: Argon ion etch rates for the metals we etch at an ion current density of 1 mA/cm^2 and an ion energy of 500 eV. Values are taken from Ref. [92] except for Py, which is calculated from the Ar ion etch rates of Ni and Fe.

Ion-milling around the Al masks

Fabrication of a F/N/F nanopillar requires ion-milling around the Al masks which are on top of the multilayer. To ion-mill we put the substrate in a special sample holder (see Fig. 3.13) which has a stainless steel mask with a tiny hole at the center. Therefore we expose only a small area at the center of the substrate to the argon ions, which prevents the accelerated ions from burning the e-beam resist.

When we ion-mill around the Al masks, we etch the parts of the multilayer which are not covered with Al. The areas below the Al masks stay intact because the Al masks get ion-milled instead of the multilayer, leaving a F/N/F nanopillar right under the masks. Therefore these nanopillars have approximately the elliptical shape and the size ($\sim$ 130 $\times$ 70 nm) of the Al masks. To eliminate the dipolar coupling between two ferromagnets, we try to ion-mill approximately half-way through the

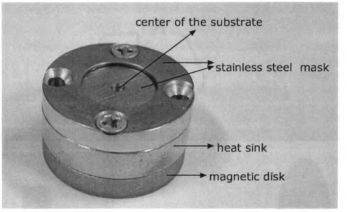

Figure 3.13: A special sample holder for ion-milling. It has a heat sink to remove heat from the substrate and a magnetic disk to hold it using a magnetic arm.

nonmagnetic metallic spacer layer (see Fig. 3.14 (b)) such that the top ferromagnet is an elliptical nanomagnet and the bottom F-layer is left untouched as a big rectangular ($\sim 8 \times 50 \mu$m) ferromagnet. Since the magnetic poles of the ferromagnets are far apart, there is no dipolar coupling.

Insulation

Right after ion milling, without breaking vacuum, we evaporate SiO to insulate the nanopillar as well as the top and bottom contacts to the nanopillar. To get a uniform thickness of SiO we hold the sample holder using a magnetic arm and spin it at 60 rpm while evaporating SiO. We adjust the total thickness of evaporated SiO such that $\sim$ 10 nm Au is left outside of the insulating layer for the top contact. However, since we evaporate SiO all over the opening for the ion-milling (see Fig. 3.14 (a)), we actually insulate the nanopillar completely as seen in the cartoon of Fig. 3.14 (c).

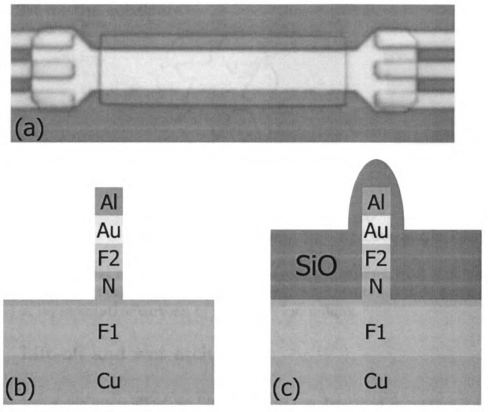

Figure 3.14: (a) An opening over the multilayer for ion-milling, created by EBL. (b) A cartoon of the cross-section of a magnetically uncoupled nanopillar. (c) A cartoon of the cross-section of a magnetically uncoupled nanopillar insulated by SiO evaporation. Scale as in Fig. 3.9.

3.4.5 Low angle Ion-milling

Since the whole pillar region is insulated with SiO we must ion-mill away the excess SiO that is insulating the top contact region of the nanopillar. To do this we use a special sample holder (see Fig. 3.15 (a, b)), which has a cylindrical hole at the center and a nearly vertical (3 degrees with the vertical) slit for the sample. The ion milling time is estimated based on the thickness of the SiO layer and the ion-milling rate. Fig. 3.15 (c) shows a cartoon of the low angle ion-milling from one side. Later, the substrate is flipped and ion-milled from the other side as well.

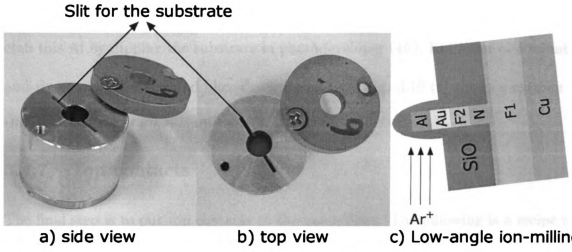

Figure 3.15: A special sample holder for low-angle ion-milling with a circular hole in the middle and a nearly vertical (3°) slit for the substrate.(a) Side view. (b)Top view. (c) A representative cartoon of low-angle ion-milling.

3.4.6 Lift-off and wet etch

After the low-angle ion-milling, we lift-off the SiO as described in section 3.4.3. Fig. 3.16 (a) shows a picture of a multilayer and SiO layer after lift off.

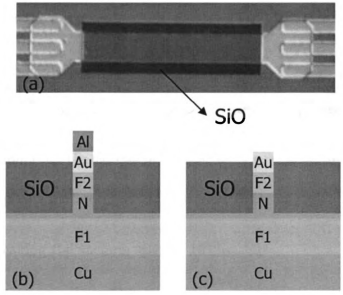

Figure 3.16: a) An optical image after SiO evaporation and lift-off. Scale as in Fig. 3.9. (b) A cross-sectional cartoon after SiO evaporation lift-off. (c) A cross-sectional cartoon after wet etch with KOH.

After lift-off we have some Al left on top of the nanopillar (see Fig. 3.16 (b)). We etch this Al by dipping the substrate in photodeveloper (452, KOH) for $\sim$ 4 minutes and rinse with DI water and blow-dry immediately. Fig. 3.16 (c) shows a cartoon of the cross-section of a nanopillar at this stage.

3.4.7 Top contacts

The final step is to put top contacts to the nanopillars. The following is a recipe for top contacts.

1. Spin 9% MMA at 4000 rpm for 30 seconds and bake for 5 minutes at 170°C.

2. Spin 2% PMMA at 4000 rpm for 30 seconds and bake for 30 minutes at 170°C.

3. Load the sample in the SEM and write the pattern in Figure 3.17. The beam current is 25 pA. The area dose is $130\mu C/cm^2$ for the inner patterns and $70\mu C/cm^2$ for the outer ones.

4. Develop the sample as described in section 3.4.2. Figure 3.18 (a) shows an image of the openings for the top contacts after development.

5. After developing put the sample in the ion-milling chamber and ion-mill the protruding Au pillars for 5 seconds to clean up the contact region of the nanopillars.

6. Without breaking the vacuum sputter 100nm Au.

7. Lift-off as described in section 3.4.3. Fig. 3.18 (b) shows an optical image of the center of the substrate after lift-off. Fig. 3.18 (c) shows a cartoon of a cross-section of a finished nanopillar device.

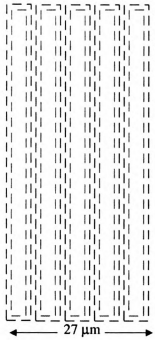

Figure 3.17: The DesignCAD drawing for top contacts to 5 nanopillars. The outer rectangles are exposed to less e-beam than the inner ones to get a good undercut.

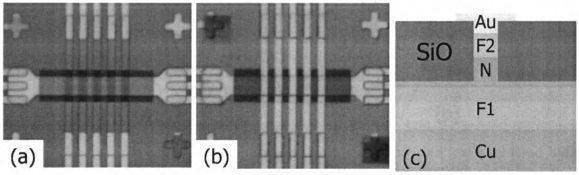

Figure 3.18: (a) Openings for 5 electrodes for top contacts created by EBL. (b) An optical image showing the multilayer, SiO insulating layer and 5 electrodes for top contacts. (c) A cartoon of a cross-section of finished nanopillar device. Scale as in Fig. 3.9.

3.4.8 Measuring the Resistances of Nanopillars

To measure the resistance of the nanopillars, we have to put indium on the Au pads of the substrate using a sharp tip soldering iron. Initially all the leads are shorted to protect the nanopillar from burning out in the case of a static electric discharge

from the operator. We mount the sample on a quick-dipper stick and solder the current and voltage leads as shown in Fig. 3.19 (a). To measure a specific nanopillar on the substrate, we scratch the shorting leads using a scriber. During soldering, and scribing, we ground ourselves by wearing a grounding wrist strap. For another level of protection, the quick-dipper has shorting switches, which are shorted until the measurement starts. We insert the sample in a room temperature electromagnet with magnetic poles bored out, which produces 820 Oe/A magnetic field. We place the sample at the center of the electromagnet as seen in Fig. 3.19 (b).

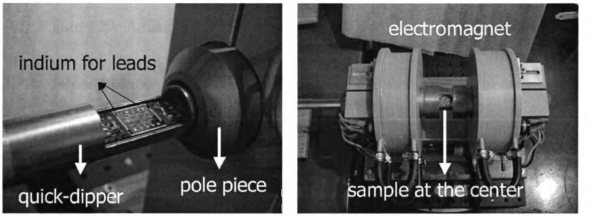

Figure 3.19: (a) The sample is mounted on the quick-dipper and leads soldered with indium. (b)Quick dipper is inserted into the electromagnet through the bored pole pieces and the sample is positioned at the center of the electromagnet.

We connect the current leads to the dc current source and the voltage leads to the pre-amplifier. We built our own battery-powered dc current source the magnitude of the output of which is set at 1.98 mA dc current per volt supplied by the lock-in (see Fig. 3.20). The preamplifier sends the amplified ac voltage signal from the sample to the lock-in amplifier's input. The differential resistance dV/dI is measured by the lock-in amplifier at frequency 8 kHz, ac measuring current $\sim 20\mu$A, and time constant

100 ms.

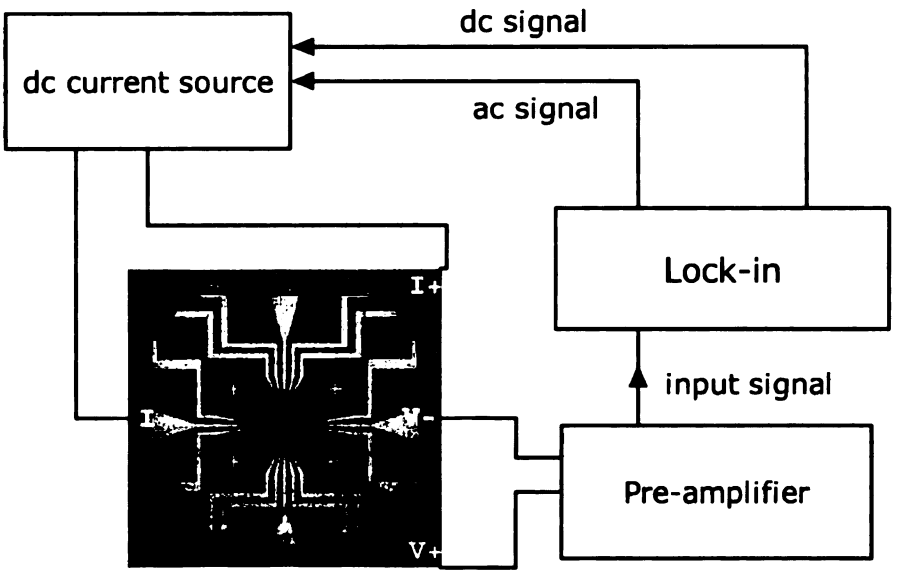

Figure 3.20: A diagram of resistance measurement using lock-in detection.

A computer running Labview controls the power supply for the electromagnet and the lock-in. The measurement is fully computer controlled. We first measure dV/dI vs. the external magnetic field H (applied along the easy axes of nanopillars) of the nanopillar to get an idea how good the sample is, i.e. if it has well defined parallel (P) and anti-parallel (AP) states. For our specific samples we usually sweep the field in steps between -1 kOe and +1 kOe. Then we sweep the dc current in steps passing through the nanopillar to check for the current driven phenomenon. dV/dI vs. I is measured with an effective sweep rate about 0.1 mA/s, calculated from a current step of 0.1 mA and step time 10 times the lock-in time constant. Positive current I^+ represents current flow from thick F1 to thin F2 i.e. electron flow from F2 to F1. We do two kinds of measurement:

1. We keep the current fixed and sweep the magnetic field, which gives CPP-MR data.

2. We keep the magnetic field fixed and sweep the dc current, which gives CIMS data.

For example, Fig. 3.21 shows the CPP-MR and CIMS data of a Py/Cu/Py nanopillar at room temperature. Noticeably, the change in the resistance, $\Delta R = R(\mathrm{AP})\text{-}R(\mathrm{P})$, of the sample is the same for both types of switching. The upward curvatures in the CIMS data for large current are due to joule heating.

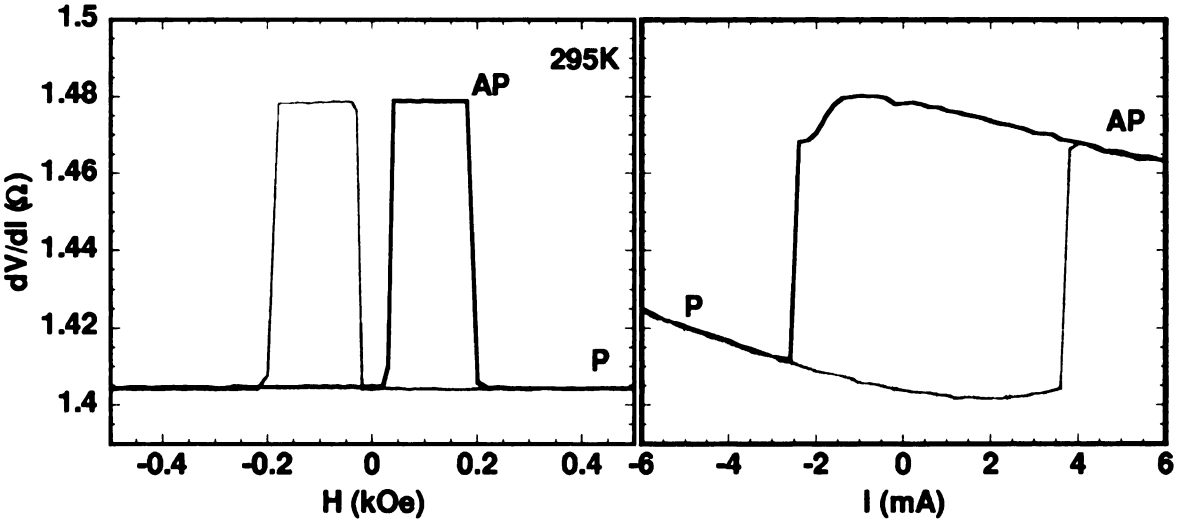

Figure 3.21: Differential resistance (dV/dI) vs. H of a Py/Cu/Py nanopillar while I=0 (on the left). dV/dI vs. the dc current (I) while $H = 0$ for the same sample.

We can also measure at 4.2K by dipping the quick-dipper into liquid helium. In this case we use a superconducting solenoid magnet with a persistent switch to provide the external magnetic field. The persistent switch of the superconducting magnet is also controlled by the computer.

Chapter 4

Spin-memory-loss in sputtered Pd,Pt and Au and at their interfaces with Cu at 4.2K

4.1 Introduction

Spin-dependent bulk and interface scattering in ferromagnetic/nonmagnetic (F/N) structures are the sources of Giant Magnetoresistance (GMR). Such scattering also results in spin-memory-loss through spin-flipping both in the layers and at interfaces. The main parameter characterizing the spin-memory-loss and therefore determining the MR is the spin-diffusion (spin-flipping) length l_{sf} that is the distance an electron diffuses before its spin flips. Currently there is no experiment that can directly give the amount of spin-flipping at a F/N interface (see, however, [68]). However, hoping to get insight into the spin-flipping at F/N interfaces, Park et al. [93] developed a method to measure the spin-flipping at N1/N2 interfaces. Park et al. [93] studied spin-memory-losses in sputtered Ag, V, Nb and W and at Ag/Cu, V/Cu, Nb/Cu and W/Cu interfaces at 4.2K. They also measured the interface specific resistances of N1/N2 to look for patterns to see if the interface specific resistances could be estimated from interfacial alloying of N1 and N2. In this chapter, we extend these studies to

determine the spin-diffusion lengths in sputtered Pd, Pt and Au and spin-memory-losses at Pd/Cu, Pt/Cu and Au/Cu interfaces at 4.2K using the same method given in Ref.[93].

Special interest in the transport properties of Pt and Pd layers, and Pt- and Pd-based multilayers, derives from several sources: the high polarizability of Pd, the large atomic number of Pt, and that both produce magnetic anisotropies perpendicular to the layer planes when very thin layers of these metals and Co are combined in multilayers [94]. To evaluate whether either metal could be used in magnetic multilayers displaying GMR, it is necessary to know their transport properties.

So far, studies of CPP-MR in F/N multilayers involving noble metals have focused upon the N-metals Cu or Ag [61]. Studies of the "inverse" phenomena, current-induced moment switching or magnon generation in F/N trilayers or multilayers, have also concentrated upon Cu [37, 95, 96]. For uses such as electron-beam lithographic fabrication of nanowires, Au has the advantage over Cu and Ag that it does not oxidize. If Au as the N-metal has small enough resistivity, and long enough spin-flipping length (spin-diffusion length), and if it produces CPP-MRs comparable to those for Cu and Ag, it could be advantageous for both scientific studies and devices.

In this chapter, we first describe the spin-memory-loss detection technique and then the experiments. Later, we divide the studies into two sections. The first section involves the spin-memory-loss in Pd and Pt, and at Pd/Cu and Pt/Cu interfaces. To test the effect of spin-orbit scattering, we compare the spin-memory-losses at Pd/Cu and Pt/Cu with Nb/Cu and W/Cu, respectively, as Pd and Nb are in the 5th, and Pt and W are in the 6th row of the periodic table. The second section involves the

spin-memory-loss in Au and at Au/Cu interfaces. To check whether Au as a spacer layer gives comparable CPP-MR to Cu and Ag, we compare the MRs of Co-based exchange-biased spin valves with Au,Cu and Ag spacer layers. We also compare the spin-memory-losses at Au/Cu and Pt/Cu interfaces to test whether the dominant source of spin-flipping is the spin-orbit scattering. If so, then the heavy metals like Pt and Au should give large spin-flipping and therefore short l_{sf}. In addition, we also include a comparison between our results and later theoretical calculations of interface specific resistances by Xia et al.[97, 98]. Most parts of this chapter are published in Ref. [99] and [100].

4.2 Spin-memory-loss detection technique

We obtain the interface resistances and spin-memory-loss results using a CPP "spin-memory-loss detector"[101, 93, 61], which is a Py-based exchange-biased spin-valve (EBSV) sandwiched between two Nb strips.

The structure of the CPP spin-memory-loss detector is:

Nb(200)/Cu(10)/FeMn(8)/Py(24)/Cu(10)/X/Cu(10)/Py(24)/Cu(10)/Nb(200),

where all the thicknesses are in nanometers. At 4.2K the Nb superconducting leads provide a uniform current through a well defined area A. The magnetization of one 24 nm thick Py layer is pinned by an 8 nm thick adjacent antiferromagnetic FeMn layer, and the magnetization of the other 24 nm thick Py layer is free to rotate from parallel (P) to antiparallel (AP) to that of the pinned layer in a small magnetic field (~20 Oe) [101, 93]. X is either a single layer N-metal or a multilayer of alternating N1/N2 metals to be studied. We measure the specific resistances (area

of CPP current flow A times resistance R) AR(AP) and AR(P), as well as their difference, $A\Delta R = AR(\mathrm{AP}) - AR(\mathrm{P})$. By varying the thickness of a single layer of N-metal (t_{N}) or varying the number of bilayers (N) of N1/N2, one can make a plot of $A\Delta R$ vs. t_{N} or N. Valet-Fert [12] analysis of these plots give the spin-memory-loss in bulk N-metal or at N1/N2 interfaces. For the spin-memory-loss detector $A\Delta R$ decays exponentially due to the spin-flipping as:

- If X is a single layer N-metal with thickness t_{N}, then $A\Delta R \propto \exp(-t_{\mathrm{N}}/l_{sf}^{\mathrm{N}})$, where l_{sf}^{N} is the spin diffusion length in N-metal.

- If X is an alternating multilayer of N1/N2 with N bilayers, then $A\Delta R \propto \exp(-2N\delta_{\mathrm{N1/N2}})$, where $\delta_{\mathrm{N1/N2}}$ measures the spin-memory-loss at an N1/N2 interface [93, 61].

The interface specific resistance $AR_{\mathrm{N/Cu}}$ is derived from the slope of $AR(AP)$ vs. N graph for X=[N/Cu]$_N$ inserts, which is given by

$$2AR_{\mathrm{N/Cu}} + \rho_{\mathrm{N}} t_{\mathrm{N}} + \rho_{\mathrm{Cu}} t_{\mathrm{Cu}}, \tag{4.1}$$

where the factor of 2 comes from 2 interfaces for one layer of N-metal.

For X=N(t) inserts, $A\Delta R$ first drops fast due to the formation of two N/Cu interfaces then continues to decrease more slowly as t_{N} increases. To derive l_{sf}^{N} we analyze the data for thicknesses larger than the total thickness of the two N/Cu interfaces ($2t_{\mathrm{N/Cu}}$), which include a constant contribution from two N/Cu interfaces in addition to the contribution from bulk N-layers. The VF equation for an EBSV with a single N-metal insert with thickness t_{N} reduces to

$$A\Delta R \propto \frac{\exp\left(-\frac{t_N}{l_{sf}^N} - 2\delta_{N/Cu}\right)}{AR_{active}(AP)} \tag{4.2}$$

For the Py-based EBSV, since $l_{sf}^{Py} \ll t_{Py}$ the $AR_{active}(AP)$ includes only the "active" region in the EBSV that is bounded by the amount of l_{sf}^{Py} in the 24 nm thick Py-layers and the inserts between them (see Chapter 2). Therefore the denominator in Eqn. 4.2 includes an additional specific resistance $\rho_N t_N + 2AR_{N/Cu}$.

Similarly, the VF equation for the EBSVs with X=$[N/Cu]_N$ inserts reduces to

$$A\Delta R \propto \frac{\exp\left[-\left(2\delta_{N/Cu} + \frac{t_N}{l_{sf}^N} + \frac{t_{Cu}}{l_{sf}^{Cu}}\right)N\right]}{AR_{active}(AP)} \tag{4.3}$$

The denominator of Eqn. 4.3 includes an additional specific resistance $N(\rho_N t_N + \rho_{Cu} t_{Cu} + 2AR_{N/Cu})$ because the X=$[N/Cu]_N$ insert is in the active region. Since l_{sf}^N and $\delta_{N/Cu}$ appear simultaneously in Eqns. 4.2 and 4.3, we find their values by self-consistent numerical fits to our data. For the numerical VF analysis, the parameters for the other constituents of the Py-based EBSV are: $\rho_{Py} = 123$ nΩm, $\beta_{Py} = 0.73$, $\rho_{Py}^* = 263.3$ nΩm, $l_{sf}^{Py} = 5.5$ nm, $\gamma_{Py/Cu} = 0.7$, $2AR_{Py/Cu}^* = 1.00 \pm 0.08$ fΩm^2, $\rho_{FeMn} = 875 \pm 50$ nΩm and $AR_{FeMn/Py} = 1.0 \pm 0.4$ fΩm^2 taken from Ref. [102], whereas ρ_N is measured using the van der Pauw technique (see Appendix A). This method can be used to determine the spin-memory-loss at any N1/N2 interface, but in that case the interface specific resistances and spin-memory-loss of both N1/Cu and N2/Cu must be known.

4.3 Experiment

The samples are sputter deposited onto (100) Si substrates. The details of our sample fabrication and measurement techniques are described in Section 3.1. To study the spin-memory-loss within the Pd, Pt and Au layers, we inserted certain thicknesses (1-20 nm) of each in the spin-memory-loss detector as described in Section 4.2. To study the spin-memory-loss at the Pd/Cu, Pt/Cu and Au/Cu interfaces we inserted $[\text{Pd(3nm)/Cu(3nm)}]_N$, $[\text{Pt(3nm)/Cu(3nm)}]_N$ and $[\text{Pt(3nm)/Cu(3nm)}]_N$ bilayers in the spin-memory-loss detector. We chose to make 3 nm thick layers of Pd, Pt, Au and Cu to eliminate the possibility of pin holes within the sputtered layers of these metals. The measuring uncertainties in individual values of AR(AP) (and in the larger values of $A\Delta R$) are dominated by a $\pm 5\%$ uncertainty in our ability to determine the area A. Uncertainties in $A\Delta R$ much larger than this value are indicated by error bars. Data fluctuations illustrate the reproducibilities of AR(AP) or $A\Delta R$ for independent samples. We also made 300 nm thick sputtered thin films of Pd and Pt and 200 nm thick Au films to measure their resistivities. The van der Pauw measurements of sputtered Pd, Pt and Au films at 4.2K gave residual resistivities of $\rho_{Pd} = 40 \pm 3$ nΩm, $\rho_{Pt} = 42 \pm 6$ nΩm, and $\rho_{Au} = 19 \pm 6$ nΩm (see Appendix A).

The typical sputtering rates for the constituents of the spin-memory-loss detector are given in Table 4.1. The sputtering rates for the metals given in Table 4.1 are not exactly the same for every sample but within 10% of those listed in Table 4.1. The main reason for these variations is the gradual reduction in the volume of the sputtering targets. All metals except FeMn are dc-triode sputtered using 2″ diameter

targets. FeMn is dc-magnetron sputtered using a 1″ diameter target, therefore the deposition rate of FeMn is much smaller.

Metal	Nb	Py	FeMn	Cu	Pd	Pt	Au
Deposition Rate (Å/s)	5.5	5.5	0.5	10	4.5	7	5

Table 4.1: Typical sputter deposition rates of Nb, Py, FeMn, Cu, Pd, Pt and Au.

4.3.1 Examples of $AR(H)$ with X inserts

As examples of our data, Fig. 4.1 shows the resistive "hysteresis curves", $AR(H)$s, for EBSVs with no insert and 10 nm thick inserts of Pd, Pt and Au. Fig. 4.1 (a), (b) and (d) show both minor loops, where the pinned layer remains pinned, and major loops, when the field H is raised until the pinned layer unpins. Notice that both major and minor loops show the same constant values of $AR(AP)$ as H increases. Also, the values of $AR(P)$ are the same for large positive and negative fields. The switching fields of the pinned Py-layer are different for magnetic fields applied in different directions due to the shift in the hysteresis curve of the pinned Py-layer. The decreases in $A\Delta R$ from (a) to (b), (c), or (d) are due to the spin-flipping in the bulk and the formation of two Pd/Cu, Pt/Cu or Au/Cu interfaces. $A\Delta R$ for the sample in Fig. 4.1 (c) is very small due to the strong spin-flipping in both the 10 nm thick Pt insert and the two Pt/Cu interfaces. To measure such small changes, we measure the resistance at a fixed field 100 times and take the average. Since the EBSVs are in the AP state at 50 Oe and in P state at -200 and 400 Oe (see Fig. 4.1 (a), (b) and (d)), we measured the resistance of this sample first at -200 Oe, where the magnetizations of Py-layers are aligned parallel, then at 50 Oe, where the magnetization of the free Py-layer is flipped causing an anti-parallel alignment

and finally at 400 Oe, where both magnetizations are again aligned parallel. We also repeated these measurements one more time in the same order as before.

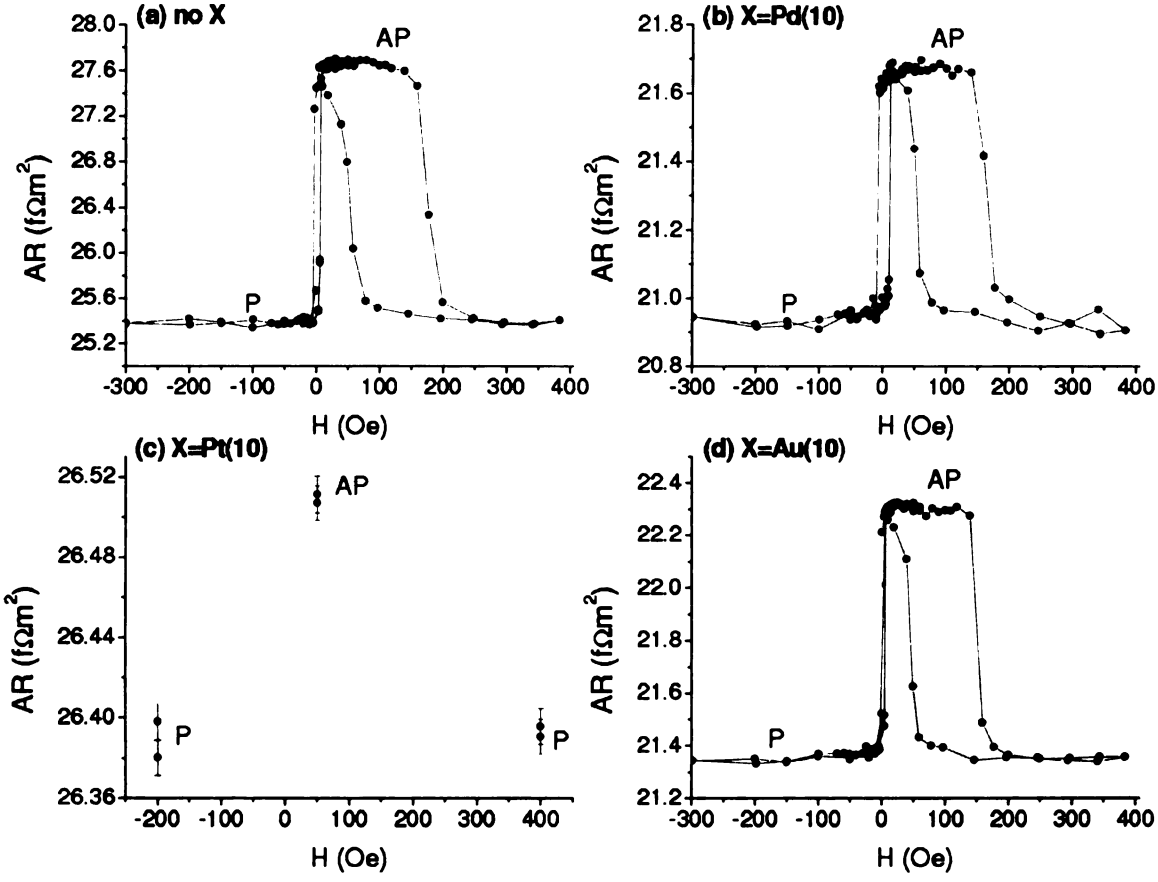

Figure 4.1: Examples of AR vs. H for Py-based EBSVs (a) with no insert X, (b) X=Pd(10), (c) X=Pt(10) and (d) X=Au(10)

Fig. 4.2 shows examples of variations in $AR(H)$ vs. N of EBSVs with $[\text{Pd(3)/Cu(3)}]_N$ inserts. Fig. 4.3 shows examples of variations in $AR(H)$ vs. N of EBSVs with $[\text{Pt(3)/Cu(3)}]_N$ inserts.

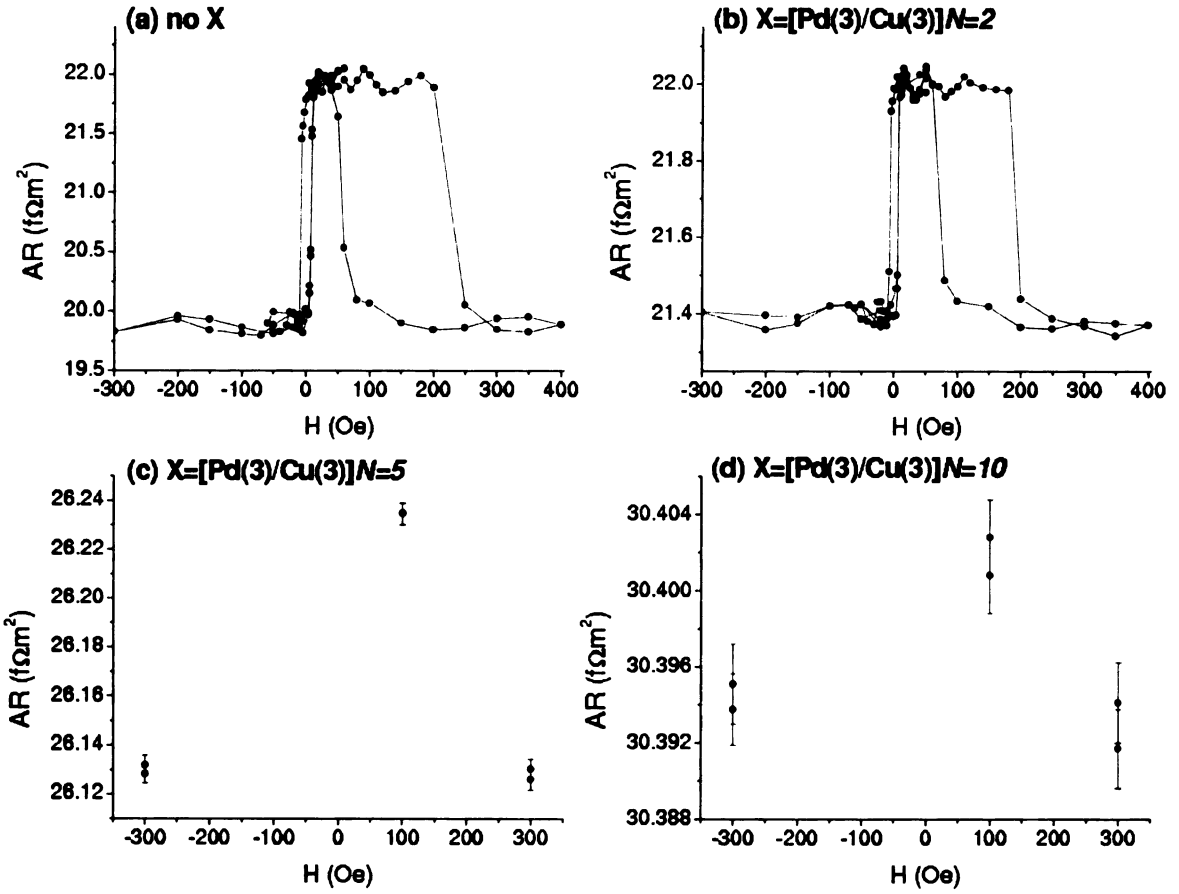

Figure 4.2: ARs vs. H for some EBSV samples (a) with no insert X (b) with X=[Pd(3)/Cu(3)]$_{N=2}$ (c) with X=[Pd(3)/Cu(3)]$_{N=5}$ (d) with X=[Pd(3)/Cu(3)]$_{N=10}$. Each data point in (c) and (d) represents an average of 100 measurements, and each error bar represents the standard deviation of the mean.

4.4 Spin-Memory-Loss at 4.2K in Sputtered Pd, Pt, and at Pd/Cu and Pt/Cu interfaces

We start with inserts of just Pd or Pt. Fig. 4.4 shows $A\Delta R$ vs. thickness, t_{Pd} or t_{Pt}, of Pd (filled triangles and solid curve) or Pt (filled diamonds and solid curve). For comparison, we show also previously published data for inserts of Nb (open triangles and dashed curve) and W (open diamonds and dashed curve) [93]. In all four cases, $A\Delta R$ behaves as expected, first decreasing rapidly as the two interfaces with Cu form (due both to the additional resistance of these interfaces and to spin-memory loss at

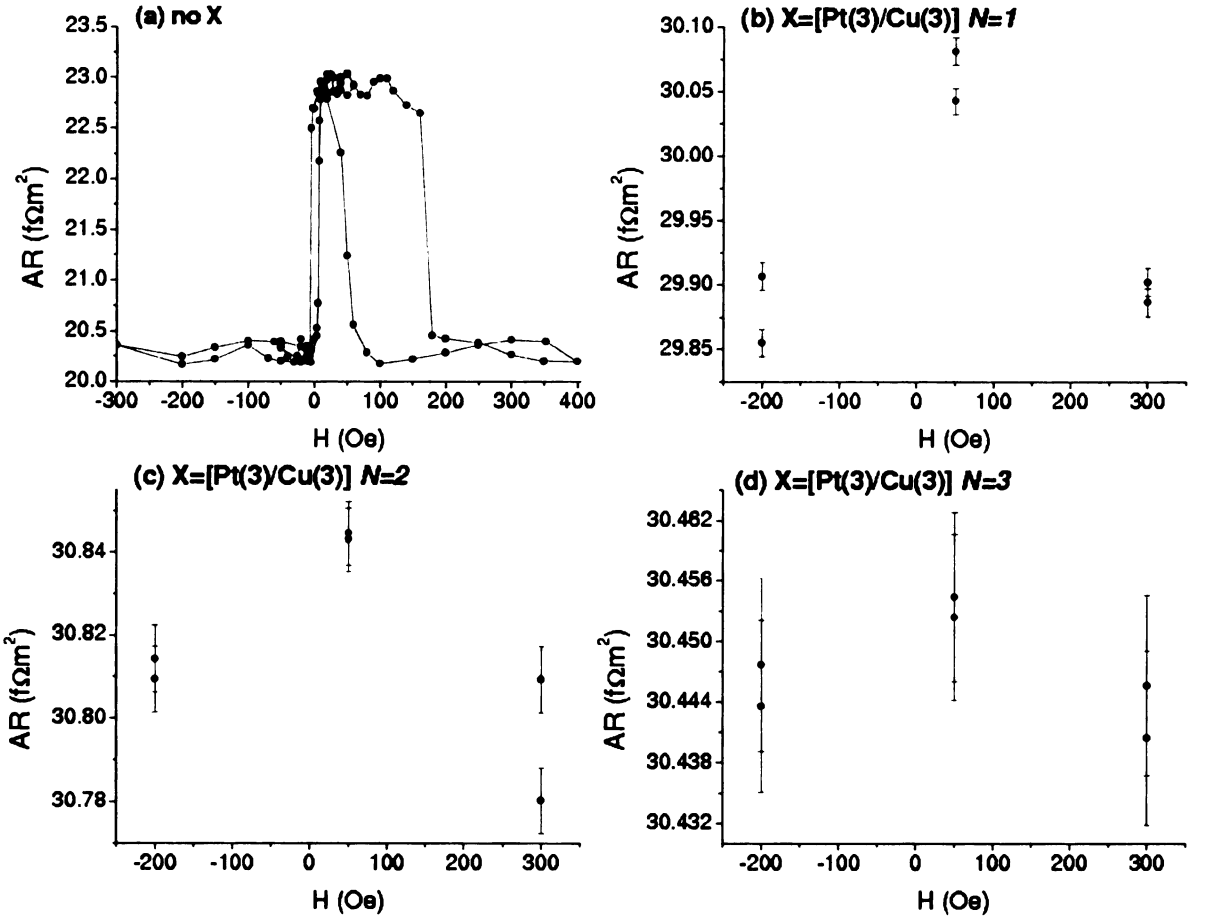

Figure 4.3: *AR*s vs. H for some EBSV samples (a) with no insert X (b) with X=[Pt(3)/Cu(3)]$_{N=1}$ (c) with X=[Pt(3)/Cu(3)]$_{N=2}$ (d) with X=[Pt(3)/Cu(3)]$_{N=3}$. Each data point in (b), (c) and (d) represents an average of 100 measurements, and each error bar represents the standard deviation of the mean.

the interfaces), and then more slowly due to spin-memory loss (finite spin-diffusion length) in the bulk metal. The fits of the Pd and Pt data in the large t regimes give l_{sf}^{Pd}=25^{+10}_{-5} nm and l_{sf}^{Pt} =14 ± 6 nm, where the larger uncertainty on the "up side" for Pd arises because the technique is less reliable when l_{sf} is larger than the largest layer thickness (20 nm) used. These values are comparable to those for Nb and W, l_{sf}^{Nb} =$25^{+\infty}_{-5}$ nm and l_{sf}^{W} = 4.8 ± 1 nm [93]. They are also comparable to the mean-free

paths $\lambda_{Pd} = 21 \pm 5$ nm and $\lambda_{Pt} = 20 \pm 6$ nm estimated from the equation

$$\lambda(\text{nm}) = \frac{(700 \rightarrow 1000)\text{f}\Omega\text{m}^2}{\rho}, \tag{4.4}$$

where the residual resistivity ρ is in nΩm [103]. Comparable values of l_{sf} and λ can be understood if the defects producing the residual resistivities are much lighter than Pd and Pt, because the large atomic number difference between the host and scatterer should produce strong spin-orbit scattering, but the likely small differences (almost unity) in the number of transport electrons/atom should produce only modest transport scattering. For example, the mirror image case of Pd or Pt impurities in Cu gives only moderate residual resistivities per atomic percent impurity ($\sim 1\mu\Omega$cm/at.% for Pd and $\sim 2\mu\Omega$cm/at.% for Pt), [103] but relatively large spin-orbit cross sections, $\sigma_{so} \sim 2.5 \times 10^{-18}$ cm^2 for Pd and $\sim 4 \times 10^{-17}$ cm^2 for Pt [104]. Putting appropriate values from Refs. [103] and [104] into the Valet-Fert [12] equation

$$l_{sf} = \sqrt{\frac{\lambda\lambda_{so}}{6}}, \tag{4.5}$$

which relates l_{sf} to the product of the transport mean-free path λ and the spin-orbit mean-free path λ_{so}, gives estimates of $l_{sf}/\lambda \sim 1$ for Pt in Cu and ~ 2.5 for Pd in Cu.

The curves shown in Fig. 4.4 are fits to all of the data by means of numerical solutions of the appropriate equations of Valet and Fert [12] using the independently determined values of the properties of the EBSV from Ref. [102], the van der Pauw layer resistivities for Pd and Pt noted above, and the interface specific resistances from the data shown in Fig. 4.5, plus values of l_{sf}^{N} and $\delta_{\text{N/Cu}}$ found self-consistently from the data of Fig. 4.4 and the data for multilayer inserts in Fig. 4.6. As we will

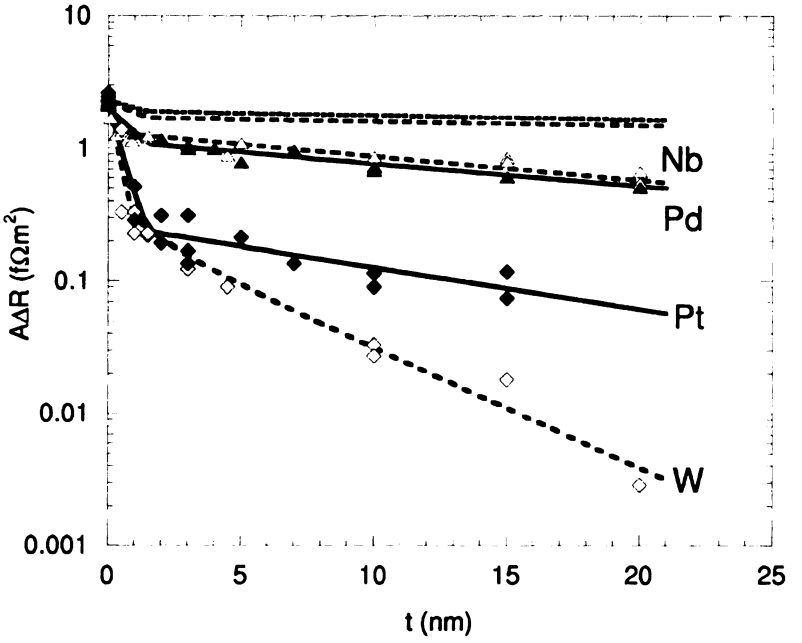

Figure 4.4: $A\Delta R$ vs. t_{Pd} or t_{Py} for Pd (filled triangles and solid curve), Pt (filled diamonds and solid curve), Nb (open triangles and dashed curve), and W (open diamonds and dashed curve). The dotted curves represent the behaviors of $A\Delta R$ expected for no spin-memory-loss in either the bulk Pd or Pt or at the Pd/Cu or Pt/Cu interfaces.

describe below, the self-consistent solution for Pd yields a slightly different value of $l_{sf}^{Pd} = 27$ nm, which lies within the uncertainty of the simpler fit described above.

Fig. 4.5 shows how AR(AP) increases with an increase in N for inserts of $[\text{Pt(3)/Cu(3)}]_N$ and $[\text{Pd(3)/Cu(3)}]_N$, as well as for $[\text{Nb(3)/Cu(3)}]_N$ and $[\text{W(3)/Cu(3)}]_N$. Least-squares straight line fits to the data give (after correcting for the contributions of the 3 nm thick Pd, Pt, and Cu layers) $2AR_{Pd/Cu} = 0.9 \pm 0.1$ fΩm^2 and $2AR_{Pt/Cu} = 1.5 \pm 0.1$ fΩm^2. These values are smaller than those for $2AR_{Nb/Cu} = 2.2 \pm 0.3$ fΩm^2 and $2AR_{W/Cu} = 3.1 \pm 0.2$ fΩm^2. If these ARs are due simply to interfacial alloying, then they are consistent with the smaller resistivities per atomic percent impurity given in Ref. [103] for Cu with Pd ($\sim 1\mu\Omega$cm/at.% impurity) and Pt ($\sim 2\mu\Omega$cm/at.% impurity) than those for Cu with Mo (we use Mo here because no value is given in [103]

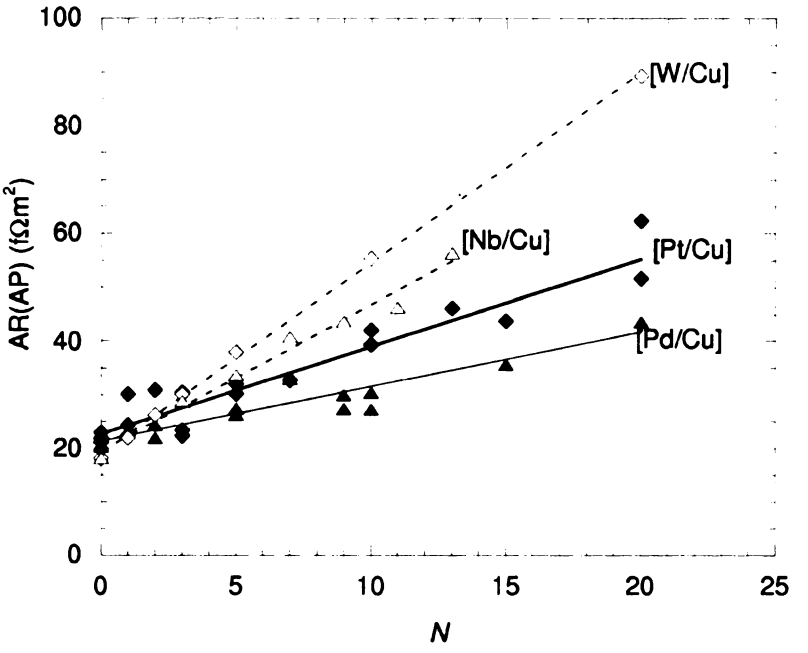

Figure 4.5: AR(AP) vs. N for $[Pd/Cu]_N$ and $[Pt/Cu]_N$ inserts compared with $[Nb/Cu]_N$ and $[W/Cu]_N$. The symbols are the same as in Fig. 4.4. The lines are least square fits.

for Nb in Cu) and W (both $\sim 4\mu\Omega$cm/at.% impurity). But such a simple comparison should be treated cautiously, both because the thicknesses of the interfacial alloys might differ for the different metal pairs, and because band structure effects could be important [105, 97].

Last, Fig. 4.6 compares the decreases in $A\Delta R$ vs. N for inserts of $[Pd(3)/Cu(3)]_N$ or $[Pt(3)/Cu(3)]_N$ with similar data for $[Nb(3)/Cu(3)]_N$ and $[W(3)/Cu(3)]_N$. Simple linear fits to the data in the form $\ln(A\Delta R)$ vs. N determine values (after correcting for spin-flipping in the Pt or Pd layers) of $\delta_{Pd/Cu} = 0.24^{+0.06}_{-0.03}$ and $\delta_{Pt/Cu} = 0.9 \pm 0.1$, where we've allotted greater uncertainty toward large $\delta_{Pd/Cu}$ (i.e., we have determined this uncertainty by underweighting the data points for large N). These values of $\delta_{Pd/Cu}$ and $\delta_{Pt/Cu}$ are comparable to those of $\delta_{Nb/Cu} = 0.19 \pm 0.05$ and $\delta_{W/Cu} = 0.96 \pm 0.1$, respectively. If spin-orbit scattering in alloyed interfaces is the dominant source of

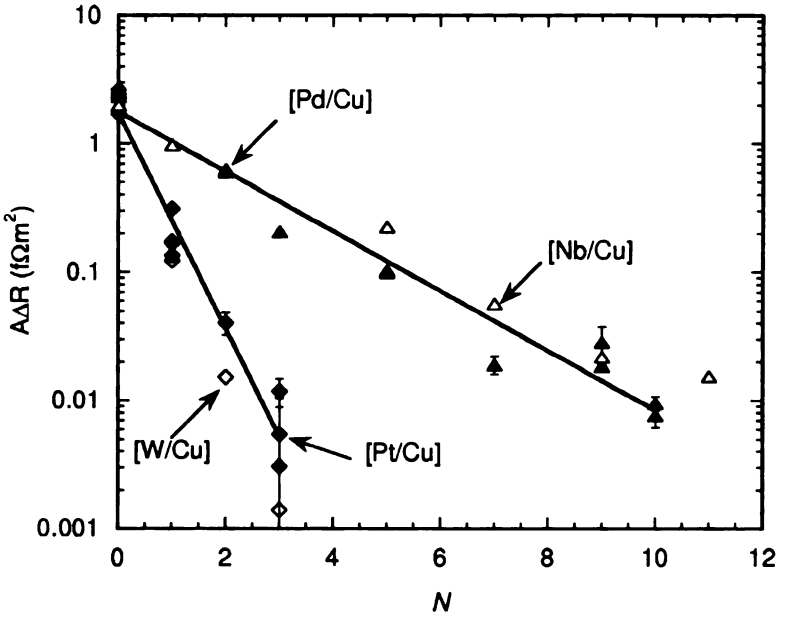

Figure 4.6: $A\Delta R$ vs. N for $[Pd/Cu]_N$, $[Pt/Cu]_N$, $[Nb/Cu]_N$, and $[W/Cu]_N$ inserts. Note the similarity of behaviors of $[Pd/Cu]_N$ and $[Nb/Cu]_N$ and of $[Pt/Cu]_N$ and $[W/Cu]_N$. The symbols are the same as in Fig. 4.4. The lines are least square fits.

δ, then we would expect $\delta_{Pd/Cu} \approx \delta_{Nb/Cu}$ and $\delta_{Pt/Cu} \approx \delta_{W/Cu}$, since Pd and Pt are, respectively, in the same chemical rows in the periodic table as Nb and W. Indeed, these pairs of data sets in Fig. 4.6 are very similar. Again, however, band structure details may complicate the analysis.

If we simply combine the best fit values of $\delta_{Pd/Cu}$ and $\delta_{Pt/Cu}$ with the best fit values of $l_{sf}^{Pd} = 25$ nm and $l_{sf}^{Pt} = 14$ nm from an equivalent fit to the data in Fig. 4.4, then the resulting Valet-Fert analysis of the data in Fig. 4.4 falls above the data. That is, these best fit values of δ are slightly too small to account for the reduction in $A\Delta R$ in Fig. 4.4 due to the formation of Pd/Cu and Pt/Cu interfaces. The curves shown in Fig. 4.4 use the alternative parameters $l_{sf}^{Pd} = 27$ nm, $l_{sf}^{Pt} = 14$ nm, $\delta_{Pd/Cu} = 0.30$, and $\delta_{Pt/Cu} = 0.99$. Since all four values lie within the uncertainties in the original values, we retain the original values and their uncertainties as our best estimates.

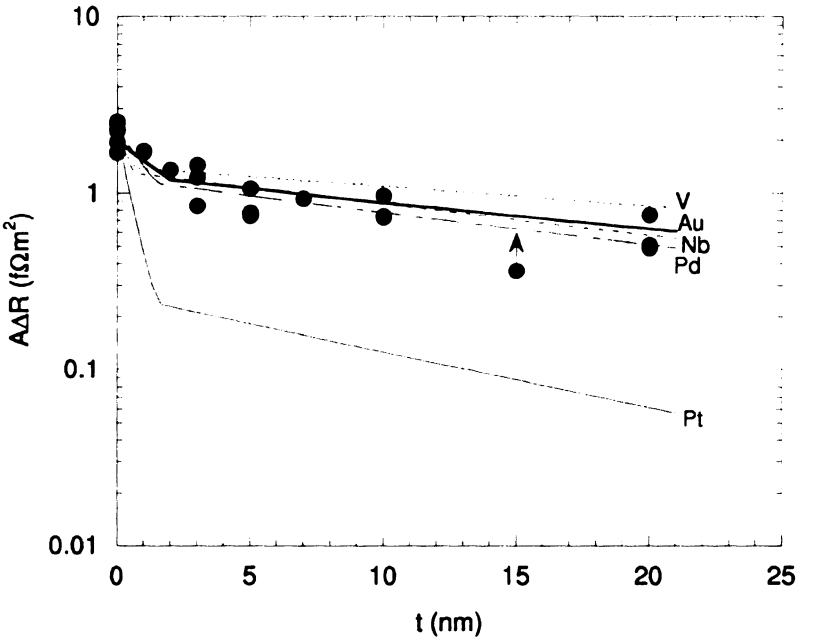

Figure 4.7: $A\Delta R$ vs. t_N for N = Au (filled circles and thick solid curve), V (dotted curve), Nb (dashed curve), Pd (broken curve), and Pt (thin solid curve). The datum at $t_{Au} = 15$ nm is only a lower bound, as its $AR(H)$ curve did not give a flat AR(AP) region. That point is not included in the fit to the Au data.

4.5 Spin-Memory-Loss and CPP-MR at 4.2K in Sputtered Multilayers with Au

Fig. 4.7 shows $A\Delta R$ vs. Au thickness, t_{Au}. For comparison, we show also the best fit curves to previously published data for inserts of V (dotted curve), Nb (dashed curve) [93], Pd (broken curve) and Pt (thin solid curve). In all cases, $A\Delta R$ behaves as expected, first decreasing rapidly as the two interfaces with Cu form (due both to the additional resistance of these interfaces and to spin-memory loss at the interfaces), and then more slowly due to spin-memory loss (finite spin-diffusion length) in the bulk metal. The slope of the Au data in the large t_{Au} regime gives $l_{sf}^{Au} = 35^{+65}_{-5}$ nm, where the uncertainty on the high side is large because the technique is less sensitive to values of l_{sf}^{Au} much larger than the largest layer thickness used (here $t_{Au} = 20$ nm).

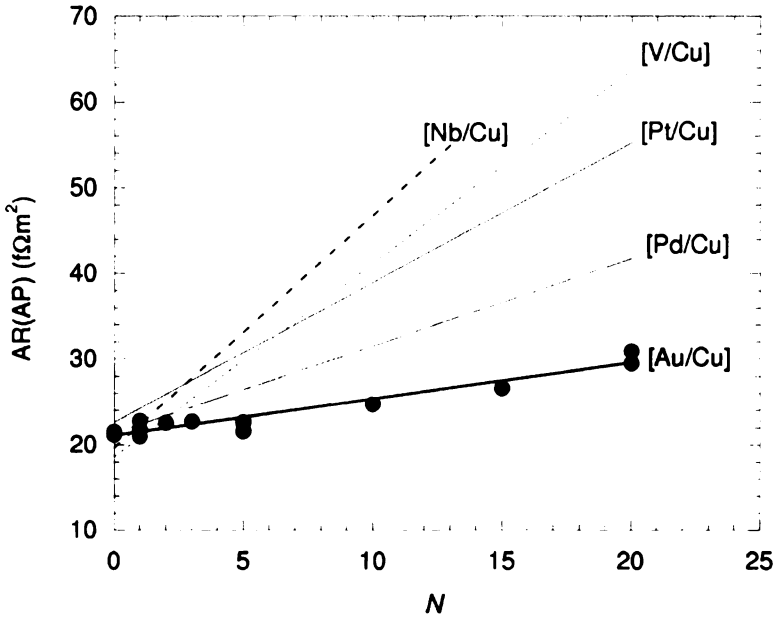

Figure 4.8: AR(AP) vs N for $[Au/Cu]_N$ inserts compared with $[V/Cu]_N$, $[Nb/Cu]_N$, $[Pd/Cu]_N$, and $[Pt/Cu]_N$. The symbols and lines are the same as in Fig. 4.7.

Such a range of values is comparable to those for V, Nb, and Pd, but smaller than for Pt [93, 99].

The curves in Fig. 4.7 are fits to all of the data by means of numerical solutions of the appropriate equations of Valet and Fert [12] using the independently determined values of the properties of the EBSV given in Ref. [102], the van der Pauw layer resistivities (for Au, the value given above), and the interface specific resistances and values of δ from the data in Figs. 4.8 and 4.9. To obtain the Au fit shown, we used $l_{sf}^{Au} = 35$ nm and $\delta_{Au/Cu} = 0.20$, the latter near the upper range of uncertainty of $\delta_{Au/Cu}$ (see later). The curve using the best fit to Fig. 4.9 alone, $\delta_{Au/Cu} = 0.13$, would have essentially the same "slope", but would fall above the data.

Fig. 4.8 shows how AR(AP) increases with increasing N for inserts of $[Au(3)/Cu(3)]_N$ as well as for $[V(3)/Cu(3)]_N$, $[Nb(3)/Cu(3)]_N$, $[Pd(3)/Cu(3)]_N$, and $[Pt(3)/Cu(3)]_N$. A least-squares straight line fit to the Au data gives (after correcting for the con-

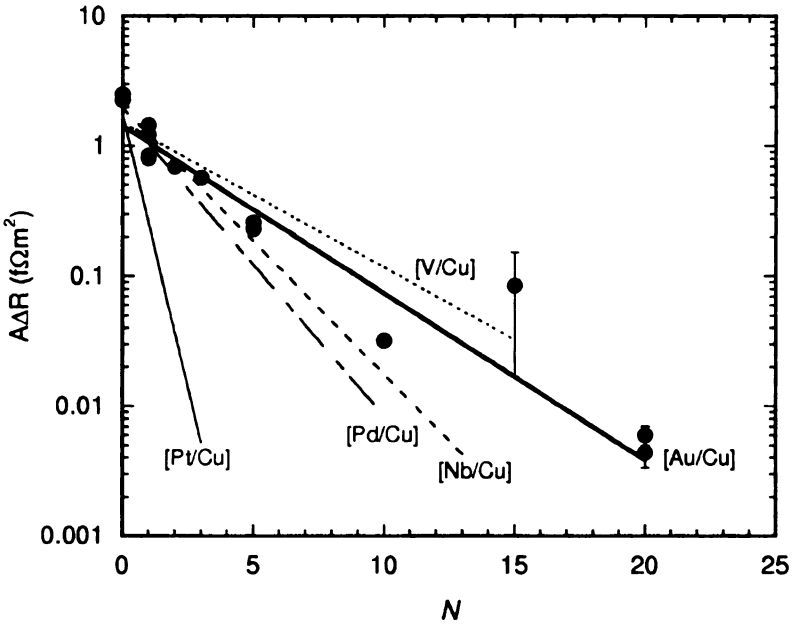

Figure 4.9: $A\Delta R$ vs. N for $[Au/Cu]_N$, $[V/Cu]_N$, $[Nb/Cu]_N$, $[Pd/Cu]_N$, and $[Pt/Cu]_N$ inserts. The symbols and lines are the same as in Fig. 4.7. $A\Delta R$ for the $N = 15$ datum dropped by a factor of ten over three successive measurements. We show the average and fluctuations, but neglect this point in our fit. In contrast, repeated measurements of the $N = 10$ and 20 data remained stable to within the uncertainty bars shown.

tributions of the 3 nm thick Au and Cu layers), $2AR_{Au/Cu} = 0.35^{+0.10}_{-0.05}$ fΩm^2, which overlaps within mutual uncertainties of the value $2AR_{Au/Cu} = 0.30 \pm 0.01$ fΩm^2 previously derived using a completely different method [106]. $AR_{Au/Cu}$ is smaller than $AR_{V/Cu}$, $AR_{Nb/Cu}$, [7], $AR_{Pd/Cu}$ and $AR_{Pt/Cu}$ [99].

Fig. 4.9 compares $A\Delta R$ vs. N for $[Au(3)/Cu(3)]_N$ $[V(3)/Cu(3)]_N$, $[Nb(3)/Cu(3)]_N$, $[Pd(3)/Cu(3)]_N$, and $[Pt(3)/Cu(3)]_N$ inserts. Self-consistent VF analyses of the data for $[Au(3)/Cu(3)]_N$ and the data in Figs. 4.7 and 4.8 give $\delta_{Au/Cu} = 0.13^{+0.08}_{-0.02}$, larger than for $[V/Cu]_N$, but smaller than for $[Nb/Cu]_N$, $[Pd/Cu]_N$, and $[Pt/Cu]_N$ [93, 99]. The curve shown for Au/Cu is for $\delta_{Au/Cu} = 0.13$, the best fit to the data of Fig. 4.9 alone. The value of $\delta_{Au/Cu} = 0.20$ used in Fig. 4.7 would correspond to a line going just above the datum at $N = 10$. Given the small values of $A\Delta R$ for $N = 20$, such a

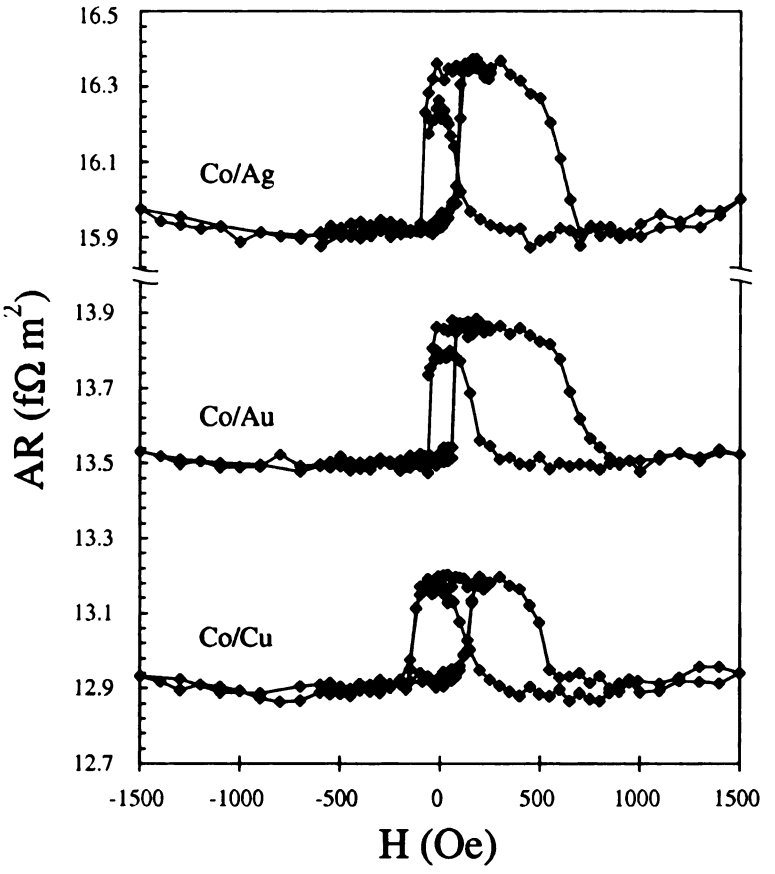

Figure 4.10: $AR(H)$ vs. H for representative Co/Ag, Co/Au, and Co/Cu EBSVs with $t_{Co} = 6$ nm and $t_N = 10$ nm for N = Ag, Au, or Cu. The data around $H = 0$ overlap for minor and major loops; the former extend up to about + 250 Oe, the latter to + 1500 Oe.

line cannot be ruled out.

Finally, to illustrate the size of the CPP-MR for Co/Au, Fig. 4.10 compares representative hysteresis curves of $A\Delta R$ vs. H for Co-based EBSVs with Co thickness, $t_{Co} = 6$ nm, and fixed thickness $t_N = 10$ nm for N=Cu, Ag, and Au. The values of AR(P), averaged over two or more samples each, increase from about 14 to 15 to 16 fΩm^2 from Cu to Au to Ag, but the data sets overlap within mutual fluctuations of $\pm 1.5 - 2$ fΩm^2. The equivalent averages for $A\Delta R$ increase from about 0.28 to 0.35 to 0.48 fΩm^2 from Cu to Au to Ag, with uncertainties of $\pm 0.03 - 0.05$ fΩm^2 each [69].

N	ρ_N (nΩm)	l_{sf}^N (nm)	$\delta_{N/Cu}$	$2AR_{N/Cu}$ (fΩm^2)
Pd	40 ± 3	25^{+10}_{-5}	$0.24^{+0.06}_{-0.03}$	0.9 ± 0.1
Pt	42 ± 6	14 ± 6	0.9 ± 0.1	1.5 ± 0.1
Au	19 ± 6	35^{+65}_{-5}	$0.13^{+0.08}_{-0.02}$	$0.35^{+0.1}_{-0.05}$

Table 4.2: A table of resistivities and spin-diffusion lengths of Pd, Pt and Au, and the spin-memory-losses at Pd/Cu, Pt/Cu and Au/Cu and the specific resistances of these interfaces at 4.2K.

4.6 Summary

We measured the spin-diffusion lengths of our sputtered Pd, Pt and Au layers as well as the spin-memory-losses at Pd/Cu, Pt/Cu and Au/Cu interfaces at 4.2K using the spin-memory-loss detector [93]. Table 4.2 shows the measured values of resistivities and spin-diffusion lengths of sputtered Pd, Pt and Au, the spin-memory-losses (δ) at Pd/Cu, Pt/Cu and Au/Cu interfaces and interface specific resistances of $2AR_{Pd/Cu}$, $2AR_{Pt/Cu}$ and $2AR_{Au/Cu}$. The spin-diffusion lengths in sputtered Pd and Pt are long enough so that nanometer thick layers of either could be used in magnetic multilayers without excessive spin-flipping (spin-memory-loss) in the layers themselves. The resistivity of sputtered gold, $\rho_{Au} \approx 19 \pm 6$ nΩm, is low enough, the spin-diffusion length in sputtered Au, $l_{sf}^{Au} = 35^{+65}_{-5}$ nm, long enough, and the CPP- $A\Delta R$ of Co/Au EBSVs with $t_{Au} = 10$ nm is large enough, that 10 nm thick Au layers can be used in magnetic multilayers both for studies of basic physics and for devices. Later, Ji et al. measured the spin diffusion length of sputtered Au in lateral spin valves using a completely different technique [107] and found $l_{sf}^{Au} = 63 \pm 15$ nm at 10K, which is in agreement with our result at 4.2K. The interface specific resistance, $2AR_{Au/Cu} = 0.35^{+0.10}_{-0.05}$ fΩm^2, overlaps an earlier value [106].

The interface specific resistances, $AR_{Pd/Cu}$ and $AR_{Pt/Cu}$, are smaller than those

for $AR_{Nb/Cu}$ and $AR_{W/Cu}$. In contrast, the spin-flipping probabilities at Pd/Cu and Pt/Cu interfaces are, respectively, very similar to those at Nb/Cu and W/Cu interfaces. These last similarities are consistent with spin-orbit scattering in interfacial alloys being the source of those probabilities. However, although Au is next to Pt in the same row of periodic table the spin-memory-loss at Au/Cu interface is much smaller than that for Pt/Cu and W/Cu, which may be due to the low resistivity and and the absence of d-electron states at the Au Fermi surface.

4.7 Comparison of measured ARs with theory

We compare the interface specific resistances measured with superconducting leads in the CPP direction with later no-free-parameter calculations with real Fermi surfaces by Xia et al.[97, 98] assuming perfect specular interfaces and 50-50 alloy interfaces. Interestingly, the samples fabricated using sputtering show good agreement with the calculated values of ARs if the lattice mismatch at the interfaces is very small, i.e the difference between the lattice parameters of the metals forming the interface is less than 1 % (see Table 4.3). Even, the calculated ARs for perfect and 50-50 alloy Pd/Cu, Pt/Cu and Au/Cu interfaces are not bad, differing only about 50% to a factor of 2 from our experimentally measured ARs (see Table 4.3).

M1/M2	$2AR$ (exp) (fΩm^2)	$2AR$ (perfect) (fΩm^2)	$2AR$ (50-50) (fΩm^2)	a_0^{M1}/a_0^{M2} (Å)	Δa_0 (%)
Ag/Au	0.1[106]	0.09[98]	0.12[98]	4.09/4.08[1]	0.24
Co(fcc)/Cu	1.0[61]	0.9[98]	1.1[98]	3.56/3.61[1]	1.4
Fe/Cr	1.6[108]	1.5[105],1.9[98]	1.6[98]	2.87/2.88[1]	0.35
Pd/Cu	0.9 ± 0.1	1.5[109]	1.6[109]	3.89/3.61[1]	7.8
Pt/Cu	1.5 ± 0.1			3.92/3.61[1]	8.6
Au/Cu	$0.35^{+0.1}_{-0.05}$	0.45[109]	0.7[109]	4.08/3.61[1]	13

Table 4.3: A comparison between the experimental and theoretical values of ARs at 4.2K. Calculations agree with the experimental values if the lattice parameters of the metals constituting the interface are close.

Chapter 5

Changes in magnetic scattering anisotropy at a ferromagnetic/ superconducting interface

5.0.1 Overview

There is now great interest in both static and transport properties of ferromagnetic/superconducting (F/S) metallic interfaces. Examples of topics of interest include: reductions in the superconducting transition temperature T_c upon injection of a polarized current [110]; propagation of a polarized current through a superconductor [111]; proximity effects between S and F metals [112, 113, 114, 115]; the F/S interface resistance [116]; predictions that the current-perpendicular-to-plane (CPP) magnetoresistance (MR) should be zero when measured with superconducting leads [117]; and subsequent arguments that it won't be if strong spin-flipping is present [118], or if exchange splitting between spin up and spin down electron bands plays an important role [119, 120].

CPP-MR experiments with superconducting Nb leads in contact with F- metals Co, Fe, Ni and the F-based alloys Py and $Co_{0.91}Fe_{0.09}$ (Refs. [61, 121, 122]) showed that F/S interfaces contribute only a constant term to each current channel of the

2CSR model, with interfacial scattering parameter $\gamma_{F/S} = 0$. Moreover, inserting 10 nm of Cu or Ag between the F-metal Co and the S-metal Nb appeared to leave $\gamma_{F/S} \approx 0$ (Refs. [61, 121]) quite different from the values of $\gamma_{Co/Cu} \approx \gamma_{Co/Ag} \approx 0.8$ for Co/Cu and Co/Ag interfaces not in contact with a superconductor [61, 31]. Direct measurements for simple Nb/F/Nb and Nb/N/F/N/Nb sandwiches with different thicknesses of F showed that N = Cu or Ag inserts produced no systematic changes in AR [123].

K. Eid [57] measured the changes in the scattering anisotropy at a Co/Nb interface at 4.2K upon inserting Cu, FeMn and Ru and combinations of these metals in between superconducting Nb and ferromagnetic Co [57]. To detect very small changes in the CPP-MR, he designed a hybrid spin-valve that would work as a null detector i.e. when there is no insert between Co and Nb the MR is zero. The use of the null detector provides a more precise check for the effect of inserts. Eid [57] observed that the scattering asymmetry changed for inserts of the combinations of Ru/Cu, Cu/FeMn but stayed the same for inserts of just Cu and FeMn between Co and Nb. We shall call such changes in the MR of the null detector (or scattering anisotropy) 'magnetic activation' of F/S interfaces. Here, we confirm Eid's results by repeating some of his studies and extending them to additional inserts to understand how the scattering asymmetry is affected. Most of this chapter is published in Ref. [124].

5.0.2 Introduction

We present evidence of a new phenomenon at F/S interfaces at 4.2K, activation of the magnetic scattering anisotropy at Co/Nb interfaces when certain non-magnetic

metals (or combinations) X are inserted between the Co and Nb as part of a carefully designed CPP-MR hybrid spin-valve (SV) [61]. More precisely, as described in detail below, the SV is designed so that when X is absent, the system SV/Nb produces almost zero change in specific resistance, $A\Delta R = AR(\mathrm{AP}) - AR(\mathrm{P})$, between the parallel (P) and anti-parallel (AP) magnetic orderings of the two F-layers in the SV. Here A is the cross-sectional area through which the CPP current flows at 4.2K (see inset in Fig. 5.1). Such a device is, thus, very sensitive to small changes in the magnetotransport properties caused by inserting X. We show that inserting X consisting of some metals or combinations of metals leaves $A\Delta R$ unchanged, which we interpret as leaving the scattering asymmetry at the F/XS interface, $\gamma_{F/XS}$, approximately 0. In contrast, insertion of other metals or combinations changes $A\Delta R$ (i.e., giving non-zero $\gamma_{F/XS}$), and whether $A\Delta R$ becomes more positive or negative is set by the previously known sign of $\gamma_{F/X}$, the anisotropy without S. "Activation" of such changes in $A\Delta R$ seems to require strong spin flipping between F and S.

5.0.3 Experiment and Results

In this study we focus upon $\gamma_{F/XS}$. We justify this focus by showing first that none of the inserts X of interest change AR between Co and Nb, and that all show least a partial proximity effect (i.e., Cooper pairs propagate from S to Co through X). Details of our sample preparation, and measuring techniques are given in Chapter 3. Fig. 5.1 shows AR for 20 nm of Co alone, and with inserts of N = 4 nm of Ru, 6 nm of Au, or 2 nm of FeMn. 20 nm of Co is thin enough so that the data all lie near the extrapolated value for zero Co thickness. The lack of significant increases in AR in

Fig. 5.1 shows at least a partial proximity effect in N, especially for FeMn ($\rho \sim 850$ nΩm)[93] and Ru ($\rho \sim 100$ nΩm)[125], where AR should otherwise have increased by ~ 3.5 and 0.8 fΩm^2, respectively, more than twice the actual deviations from the value for Co(20). FeMn is also unique in the present study, in that a layer only 1 nm thick generates very strong spin-flipping, [93] and that various of our unpublished studies lead us to believe that F/FeMn interfaces are magnetically inactive (i.e., have $\gamma_{F/FeMn} = 0$).

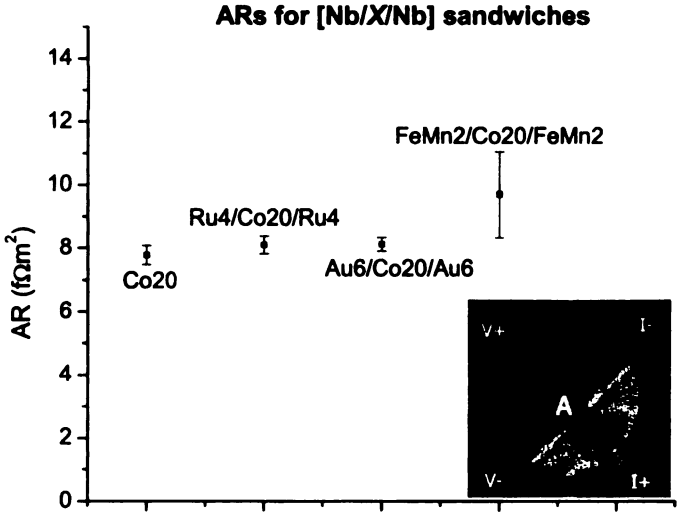

Figure 5.1: ARs for Nb/X/Nb sandwiches with X=Co(20), Ru(4)/Co(20)/Ru(4), Au(6)/Co(20)/Au(6), and FeMn(2)/Co(20)/FeMn(2). Thicknesses are in nanometers. Inset: The circular sample with bottom (V-, I-) and top (V+, I+) crossed Nb strips. Current (I) and voltage (V) connections are indicated. A is the area through which the current flows at 4.2K.

To isolate the behavior of a single Co/X/Nb structure, thus focusing upon $\gamma_{Co/XS}$, we constructed a SV for which $A\Delta R$ is near zero when X is absent. We then examined the effect of inserting X. We achieved the clear AP and P states required for a hybrid SV by choosing F-metals and thicknesses to give very different saturation fields,

Py(24) ($H_s \sim 20$ Oe) and Co(2) ($H_s \sim 300$ Oe). Here, and hereafter, all thicknesses are in nm. Our SV has the form Nb/Cu(1)/Py(24)/Cu(20)/Ru(2)/Co(2)/X/Nb. Significant spin-flipping in the Py layer [122] and at Cu/Ru [125] and Co/Cu [68] interfaces means that the specific resistances of such a spin-valve cannot be described using a simple two-current series-resistor (2CSR) model. However, a modified 2CSR model so greatly simplifies the explanation of our experiment, that we use it, subject to the caveat that our explanation is only schematic, strengthened by our belief that the model does not distort the essential features of the argument. If we assume that the Co/Nb interface is magnetically inactive (i.e. that it has $\gamma_{Co/Nb} = 0$), then for no X, the 2CSR model taking account of strong spin-flipping only within the Py would give [61, 23, 12][Chapter 2]:

$$A\Delta R \propto (\beta_{Py}\rho^*_{Py}l^{Py}_{sf} + \gamma_{Py/Cu}AR^*_{Py/Cu})(\beta_{Co}\rho^*_{Co}t_{Co} + \gamma_{Co/Ru}AR^*_{Co/Ru}), \qquad (5.1)$$

where β_F is the bulk scattering anisotropy in metal F, $\rho^*_F = (\rho^{\uparrow}_F + \rho^{\downarrow}_F)/4$, and l^{Py}_{sf} is the spin-diffusion length in Py [61, 122]. The essential features of Eqn. 5.1 are: (1) that the contributions from the Py and the Co appear separately as a product; and (2) because $\gamma_{Co/Ru}$ is negative [125], the two terms in the second parentheses have opposite signs. Choosing $t_{Co} = 2$ nm should bring the sum of those two terms close to zero [61, 125]. Fig. 5.2 shows that the resulting $A\Delta R \sim -0.05$ fΩm^2 with no X is indeed much smaller than the value $A\Delta R \sim +0.4$ fΩm^2 that we find [57] when there is no Ru to the left of the Co(2) layer in the SV and also no X.

If, now, we insert into Eqn. 5.1 a layer X as listed above, and if the Co/X interface is magnetically active, ($\gamma_{Co/XS} \neq 0$), then this interface contributes an additional term

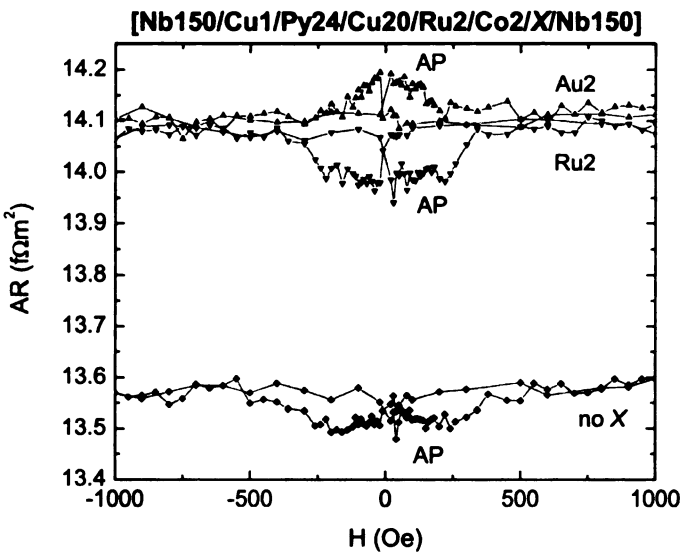

Figure 5.2: AR vs. H for Nb150/Cu1/Py24/Cu20/Ru2/Co2/X/Nb150 with no X, X=Ru(2) and X=Au(2). The AP states are labeled for each case.

to Eqn. 5.1, giving

$$A\Delta R \propto (\beta_{Py}\rho^*_{Py}l^{Py}_{sf} + \gamma_{Py/Cu}AR^*_{Py/Cu})(\beta_{Co}\rho^*_{Co}t_{Co} + \gamma_{Co/Ru}AR^*_{Co/Ru} + \gamma_{Co/XS}AR^*_{Co/X}). \tag{5.2}$$

To focus upon $\gamma_{Co/XS}$, we have assumed that $AR^*_{Co/XS} = AR^*_{Co/X} \approx 0.5$ fΩm^2, the already measured and very similar values of $AR^*_{Co/X}$ for X=Cu, Ag, Ru, and Au. If this additional term is positive ($\gamma_{Co/XS} > 0$), $A\Delta R$ should become more positive and if it is negative ($\gamma_{Co/XS} < 0$), $A\Delta R$ should become more negative. Fig. 5.2 shows how $A\Delta R$ became more negative upon insertion of $X = 2$ nm of Ru, but larger and positive upon insertion of $X = 2$ nm of Au.

In Fig. 5.3 we collect together $A\Delta R$ data for a series of different metals and combinations of metals. The uncertainty bars for each X were obtained by summing the

squares of the individual uncertainties in $A\Delta R$, taking the square root, and dividing by the number of samples measured. The values of $A\Delta R$ and the number of samples used in the statistics are given in Table 5.1. To within measuring uncertainties, X = Cu, Ag, FeMn, Ag/Cu, and Cu/Ag, all leave $A\Delta R$ unchanged. In contrast, X = Ru, Ru/Cu, and Ru/FeMn all make $A\Delta R$ more negative, and X = Au, Cu/Ru, Cu/FeMn, Cu/Au, and Ag/Ru all invert the sign of $A\Delta R$, making $A\Delta R$ positive. To within experimental uncertainties, the positive values for Au, Cu/Ru, Cu/Au, and Ag/Ru, are all the same (with that for Cu/FeMn somewhat larger). These similar values without FeMn are consistent with similar values of $\gamma_{Co/X}$ for X=Cu [61], Ag [23], and Au. While, strictly, we have not measured $\gamma_{Co/Au}$ and $AR^{*}_{Co/Au}$ separately, the similarity of our (mostly unpublished) CPP-MR data for Co or Py with Au to those for Co or Py with Cu and Ag strongly suggests that the interfacial parameters for Au are similar to those for Cu and Ag. It is of key importance to note that $A\Delta R$ becomes more negative whenever Ru is next to the Co, and more positive when Cu or Ag is next to the Co but separated from the Nb by Ru, Au, or FeMn. These behaviors show that the change in $A\Delta R$ is due to a change in the Co/X interface, since $\gamma_{Co/Ru} < 0$, but $\gamma_{Co/Cu} \approx \gamma_{Co/Ag} > 0$. We consider next why some X leave $A\Delta R$ unchanged (i.e., leave $\gamma_{Co/XS} = 0$ in the presence of superconducting Nb), while others change it (i.e., give $|\gamma_{Co/XS}| > 0$).

5.0.4 Discussion

As noted in the introduction, Taddei et al. argued [118] that the presence of strong spin-flipping is necessary for the appearance of a full CPP-MR. While there are ques-

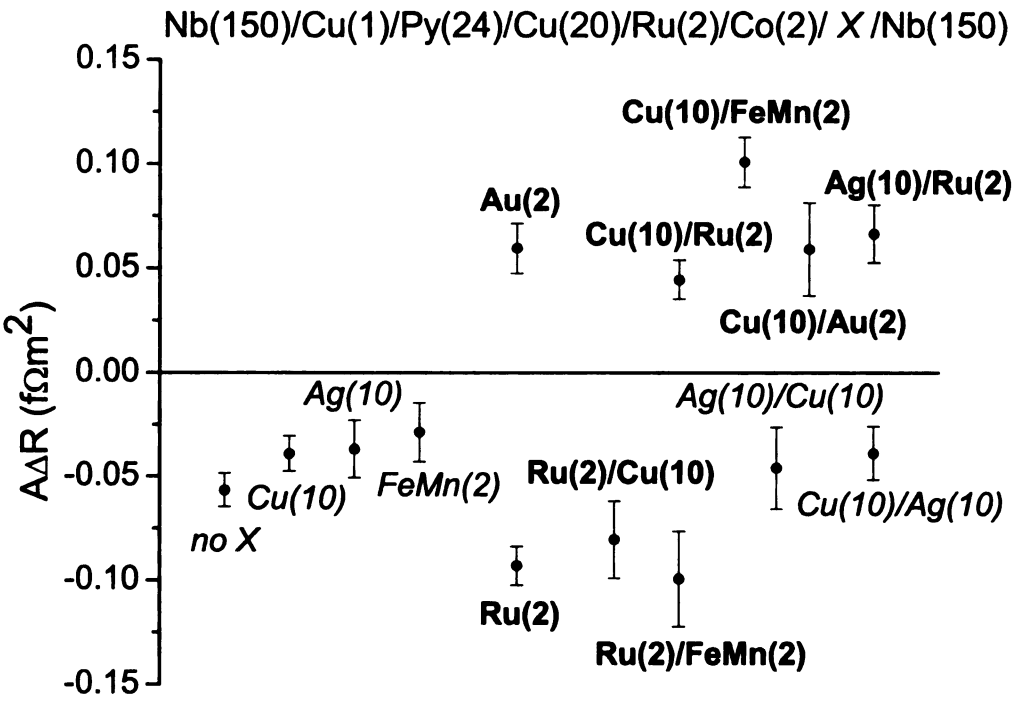

Figure 5.3: $A\Delta R$ for samples of the form Nb(150)/Cu(1)/Py(24)/Cu(20)/Ru(2)/ Co(2)/X/Nb(150) for a variety of X, including no X. Samples with italic labels leave $\gamma_{Co/XS} = 0$, whereas samples with bold labels give $|\gamma_{Co/XS}| > 0$.

tions about the applicability of their argument, no other simple potential explanation for the different behaviors shown in Figs. 5.2 and 5.3 presents itself to us. We, thus, ask whether the data in Figs. 5.2 and 5.3 can be understood in terms of different amounts of spin-flipping between the Co and Nb for different X, with weak spin-flipping leaving X inactive (i.e., $\gamma_{Co/XS} = 0$) but strong spin-flipping making it active ($\gamma_{Co/XS} > 0$).

All of the metallic layers N except FeMn are much thinner than their respective bulk spin-diffusion lengths. Thus, spin-flipping within those metals cannot be the source of the differences in their activities. The only potential source is spin-flipping

X [# of samples]	$A\Delta R$ (fΩm^2)
no X [6]	-0.057 ± 0.008
Cu(10)[7]	-0.039 ± 0.008
Ag(10) [2]	-0.037 ± 0.014
FeMn(2) [2]	-0.029 ± 0.014
Au(2) [2]	0.060 ± 0.012
Ru(2) [3]	-0.093 ± 0.009
Ru(2)/Cu(10) [1]	-0.080 ± 0.019
Cu(10)/Ru(2) [4]	0.044 ± 0.009
Ru(2)/FeMn(2) [1]	-0.099 ± 0.023
Cu(10)/FeMn(2) [3]	0.101 ± 0.012
Cu(10)/Au(2) [1]	0.059 ± 0.022
Ag(10)/Cu(10) [2]	-0.046 ± 0.020
Ag(10)/Ru(2) [2]	0.066 ± 0.014
Cu(10)/Ag(10) [2]	-0.039 ± 0.013

Table 5.1: $A\Delta R$s and the number of samples used to determine the error bars for inserts X in Fig. 5.3

at the N/S interface. Unfortunately, we do not have a way to measure spin-memory loss at the interfaces of these metals with superconducting Nb. We can, however, measure such loss at interfaces with non-superconducting Nb [93]. Since Co/Au and Co/Ru have their interface magnetic anisotropies activated when the Au or Ru are in contact with superconducting Nb, whereas Co/Cu does not, we examined spin-memory loss at the interfaces of these three metals with non-superconducting Nb, using the method described in Ref. [93]. In that method, a multilayer of the form $[\mathrm{N(3nm)/Nb(3nm)}]_N$, where N is the number of bilayers, is inserted into the middle of a Py-based spin-valve, in which one Py-layer is exchange-bias pinned and the other is left free to reverse in a small magnetic field. Insertion of the multilayer should then cause $A\Delta R$ to decrease exponentially with N as

$$A\Delta R \propto \exp(-2N\delta_{\mathrm{N/Nb}}), \tag{5.3}$$

where $\delta_{\mathrm{N/Nb}}$ characterizes the probability of spin-flipping at the N/Nb interface. Fig.

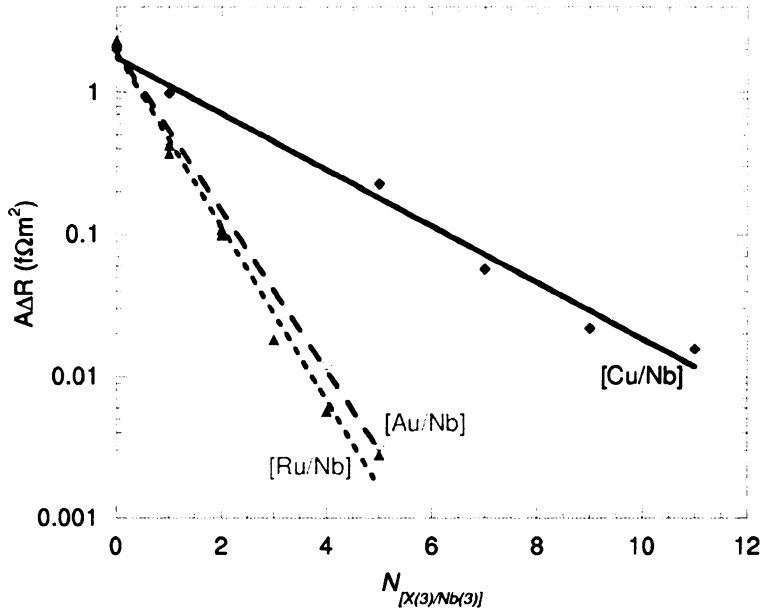

Figure 5.4: $A\Delta R$ vs. N for inserts X=[Ru(3)/Nb(3)]$_N$, X=[Au(3)/Nb(3)]$_N$ and X=[Cu(3)/Nb(3)]$_N$ in exchange-biased spin valves of the form Nb(150)/Cu(10)/FeMn(8)/Py(24)/Cu(10)/X/Cu(10)/Py(24)/Cu(10)/Nb(150).

5.4 shows a plot of $\log(A\Delta R)$ vs. N for N = Cu, Au, or Ru. The Au/Nb and Ru/Nb data decrease much more rapidly with increasing N than do the data for Cu/Nb, showing that spin-flipping is several times stronger at Au/Nb and Ru/Nb interfaces than at Cu/Nb interfaces, when the Nb is normal. Since increasing N also increases the amount of N = Cu, Au, or Ru, as well as of Nb, in the spin-valve, the data of Fig. 5.4 must be corrected for spin-flipping within the "bulk" of these layers to correctly obtain $\delta_{\mathrm{N/Nb}}$. These corrections are, however, modest in size and similar for Cu, Au, and Ru. Thus, they do not affect the relative sizes of $\delta_{\mathrm{N/Nb}}$ inferred directly from Fig. 5.4. Assuming that spin-flipping at Au/Nb and Ru/Nb interfaces is also stronger than at Cu/Nb when the Nb is superconducting, we have a rationale for activation of the Co/Au and Co/Ru interfaces by spin-flipping at the Au/Nb and Ru/Nb interfaces.

Turning, lastly, to FeMn, if $\gamma_{Co/FeMn} = 0$ as noted above, then strong spin-flipping

in the FeMn can only activate Co/X if X = N/FeMn, where FeMn is inserted between N and the superconducting Nb. Indeed, we see in Fig. 5.3 that the Co/FeMn interface is not activated, but the Co/Cu/FeMn interface is.

5.0.5 Summary

We constructed a multilayer that let us measure anisotropy in spin-dependent scattering at a single F/XS interface, when the non-ferromagnetic metal (or combination) X is sandwiched between the ferromagnetic metal F and superconducting (S) Nb. We assume that the proximity effect allows Cooper pairs to pass through X, so that we are still studying an effectively F/S interface. Our results confirm earlier conclusions [61] that such an F/X interface is magnetically inactive (insertion of X produces little or no change in $A\Delta R$) when X=Cu, Ag, or FeMn alone, or combinations involving only Ag and Cu. In contrast, when X=Ru or Au, or combinations involving either of these two metals or FeMn that itself is not in contact with the Co, the F/XS interface becomes magnetically active, producing significant changes in $A\Delta R$ including, in some cases, changes in sign. For X=Cu, Au, and Ru, we showed that these different magnetic activities correlate with the strength of spin-flipping at the interfaces of X with non-superconducting Nb. Qualitatively these results are consistent with the arguments of Taddei et al. [117, 118] that spin-flipping can affect the CPP-MR when the sample has superconducting leads. To determine if this argument provides the correct explanation for our data, further theoretical analysis is needed.

Chapter 6

Controlled normal and inverse CIMS and MR in magnetic nanopillars

6.1 Introduction

Although CIMS is expected to result from spin polarization of the current, it has yet to be shown that CIMS can be manipulated (e.g., inverted) by changing that polarization. Prior studies of CIMS in F1/N/F2 nanopillars, where F1 is a thick (fixed) ferromagnet, N is a normal metal and F2 is a thin (free) ferromagnet which is free to switch with a high-density spin polarized dc current, involved only positive scattering anisotropies in both F-metals and at F/N interfaces, i.e. minority electrons are scattered more strongly in F1, F2 and at F1/N and N/F2 interfaces. The current is then positively spin polarized in the F layers, i.e., carried mainly by majority electrons. In such "standard" conditions, electrons flowing from F1 to F2 (negative charge current, $I < 0$) switch the moment $\mathbf{M_2}$ of F2 from antiparallel (AP) to $\mathbf{M_1}$ (high resistance R) to parallel (P) to $\mathbf{M_1}$ (low R). Conversely, positive I (> 0) switches F2 from P to AP. We call these behaviors "normal" CIMS and normal current-perpendicular-to-plane (CPP) magnetoresistance (MR). We present CIMS experiments exploiting the possi-

bility of inverting the spin anisotropy by doping F1 or F2 with an impurity (Cr) that scatters majority spin electrons more strongly [61, 126, 127, 108, 128, 129, 105, 97]. We thus show, for the first time, that inversion of the spin anisotropy can invert the CIMS direction, i.e., invert the signs of I for AP to P and P to AP transitions. We also find inversions of the MR (larger R for the P state) with appropriately doped samples, as expected from prior CPP-MR results at low temperature [61, 126]. Measurements at 295 and 4.2 K show that the qualitative behaviors of both CIMS and MR are independent of temperature over this range for our samples.

Analysis of the switching behaviors lets us discriminate between models of CIMS. We divide the standard models of spin-transfer torque (STT) used to describe CIMS into two classes, ballistic [33, 34, 130] and diffusive [86, 35, 73, 131, 132, 74]. Both predict that changing scattering anisotropies can invert the MR and/or CIMS. However, their expectations need not agree. In ballistic transport, the spin anisotropy comes only from reflections at the F/N interfaces. Inverting CIMS is predicted to require negative anisotropy at F1/N [130]. Inverting the MR should require opposite scattering anisotropies at F1/N and N/F2 [61]. In diffusive transport, the spin anisotropy of scattering within the F layers is also important, so that one must consider the net anisotropy of each F layer (i.e., the resultant effect of the bulk of F and its F/N interface). An additional effect, spin accumulation, can either support or compete with the effect of polarized current [86, 35, 73, 131, 132, 74]. In this Chapter, in addition to determining the relation between spin anisotropies and CIMS direction, we answer four questions relevant to understanding CIMS.

1. Is the CIMS direction set only by interface scattering anisotropy? No.

2. Can impurity scattering within the layers be important? Yes.

3. Do the anisotropies of F1 and F2 play different roles for the CIMS direction of F2? Yes.

4. Can spin accumulation be important? Yes.

Most of this Chapter is published in Ref. [89].

6.2 Experiment and Results

Sample preparation and measurement techniques are described in detail in Chapter 3. Here, we briefly note that our F1/N/F2 nanopillars have approximately 130 × 70 nm lateral dimensions, are ion-milled only partly through N to minimize dipolar magnetic coupling between F1 and F2, and I^+ represents electron flow from F2 to F1.

To determine how changing spin anisotropies changes CIMS directions, we combine in different ways three pairs of materials: Py/Cu (Py= $Ni_{84}Fe_{16}$), with both bulk and interface anisotropies positive [61]; Fe(Cr)/Cr [Fe(Cr)=$Fe_{95}Cr_5$], with both negative [126, 127, 108, 129, 105, 97]; and Ni(Cr)/Cu [Ni(Cr)=$Ni_{95}Cr_5$], with thick enough Ni(Cr) so its negative anisotropy dominates the positive anisotropy of the Ni(Cr)/Cu interface [133]. The net anisotropy is found using the MR. Here, we present the general results of the study but the details of samples with Fe(Cr) will be given in the thesis of Al-Haj Darwish.

Py and Py-Cu interfaces both have positive scattering anisotropy [61]. In accord with prior data [48], Fig. 6.1 shows that Py(24)/Cu(10)/Py(6) nanopillars (layer

thicknesses in nm) give normal MR and normal CIMS. At both 295 and 4.2K, the MR transitions from P to AP occur after H passes through zero, consistent with little or no magnetic coupling. The agreement between minimum and maximum values of dV/dI for the MR and CIMS curves shows that the switching is complete. Figures 6.2 and 6.3 also show weak coupling and complete switching. In contrast to Py, Ni(Cr) has negative scattering anisotropy but Py/Cu and Ni(Cr)/Cu interfaces both have positive scattering anisotropies. Ni(Cr)/Cu systems are special in the sense that they have opposite bulk and interface anisotropies that allows us to investigate the ballistic and diffusive models of transport for CIMS. Figure 6.2 shows the case, Ni(Cr)(20)/Cu(20)/Py(10). Combining net negative anisotropy for Ni(Cr) with net positive anisotropy for Py gives the expected inverse MR, and now inverse CIMS. Figure 6.3 shows a way to achieve inverse MR with normal CIMS, using Py(24)/Cu(10)/Ni(Cr)(4). For each sample, the switching directions of MR and CIMS are the same at 295K and 4.2K. Each switching behavior was independently reproduced, and no inconsistent switching was seen.

As expected for the MR [61, 126], when the net scattering anisotropies for F1 and F2 are the same (Fig. 6.1), the MR is normal, and when they are opposite (Figs. 6.3 and 6.2), the MR is inverse. New for CIMS, when the net scattering anisotropy for F1 is positive, CIMS is normal (Figs. 6.1 and 6.3), and when it is negative (Fig. 6.2), CIMS is inverse. For these samples, the direction of CIMS is set by the net scattering anisotropy of F1 and is independent of that of F2. Table 9.2 lists the signs for F1, F2 bulk, F1/N, N/F2 interfaces, and F1(net), F2(net), as well as for the observed MR and CIMS. The MR and CIMS figures of samples involving Fe(Cr) are given in Ref.

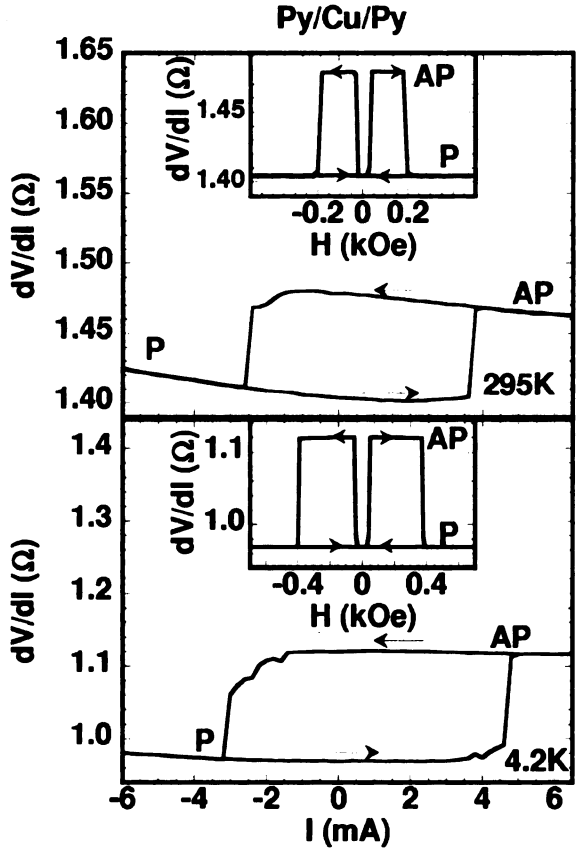

Figure 6.1: Py(24)/Cu(10)/Py(6) data at 295K (top) and 4.2K (bottom) showing normal MR (dV/dI vs. H at $I = 0$) in the insets and normal CIMS for dV/dI vs. I in the main figures at $H = 0$ Oe for 295K and at $H = 20$ Oe for 4.2K. In all figures, $I > 0$ represents electron flow from F2 to F1.

[89].

F1/N/F2	F1	F1/N	F1(net)	F2	N/F2	F2(net)	MR	CIMS
Py/Cu/Py	+	+	+	+	+	+	+	+
Ni(Cr)/Cu/Py	-	+	-	+	+	+	-	-
Py/Cu/Ni(Cr)	+	+	+	-	+	-	-	+
Fe(Cr)/Cr/Fe(Cr)	-	-	-	-	-	-	+	-
Py/Cu/Cr/Fe(Cr)	+	+	+	-	-	-	-	+

Table 6.1: Scattering anisotropies (+=positive, -=negative) of F1, F1/N, and their net anisotropy F1(net), those of F2, N/F2, and their net anisotropy F2(net), and the observed MR and CIMS (+=normal, -=inverse).

Comparing the results of Py/Cu/Cr/Fe(Cr) and Py/Cu/Ni(Cr), which both have inverse MR and normal CIMS, and Fe(Cr)/Cr/Fe(Cr) with normal MR and inverse

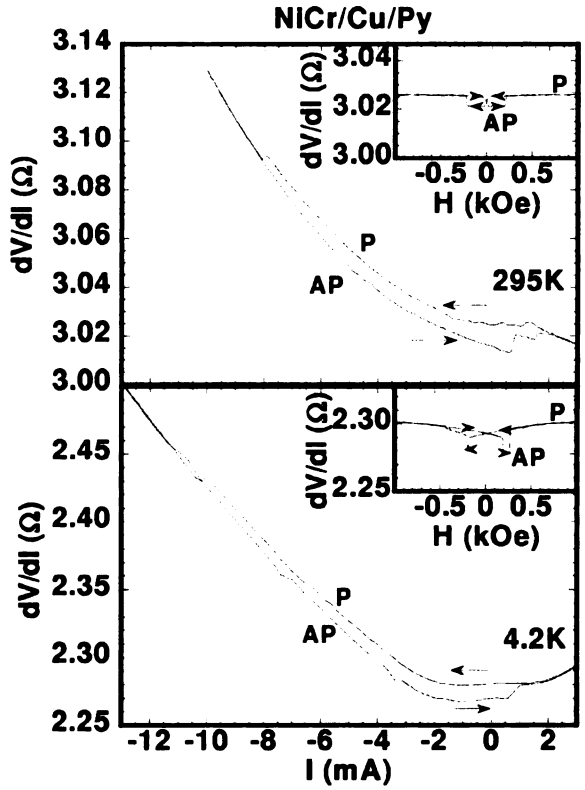

Figure 6.2: Ni(Cr)(20)/Cu(20)/Py(10) data at 295K (top) and 4.2K (bottom) showing inverse MR (dV/dI vs. H at $I = 0$) in the insets and inverse CIMS for dV/dI vs. I at $H = 0$ in the main figures.

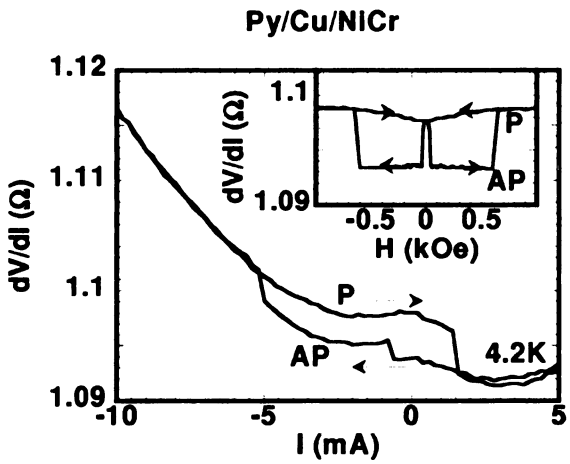

Figure 6.3: Py(24)/Cu(10)/Ni(Cr)(4) data at 4.2K showing inverse MR (dV/dI vs. H at $I = 0$) in the inset and normal CIMS for dV/dI vs. I at $H = 0$ in the main figure.

CIMS and Ni(Cr)/Cu/Py with inverse MR and inverse CIMS given in table 9.2, shows that, when bulk scattering predominates, the CIMS direction is independent of the scattering anisotropy of F1/N and N/F2. Finally, dominance of the bulk contribution of scattering anisotropy in either F1 [e.g., Ni(Cr) in Fig. 6.2] or F2 [Ni(Cr) in Fig. 6.3] is inconsistent with ballistic transport through the nanopillar, where the interfaces must dominate the scattering. While ballistic STT models cannot describe our data involving Ni(Cr), the CIMS directions in all cases studied accord with the ballistic prediction of [130] if the scattering anisotropy at the F1/N interface is simply replaced by the net anisotropy for F1. For diffusive transport, the current polarization in N depends upon the net scattering anisotropies of both F1 and F2, and CIMS depends upon both the spin-polarized charge current and spin-accumulation effects [86, 35, 73, 131, 74]. Equation (1) reproduces Eq. 5 of Ref. [74] for the torque Γ^P at a small angle from the P state (for Γ^{AP}, replace P by AP). Our notations for F1 and F2 are reversed from [74].

$$\frac{\Gamma^P}{\hbar} = \left[\left\{\frac{v_F m_N^P}{8} + \frac{j_{m,N}^P}{2}\right\}(1 - e^{-t_N/\lambda_N}) + \left\{\frac{v_F m_{F1}^P}{4} + j_{m,F1}^P\right\} e^{-t_N/\lambda_N}\right] \times \hat{\mathbf{M}}_2 \times (\hat{\mathbf{M}}_2 \times \hat{\mathbf{M}}_1) \quad (6.1)$$

Equation 6.1 comes from an extension of the Valet-Fert [12] model of CPP-MR to noncollinear states. v_F is the Fermi velocity in N, m_N^P and $j_{m,N}^P$ are the spin accumulation density [73, 131, 132, 74, 12] and spin-current density in N just outside the F2-N interface calculated for the P state, m_{F1}^P and $j_{m,F1}^P$ are the same quantities in F1 just inside the F1-N interface, t_N and λ_N are the thickness and mean-free path of N, and $\hat{\mathbf{M}}$ is a unit vector in the direction of $\mathbf{M}$. The second set of {} braces

dominates the usual case when $t_N \ll \lambda_N$ and the first dominates if $t_N \gg \lambda_N$. The signs of spin current and spin accumulation can support each other or compete.

Using the best parameters from CPP-MR experiments [61, 133], we calculate spin currents and spin accumulations [61, 12], and insert them into Γ^P or Γ^{AP}. Except for Fig. 6.2, the signs of spin current and accumulation always agree and are as expected from the sign of the net spin anisotropy of F1 seen by MR. The case for Fig. 6.2 is more complex. For P to AP, the spin accumulation dominates Γ^P and gives the observed inverse CIMS at $I < 0$; due to the particular parameters of Ni(Cr) and Py, the spin current alone would predict normal CIMS. For AP to P, the spin current dominates Γ^{AP} and gives the observed inverse CIMS at $I > 0$. Thus, we reproduce the behaviors in Fig. 6.2.

6.3 Summary

We have shown that judiciously chosen pairs of ferromagnetic metals or alloys can produce all four combinations of normal and inverse MR and current-induced magnetization switching at both 4.2 and 295 K. The MR is normal if the net scattering anisotropies of F1 and F2 have the same sign, and inverse if they do not. For the samples studied, the CIMS direction is set solely by the net anisotropy for F1, although in Fig. 6.2 this result requires dominance of spin accumulation for the P to AP transition. This latter result, as well as the inverted MRs in Figs. 6.2 and 6.3, show that the interpretation of MR and CIMS must generally take account not only of the interface scattering assumed in ballistic models but also the scattering (and diffusion) within the F layers. As the widely accepted mechanism of CIMS is a quasi-interfacial

absorption of the transverse component of the spin current [33, 130, 73, 131, 74], the importance of scattering within the F layers might seem surprising. However, in a noncollinear magnetic configuration, the transverse spin current in the frame of F2 is related to the longitudinal one in F1, and a global treatment [73, 131, 74] of the longitudinal and transverse components of the spin current and spin accumulation requires the diffusive aspects of the CPP-MR theory [61, 12].

Chapter 7

CIMS in permalloy-based nanopillars with Cu, Ag, and Au spacers

7.1 Introduction

Most experimental studies of current-induced magnetization switching (CIMS) in ferromagnetic/nonmagnetic/ferromagnetic F/N/F trilayer metal nanopillars have used N=Cu as the spacer layer [46, 134, 76, 135, 136, 137, 41, 48]. None has yet used N=Ag or Au. Ag has the potential advantage for devices of sometimes giving a larger Current-Perpendicular-to-Plane (CPP) magnetoresistance (MR) with Permalloy [Py=$Ni_{.84}Fe_{.16}$] [138]. Au has the advantage of being insensitive to atmospheric contamination. We, thus, decided to compare MR and CIMS data at 295K and 4.2K for Py-based nanopillars with N=Cu, Ag, and Au. Most of this chapter is published in Ref. [139].

7.2 Experiment and Results

We fabricated magnetically uncoupled Py-based nanopillars with a standard structure of Cu(80)/Py(24)/N(10)/Py(6)/Au(115), where thicknesses are in nm, N=Cu, Ag,

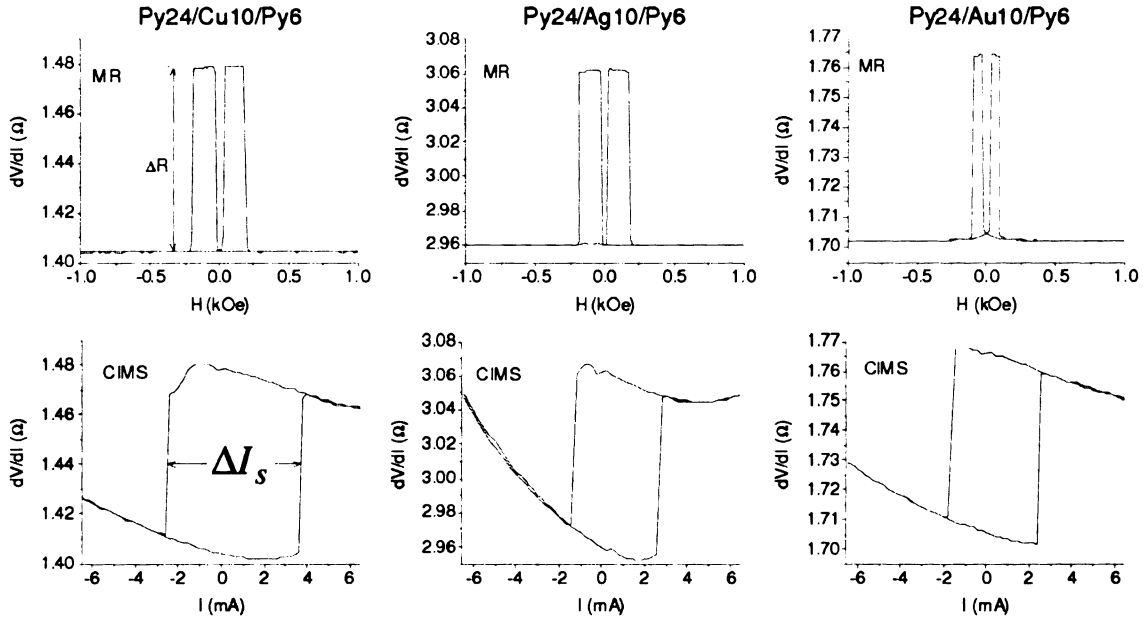

Figure 7.1: MR (top) and CIMS (bottom) at 295K for Py/N/Py nanopillars with N=Cu (left), Ag (middle) and Au (right). Layer thicknesses are in nm.

or Au is the spacer layer, the thick Cu layer is the bottom contact, and the thick Au layer is the top contact. I^+ represents electron flow from Py(6) to Py(24). The approximate sputter deposition rates for the metals and alloys are given in Table 8.1. The details of the sample fabrication and measurement are given in Chapter 3.

Target	Py	Cu	Ag	Au
Deposition rate (Å/s)	5	10	8	5

Table 7.1: Approximate sputter deposition rates of Py, Cu, Ag and Au.

At 4.2K, 10 nm is much less than our best estimates of the spin-diffusion lengths in Cu ($0.5^{+0.5}_{-0.25}\mu$m) and Ag ($0.4 \pm 0.2\mu$m) [69] and three times less than our minimum estimate [100] for Au (35^{+65}_{-5} nm). The room temperature spin-diffusion lengths are probably factors of $2-3$ smaller, [140, 141] still much longer than 10 nm for Cu and Ag, but no longer so for Au. Thus, 10 nm thick Au as an interlayer is expected to give smaller MR than Ag and Cu.

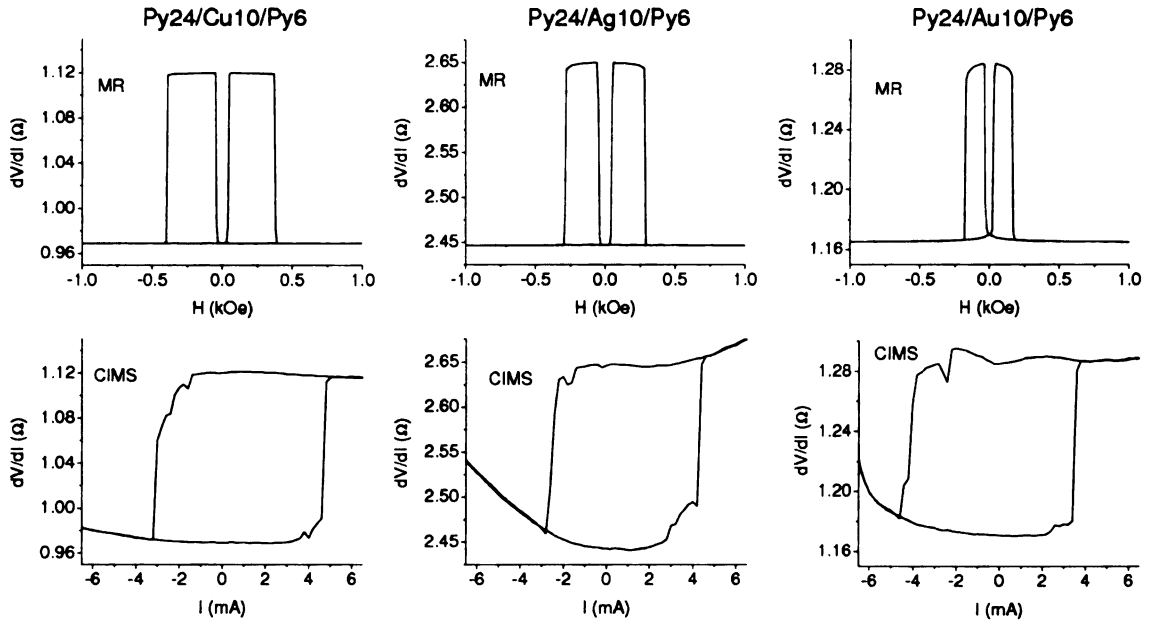

Figure 7.2: MR (top) and CIMS (bottom) plots at 4.2K for the samples in Fig. 7.1. Layer thicknesses are in nm.

N-# of samples	$R(P)$ (Ω)	$\Delta R(\Omega)$	MR (%)	ΔI_s (mA)	H_s (kOe)
295 K					
Cu-5	1.38 ± 0.02	0.070 ± 0.002	5.1 ± 0.3	5.7 ± 0.3	0.18 ± 0.02
Ag-3	2.75 ± 0.14	0.096 ± 0.004	3.5 ± 0.2	3.1 ± 0.4	0.13 ± 0.03
Au-13	1.78 ± 0.05	0.061 ± 0.003	3.4 ± 0.1	5.6 ± 0.4	0.14 ± 0.02
4.2 K					
Cu-2	0.94 ± 0.02	0.144 ± 0.006	15.3 ± 0.3	7.6 ± 0.2	0.32 ± 0.05
Ag-3	2.26 ± 0.12	0.192 ± 0.005	8.5 ± 0.4	6.9 ± 0.2	0.20 ± 0.05
Au-3	1.31 ± 0.07	0.123 ± 0.007	9.4 ± 0.06	6.8 ± 1	0.18 ± 0.02

Table 7.2: Average values of R, ΔR, MR(%), ΔI_s and H_s at 295K and at 4.2K of Py/N/Py with N=Cu, Ag and Au.

Fig. 7.1 compares representative MR and CIMS switching data at 295K for samples of Py(24)/N(10)/Py(6) nanopillars with N=Cu, Ag, and Au. Fig. 7.2 compares the same quantities for the same samples at 4.2K. Table 9.2 compares average values of the total resistance, $R(P)$, when the magnetic moments of the two layers are oriented parallel (P) to each other, the change in resistance upon switching, $\Delta R = R(AP) - R(P)$ between the antiparallel (AP) and P magnetic states, the

magnetoresistance, MR(%)= $(\Delta R/R) \times 100\%$, the difference $\Delta I_s = I_s^+ - I_s^-$ between positive (+) and negative (-) switching currents, I_s, and the upper magnetic switching field, H_s, over $3-13$ samples of each type at 295K (top three data sets) and over $2-3$ samples of each type at 4.2K (bottom three data sets). As a measure of the scatter in our values, we list also the standard deviation of the mean for each quantity.

The average resistances of the three sets of samples differ, due to an unknown mix of variation in areas (smaller area increases R, does not change MR, and decreases ΔI_s) and contact resistances (larger contact resistance increases R, decreases MR, and may leave I_s unchanged). Thus, a precise comparison between them cannot be made. However, at both temperatures, the MRs and ΔI_s are roughly similar for all three metals. The average total resistances of the samples in P states given in Table 9.2 include the sheet resistances of the bottom Cu lead and top Au lead, which are the same for all samples. The resistances of the samples with N=Ag(10) interlayer are almost twice as much as the resistances of the other samples with Au and Cu interlayers. Since we fabricate all the nanopillars in the same way, a factor of 2 in the total resistance of a nanopillar suggests that the main reason for these high resistances is due to bad contacts, because it is very unlikely to have sample areas twice as small. The MRs for the samples with N=Ag(10) give larger ΔR, which is in good agreement with the CPP-MR experiments [138] but smaller MR(%), which is not expected. This also makes us believe that the high resistances of our samples with N=Ag(10) are due to large contact resistances. Although the samples with Au give smaller ΔR and MR, they show switching currents similar to the ones with Ag and Cu. The switching currents of nanopillars with N=Au(10) are interestingly similar

to the ones with the ones with N=Cu(10) even though the MRs of nanopillars with N=Au(10) are smaller. We conclude that Ag and Au represent potentially viable alternatives to Cu for studies of CIMS physics and for CIMS-based devices.

Chapter 8

Reduction of spin polarization and spin transfer by synthetic antiferromagnets

8.1 Introduction

Much CIMS research has been done to try to reduce the switching currents of nanopillars so that they could be used in next generation MRAMs. However, there are possible applications of nanopillars which require higher switching currents like read heads of hard drives. To use nanopillars in read heads the switching currents must be so large so that the magnetization of a nanomagnet flips only due to the external magnetic fields of the magnetic bits on a hard disk. In this Chapter we present a method to increase the switching current by using a synthetic antiferromagnet (SAF) i.e. antiferromagnetically coupled layers as a polarizing layer. Since a similar study was also done by Emley et al. around the same time and already published (see Ref. [142]), we did not publish our results.

8.2 Experiment and Results

When two ferromagnetic layers are separated by a thin enough nonmagnetic layer, the RKKY exchange interaction between the two F-layers couples them ferromagnetically or antiferromagnetically depending on the thickness of the separating N-layer. It is known that 0.6 nm thick Ru between two Co layers gives antiferromagnetic coupling [13]. To study the effect of a synthetic antiferromagnet (SAF) as a polarizing (fixed) layer, we fabricated two magnetically uncoupled nanopillars with the structures: (a) Cu(80)/Co(20)/Ru(0.6)/Co(4)/Cu(10)/Co(4)/Cu(5)/Au(110) (see Fig. 8.1), where Co(20)/Ru(0.6)/Co(4) is an SAF; (b) Cu(80)/Co(20)/Cu(10)/Co(4)/Cu(5)/ Au(110) and compare the MRs and the switching currents of these devices at room temperature. The approximate sputter deposition rates of the constituents of our samples are given in Table 8.1. Further details of sample fabrication and measurement are given in Chapter 3.

Target	Au	Co	Cu	Ru
Deposition rates (Å/s)	6.7	4	10	0.5

Table 8.1: The approximate sputter deposition rates for Au, Co, Cu and Ru.

Fig. 8.2 shows the MR curve for a sample shown in Fig. 8.1. The highest resistance state is the AP alignment of the two Co(4) layers. The P alignment of the two Co(4) layers gives a pseudo P state which is in between the AP state and the total P state of all Co layers, which is not shown in Fig. 8.2 because the strong antiferromagnetic coupling between Co(20) and Co(4) layers require fields higher than 3 kOe to align. The average MR (P and AP alignments between Co(4) layers) for 5 samples with an SAF polarizing layer is 2.23 % and the average MR for 4 samples with a Co(20)

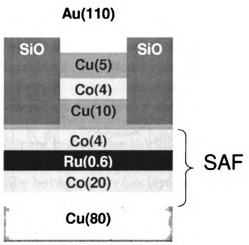

Figure 8.1: A cross-sectional cartoon of the structure of a magnetically uncoupled nanopillar with a synthetic antiferromagnet (SAF). All thicknesses are in nm.

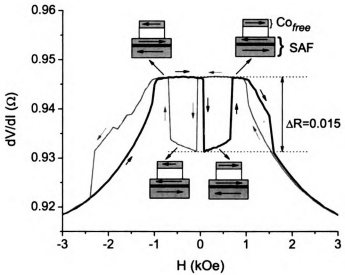

Figure 8.2: MR curve for a Co(20)/Ru(0.6)/Co(4)/Cu(10)/Co(4) nanopillar at zero current at room temperature. The highest resistance antiparallel state represents antiparallel alignments of two Co(4) layers. The parallel alignments of Co(4) layers represent a pseudo parallel state, which gives a higher resistance than the complete parallel alignments of all Co layers.

polarizing layer is 5.4%, which shows that an SAF reduces the spin polarization and therefore MR.

Fig. 8.3 shows CIMS from AP to P state but does not show the P to AP state

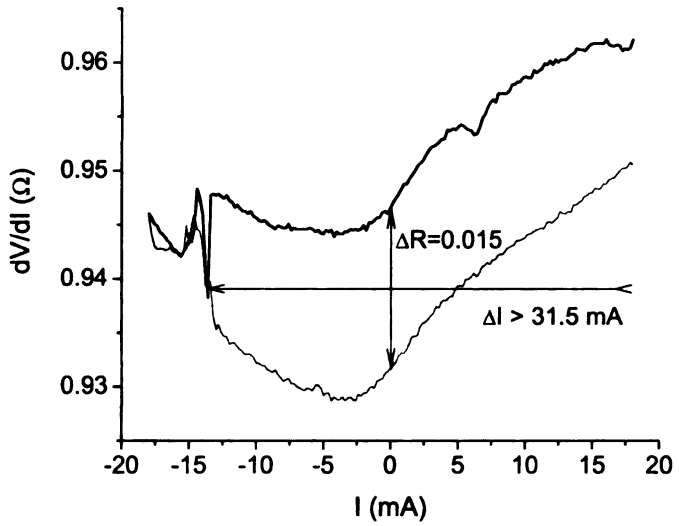

Figure 8.3: CIMS curve for the nanopillar in Fig. 8.2 at zero field at room temperature. The positive switching current is not seen because it is higher than the limit (18 mA) of our current supply.

because of the limit (18 mA) of our dc-current supply. The difference in the switching currents $\Delta I = I^+ - I^-$ for the Co(4) nanomagnet with SAF polarizing layer is greater than 31.5 mA. None of our 5 samples with an SAF polarizer showed a positive current switching (from P to AP). However, the average δI for 5 samples is > 31 mA. Whereas, the average ΔI for 4 Co(20)/Cu(10)/Co(4) nanopillars is 8.5 mA. This dramatic increase in the switching currents of a Co(4) nanomagnet is attributed to the reduction in the spin polarization and thus reduction in the spin transfer to the Co(4) nanomagnet due to an SAF polarizer. Since only the top Co(4) nanomagnet switches with current, the change in resistance, ΔR for CIMS (see Fig. 8.3) is the same as the ΔR for MR (see Fig. 8.2) between the P and AP alignments of the two Co(4) layers.

8.3 Summary

We fabricated magnetically uncoupled nanopillars with a SAF polarizer and observed a reduction in spin polarization that results in a decrease in MR as seen in Fig. 8.2. The reduction in the spin polarization also causes a reduction in the spin-transfer to the Co(4) nanopillar, which in turn switches at a higher current by a factor of more than 3.6 compared to our magnetically uncoupled Co(20)/Cu(10)/Co(4) samples. Our results agree with the results of Emley et al. [142], in which they studied the same effect in nanopillars with Co(11.5)/Ru(0.7)/Co(8)/Cu(6)/Co(2)/Cu(2)/Pt(30) structure, where they patterned all Co layers into a nanopillar shape but adjusted the thicknesses of Co layers in the SAF such that the dipolar coupling to the free layer is minimal. Thus, we essentially study similar geometries. They also observed a reduction in the ΔRs and also an increase in the switching current densities by a factor of $\sim$ 2.3 compared to their magnetically uncoupled Co(40)/Cu(10)/Co(3) samples. Although it is not clear whether the comparisons between the MRs of samples with and without SAFs are legitimate due to their unequivalent structures, the comparison between their switching currents is legitimate because only the free Co nanomagnet switches with current.

We conclude that the spin polarization and spin transfer could be reduced by using an SAF as a polarizing layer in a nanopillar. Such reductions in the spin transfer requires higher current densities for CIMS, which may be useful for some technological applications such as CPP-MR read heads.

Chapter 9

Effect of asymmetric leads on the switching currents of nanopillars

9.1 Introduction

Manschot et al. [58] recently predicted that J_s^+, the positive switching current density needed to flip the switching layer from parallel (P) to antiparallel (AP) to the fixed layer, could be reduced by up to a factor of five in a $Co_{fixed}/Cu/Co_{free}$ nanopillar through the use of asymmetric leads having different effective resistances, $r^* = \rho \times l_{sf}$ = resistivity times spin-diffusion length. Assuming a simple one-dimensional model with no magnetic coupling in which the bulk scattering is neglected, they argued that combining a large r^* for the lead B outside of the switching layer, with a small r^* for the lead A outside of the fixed (polarizing) layer, could reduce J_s^+ by up to a factor of five. They also predicted that reversing such a B and A pair would invert the CIMS, i.e. that positive current would switch the sample from AP to P. Manschot et al. assumed that the F- and N-layers within the leads of primary interest were much thinner than their spin-diffusion lengths, and that all of the interfaces were the same and also produced no spin-flipping. While these assumptions are not necessarily valid for our samples, we adopt them for the moment

to obtain simple Manschot predictions.

9.2 Experiment

Testing the Manschot prediction requires F-layers with l_{sf}^{F} longer than their layer thicknesses, t_F, since otherwise the effects of the leads on both the magnetoresistance (MR) and CIMS will be minimal. Then one needs non-magnetic leads N, on the two sides of the nanopillar with very different values of r^*, and with lengths thicker than their respective values of l_{sf}, so that r^* can have its full effect. As F-metal, Manschot et al. proposed using Co, for which l_{sf}^{Co} (4.2K) is probably $\sim$ 60 nm [143] and l_{sf}^{Co}(RT) (RT = room temperature) is probably $\sim$ 38 nm [143]. We adopt their proposal of Co and chose a thickness of 20 nm to be less than the likely room temperature l_{sf}^{Co}. For the N-lead pair they proposed Pt for the smaller r^* and Cu for the larger r^*. For our sputtered metals at 4.2K we estimate $r_{Pt}^* = \rho_{Pt}(42\ \text{n}\Omega\text{m}) \times l_{sf}^{Pt}(14\ \text{nm}) \approx 0.6\ \text{f}\Omega\text{m}^2$ [99], and $r_{Cu}^* = \rho_{Cu}(5\ \text{n}\Omega\text{m}) \times l_{sf}^{Cu}(500\ \text{nm}) = 2.5\ \text{f}\Omega\text{m}^2$ [144]. Cu as top lead outside of B, however, cannot have full effect in our nanopillars, since its thickness would have to be $\ll l_{sf}^{Cu}$ before reaching the Au capping layer that we need to obtain clean top contacts to our nanopillar. For large r^* we have chosen instead the alloy AgSn(5%), which has both a much shorter $l_{sf}^{AgSn} \sim 25$ nm and a larger $r_{AgSn}^* \sim 5\ \text{f}\Omega\text{m}^2$ [144]. In this paper we compare switching currents for samples with A = Pt and B = AgSn and, for comparison, with just Cu outside the fixed layer and Au outside the switching one (i.e., with A = B = 0). We estimate $r_{Au}^* = \rho_{Au}(20\ \text{n}\Omega\text{m}) \times l_{sf}^{Au}(60\ \text{nm}) = 1.2\ \text{f}\Omega\text{m}^2$. Combining these various metals or alloy gives the values of $rr^* = r_B^*/r_A^*$ listed in the second column of Table 9.2. With increasing temperature, ρ will increase and l_{sf}

will decrease, but we assume that their product r^* should be nearly independent of temperature.

Our sample preparation and fabrication techniques are described in detail in Chapter 3. As illustrated in Fig. 9.1, to minimize dipolar coupling between the two Co layers of our nanopillars, we stop our ion-milling within the middle Cu spacer layer, so that the in-plane length scales of both our fixed Co layer and part of the Cu layer are several microns. Our samples thus differ from the simple uniform linear assumption of Manschot et al. [58].

The multilayered nanopillars to be compared had the forms:

1. Cu(80)/**Co(20)/Cu(10)/Co(4)**/Cu(5)/Au(110) (Fig. 9.1a)

2. Cu(80)/Pt(20)/**Co(20)/Cu(10)/Co(4)**/AgSn(30)/Au(110) (Fig. 9.1b)

3. Cu(80)/AgSn(30)/**Co(20)/Cu(10)/Co(4)**/Pt(20)/Au(110) (Fig. 9.1c)

with all thicknesses in nm. The approximate sputter deposition rates for the constituents of our samples are given in Table 9.1. For ease of description, we label the samples by A/X/B, where X = Co(20)/Cu(10)/Co(4), A is the insert of interest to the left of X, and B is the insert to the right of X. The Cu(80) layer is the bottom contact and the Au(110) is composed of $\sim$ 10 nm of the last layer of the nanopillar plus an additional 100 nm thickness of the top contact. The thicker and much wider bottom Co layer switches more easily than the thinner and narrower bottom Co layer upon application of a magnetic field, but won't switch upon application of a current. The AgSn(5%) alloy was made by inserting Sn plugs into a Ag sputtering target. We estimated the atomic percent Sn from measurements on separate 200 nm thick test

films using Energy-Dispersive-Spectroscopy (EDS), which gave $\sim$ 5 at.%, and measurements of the residual resistivity, which gave $\sim$ 150 nΩm corresponding to $\lesssim$ 4 at. %. [103].

Target	Cu	Pt	Au	Co	AgSn(5%)
Deposition rate (Å/s)	10	4	3	4.5	7

Table 9.1: Approximate sputter deposition rates of Cu, Pt, Au, Co and AgSn(5%).

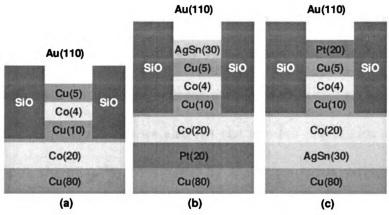

Figure 9.1: Cross-sectional cartoons of (a) X=Co(20)/Cu(10)/Co(4), (b) A=Pt(20)/X/B=AgSn(30), and (c) A=AgSn(30)/X/B=Pt(20) magnetically uncoupled nanopillars. All thicknesses are in nm.

A problem in determining reliable values of I_s^+ is the irreproducibility of coupling, magnetoresistance, and switching currents, due to uncontrolled variations in nanopillar shape and to incompletely controlled interface resistance with the top contact. In our analysis, we include data only for samples that showed both nearly single step magnetoresistance (MR) occurring after the magnetic field H passed zero (consistent with weak or no magnetic coupling, which is also stipulated by Manschot et al.), and CIMS with values of resistances in the P and AP states that agreed well with those for the MR. Fig. 9.2 shows three examples of MR and CIMS for samples with A = Pt(20) and B =AgSn(30). Fig. 9.3 shows three examples for the inverse situation,

A = AgSn(30) and B = Pt(20). Note that the values of I_s vary substantially from sample to sample. In both cases we use the standard convention that positive current I^+ flows from the thick to the thin Co layer. However for the case of A = AgSn(30) and B = Pt(20) we did not observe inverse CIMS as predicted by Manschot et al. [58]. Table 9.2 lists average values (with standard deviations) of: the resistance in the AP-state, R(AP), magnetoresistance, MR(%), difference in switching currents, $\Delta I = I^+ - I^-$, switching current for negative, I^-, and switching current for positive current, I^+, for samples with Pt and AgSn on opposite sides of the samples and, for comparison, samples from different sources with A = B = 0, i.e. with just Cu and Au contacts. For each sample set we also list the number of samples averaged.

We focus upon the quantity considered by Manschot et al., namely I^+ (since all of our samples have the same nominal area, I^+ is proportional to J^+). Manschot predicted that I^+ would be much smaller for A = Pt, B = AgSn than for a nanopillar with symmetric contacts, and that I^+ would be 'inverted' for A = AgSn, B = Pt. In contrast, our average values of I^+ for both orientations of Pt and AgSn are similar to each other (to within mutual uncertainties), and are also similar to those for our 'comparison' samples with A = B = 0. While the comparison samples are not strictly 'symmetric', their values of rr^* are intermediate between those for A = Pt, B = AgSn and A = AgSn, B = Pt. As checks upon our values of ΔI and I^+ for A = B = 0, we list values of both obtained independently by a different one of us, and also our best estimate of ΔI from data from the Cornell group in ref. [141]. For this comparison, we took the Cornell value of $\Delta J = 14 \times 10^7$ A/cm^2 from Fig. 2 in [141] and multiplied by the nominal area of $A = 70 \times 130$ nm^2 to get rounded $\Delta I = 12.7$ mA. Both of

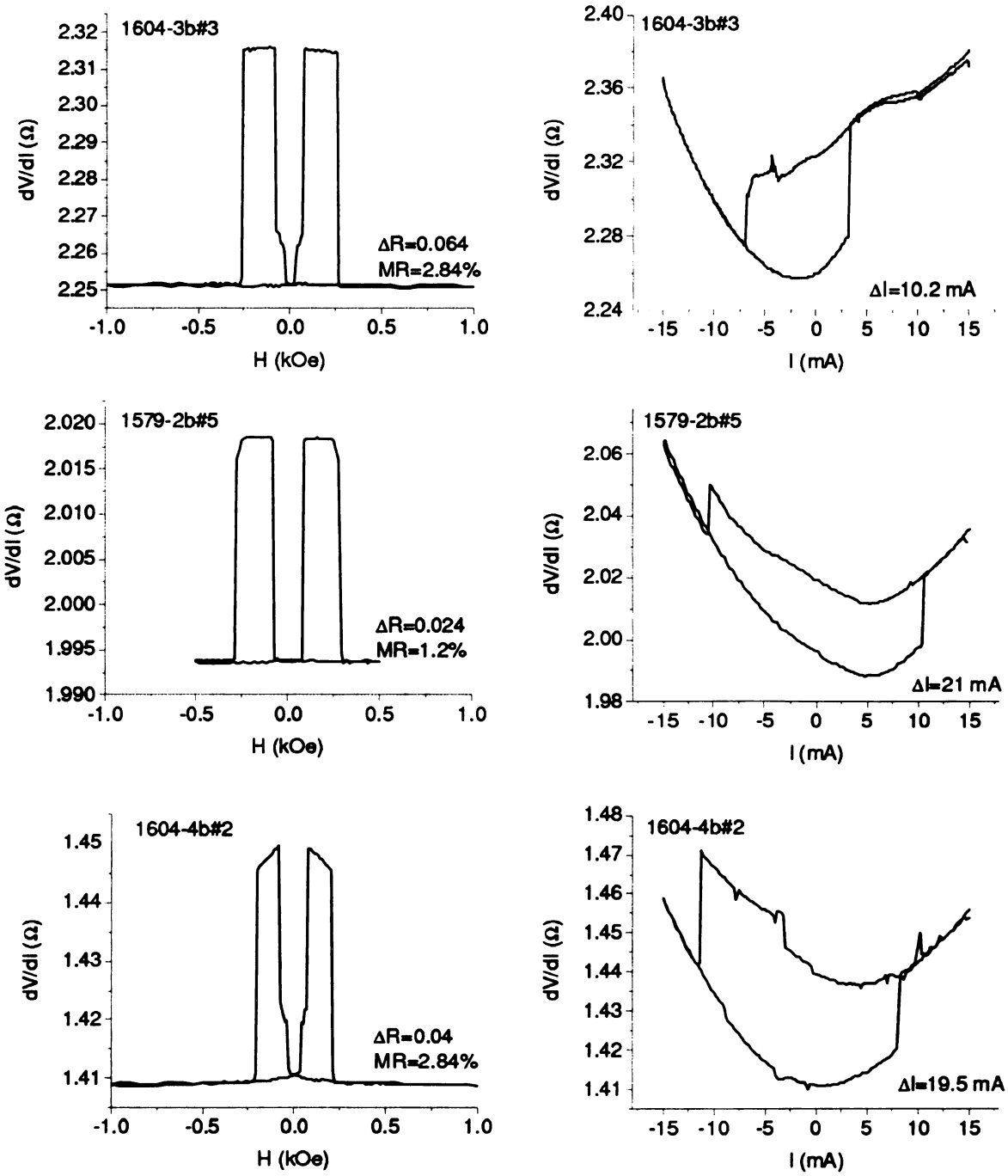

Figure 9.2: Examples of MR and CIMS curves for A=Pt(20)/X/B=AgSn(30) nanopillars at room temperature.

these other results are consistent with ours to within mutual uncertainties.

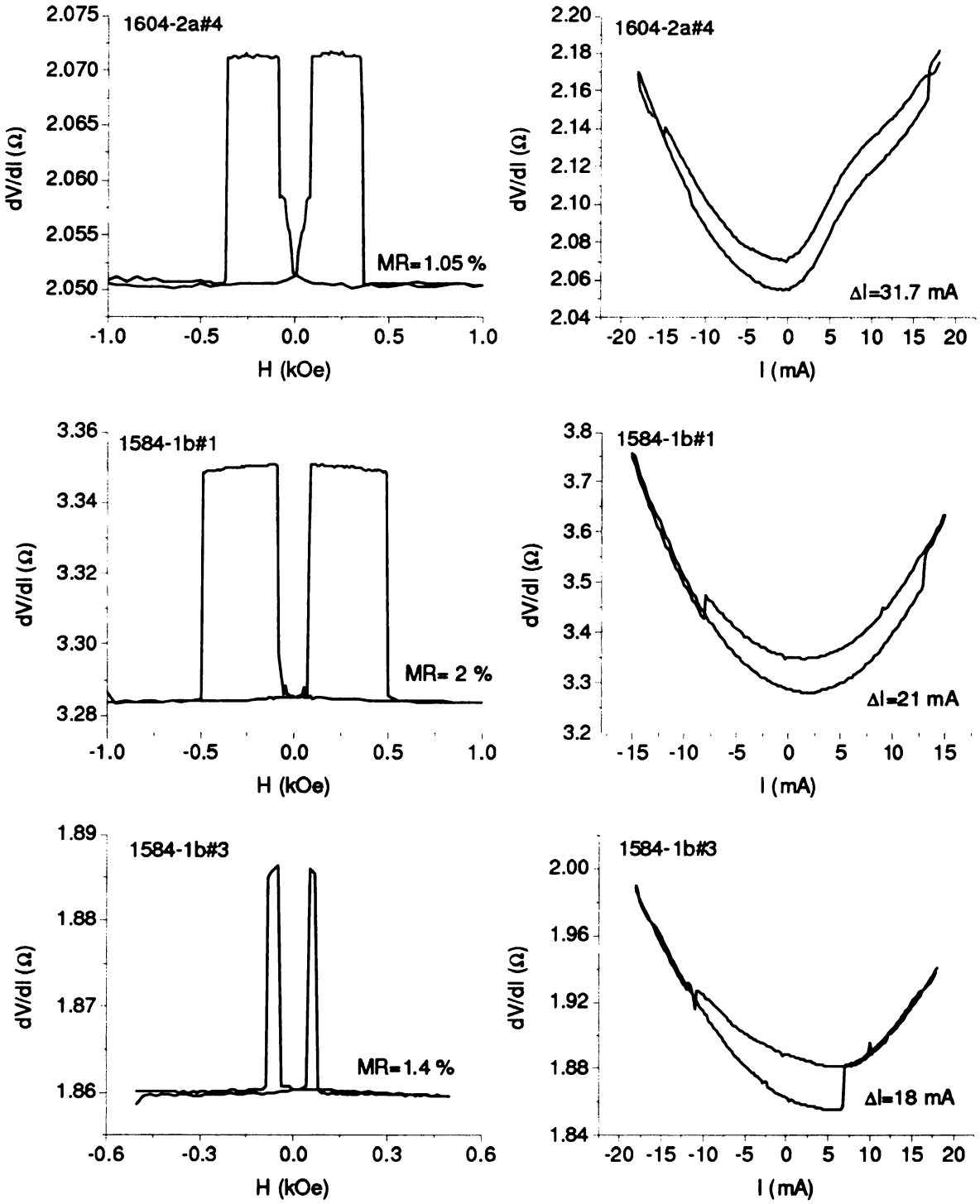

Figure 9.3: Examples of MR and CIMS curves for A=AgSn(30)/X/B=Pt(20) nanopillars at room temperature.

9.3 Summary

We have tested the Manschot prediction [58] that I^+, the positive current needed to switch Co/Cu/Co nanopillar from the P state to the AP state could be greatly

A/X/B (# of samples)	rr^*	R(AP) (Ω)	MR (%)	ΔI (mA)	I^- (mA)	I^+ (mA)
Pt(20)/X/AgSn(30) (13)	8.3	2.2	2.6	15 ± 5	-7.5 ± 2.5	7.5 ± 2.5
AgSn(30)/X/Pt(20) (4)	0.12	3.3	1.5	20 ± 7	-9.5 ± 3.5	10.3 ± 5
X (4)	0.5	1.4	5.4	8.5 ± 1.6	-2.85 ± 0.6	5.7 ± 1.2
X (AlHajDarwish) (8)	0.5	1.0	5.6	13.5 ± 2	-5 ± 1	8.5 ± 2
X (Cornell [141]) (4-10)	0.24			12.7		

Table 9.2: Average values of $rr^* = r_B^*/r_A^*$, R(AP), MR(%), $\Delta I = I^+ - I^-$, I^- and I^+ for our samples of the form Cu(80)/A/X/B/Au(110) with X = Co(20)/Cu(10)/Co(4), and A, B = Pt(20), AgSn(30), or nothing. The AlHajDarwish samples are similar to our ones without Pt and AgSn, except that the thickness of the fixed Co layer is 30 nm.

reduced by placing a lead with large r^* outside the switching F-layer and one with much smaller r^* outside the fixed layer. We successfully fabricated magnetically uncoupled nanopillars with equivalent asymmetric leads as proposed by Manschot et al. [58] yet we did not observe any reduction in the positive switching current. Upon switching the sides of the asymmetric leads we did not observe the predicted inverse CIMS behavior either. We observed little difference between I^+ or ΔI for nanopillars with A = Pt and B = AgSn and nanopillars with A = AgSn and B = Pt. Either the Manschot assumption of a one-dimensional geometry, or some other part of the analysis (e.g. neglecting bulk scattering), is inadequate for describing our nanopillars.

Chapter 10

Effect of lower demagnetizing fields on the switching currents of nanopillars

10.1 Introduction

The high critical switching current densities of nanopillars has been an obstacle for some technological uses. Katine et al. [46] derived the critical switching currents from the original theory of Slonczewski [33] as:

$$I_c^+ = \frac{\alpha\gamma eS}{g(0)}[H_{eff}(0) + 2\pi M] \tag{10.1}$$

$$I_c^- = \frac{\alpha\gamma eS}{g(\pi)}[H_{eff}(\pi) - 2\pi M] \tag{10.2}$$

where α is the phenomenological Gilbert damping constant, γ is the gyromagnetic ratio, M is the magnetization of the nanomagnet, S is the total spin of the nanomagnet, and $H_{eff} = H_{an}\cos(\theta) + H_{ext} - H_{exc}$ is the sum of anisotropy, external and exchange (but not demagnetizing) fields. $g(\theta)$ is a coefficient that depends on the spin polarization of the thick (fixed) ferromagnet and the relative orientations of magnetizations.

For $H_{ext} = 0$ the switching currents become dependent only on the anisotropy,

exchange and demagnetizing fields of which the contribution from the demagnetizing field is much larger compared to the exchange and anisotropy fields for a Co thin film that has in-plane anisotropy. The demagnetizing field for a ferromagnetic thin film is the field required to pull the in-plane magnetic moment of the sample perpendicular to the plane and is proportional to the magnetization M of the sample. Due to the large shape anisotropies of thin film ferromagnets, they require very high external fields (couple of Teslas) to demagnetize.

In this chapter we study the effect of lower demagnetizing fields on the switching currents of nanopillars by comparing the MRs and the switching currents of Au/Co(t)/Au nanomagnets (where for Au/Co(1 nm)/Au nanomagnet the easy axis is normal to the sample plane) with the MRs and the switching currents of Cu/Co(t)/Au nanomagnets given in Ref. [141].

10.1.1 Perpendicular anisotropy in Au/Co/Au systems

For a thin film ferromagnet the magnetization usually lies in the plane of the sample due to large shape anisotropy [145]. Previous studies of epitaxially grown very thin (< 1 nm) Co layer sandwiched between two Au layers gives perpendicular anisotropy [146] i.e. the magnetization easy axis is perpendicular to the Co/Au interface. The possible reasons for perpendicular anisotropy of such ferromagnetic thin films are the large anisotropy of the orbital moment [147] and the strain at a Co/Au interface resulting from a large (14%) lattice mismatch [148]. The perpendicular anisotropy decreases as the thickness of Co increases and disappears at about $t_{Co} = 20$ Å for a Au/Co/Au system and at $t_{Co} = 10$ Å for a Cu/Co/Cu system [149]. Although most

studies on perpendicular anisotropy are done with epitaxially grown samples, similar behaviors were also observed in sputtered Au/Co/Au systems [147] for up to 1.2 nm thick Co [150].

As the thickness of a Co layer sandwiched between two Au layers increases above 1 nm the strength of the perpendicular anisotropy decreases with some magnetic domains still preferring to stay in the perpendicular direction and others preferring to stay in-plane in a multi-domain sample. The interfacial interaction between Co/Au causing the perpendicular anisotropy is always present but as the thickness of Co increases the net anisotropy becomes in-plane. Having some magnetic domains lying perpendicular to the plane of a Co thin film should give demagnetizing fields smaller than those for a Co layer with the same thickness but with in-plane anisotropy.

10.2 Experiment

To determine the easy axes of of Co(t) layers sandwiched between Au layers, we sputtered Cu(40)/Au(10)[Co(t)/Au(10)]×5 samples and measured their magnetizations using a SQUID magnetometer by varying the angular position of the sample with respect to the external magnetic field. All thicknesses are given in nm. The Cu(40) is a buffer layer sputtered on a (100) Si wafer, Au(10) is selected to minimize exchange coupling between the Co layers and the structure is repeated 5 times to improve signals for a SQUID magnetometer. Fig. 10.1 shows the magnetization vs. angle at room temperature for Cu(40)/Au(10)[Co(1)/Au(10)]×5 and Cu(40)/Au(10)[Co(2)/Au(10)]×5 in an external magnetic field of 1000 Oe. The easy axis for Co(1) is in the perpendicular direction, whereas the easy axis for Co(2) is in the plane of the sample. Fig. 10.2

shows the magnetization vs. angular position of a Cu(40)/Au(10)[Co(1)/Au(10)]×5 sample at 500, 1000 and 5000 Oe at room temperature, which also shows that the magnetization of Co(1) sandwiched between Au layers has a perpendicular easy axis. The external field had to be increased up to 5000 Oe to eliminate any angular dependence.

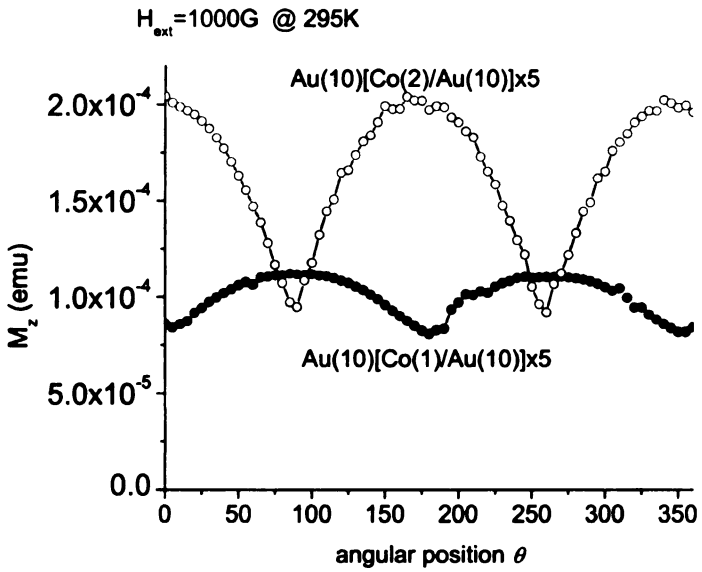

Figure 10.1: The magnetizations of Au[Co(1)/Au(10)]×5 (filled symbols) and Au[Co(1)/Au(10)]×5 (open symbols) samples as a function of angular position θ in a magnetic field of $H = 1000$ Oe at room temperature. θ is the angle between H and the sample plane.

The easy axes of Au/Co(t)/Au samples were also tested by making mm^2 Nb cross-stripped samples in the following forms and measuring $A\Delta R$ at 4.2K where Nb leads superconduct:

- Nb(150)/Cu(10)/Py(20)/Cu(10)/Co(t)/Cu(20)/Nb(150)
- Nb(150)/Cu(10)/Py(20)/Au(10)/Co(t)/Au(10)/Cu(10)/Nb(150)

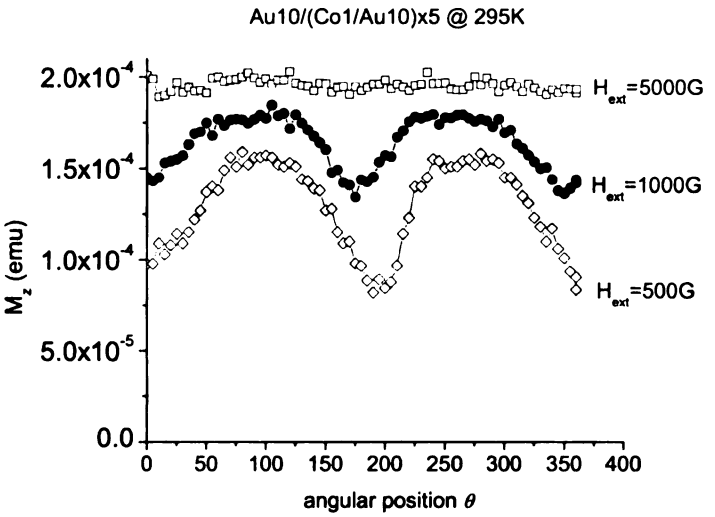

Figure 10.2: The magnetization of a Au[Co(1)/Au(10)]×5 film as a function of angular position θ in external magnetic fields of $H = 500, 1000$ and 5000 Oe at room temperature. θ is the angle between H and the sample plane.

The sample fabrication and measurement techniques for these macroscopic samples are given in detail in Chapter 3. Fig. 10.3 shows that $A\Delta R$ of Au/Co(t)/Au samples decreases as t_{Co} decreases, whereas $A\Delta R$ of Cu/Co(t)/Cu samples hardly varies from $t = 4$ nm to $t = 1$ nm. The fact that the easy axis for Au/Co(1)/Au layers is normal to the sample plane and yet we still have non-zero MRs much smaller than those for Cu/Co(1)/Cu samples indicates that Co(1) layer sandwiched between two Au(10) layers has partially perpendicular anisotropy.

All measurements described above were done for multi-domain polycrystalline samples. For a mono-domain nanomagnet the physics may or may not be the same as there is no means of determining the easy axes of a mono-domain thin Co sandwiched between Au or Cu layers. The only way to see whether there is any partial perpendicular anisotropy is to compare the MRs of nanopillars where a thin Co is sandwiched between Au or Cu layers.

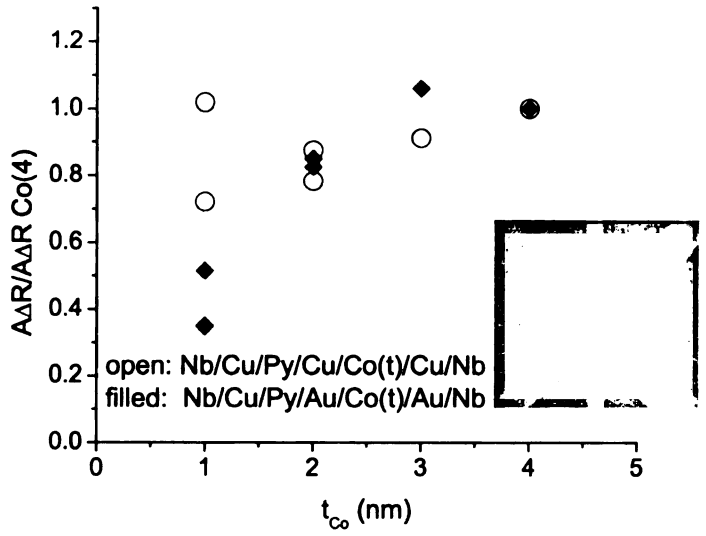

Figure 10.3: A comparison between $A\Delta R/A\Delta R(Co(4))$ of mm^2 Nb cross-stripped CPP samples with Co(t) sandwiched between Au and Cu layers at 4.2K. The inset shows a picture of a CPP-sample, where the CPP current flows through the overlap area of Nb strips at 4.2K.

We fabricated Cu(80)/Co(20)/Au(10)/Co(t)/Au(115) nanopillars with t =1, 2, 3 and 4 nm and measured the MR and switching currents. The details of the fabrication and measurement of our nanopillars are given in detail in Chapter 3. The sputter deposition rates were $\sim$ 2 Å/s for Co, $\sim$ 10 Å/s for Cu, and $\sim$ 5 Å/s for Au. Fig. 10.4 shows that the MR of these nanopillars decreases with decreasing t, which is also consistent with the magnetization and CPP-MR measurements given above. The quantitative studies in Ref. [141] show that the MR of their Co/Cu(10)/Co(t)/Au samples for t = 1.2, 3.6, and 6 nm hardly vary as t decreases, indicating that the Co/Cu and Co/Au interfaces are the dominant factors determining the MR in these thickness ranges, also consistent with our data for macroscopic CPP samples (see Fig. 10.3). These similarities in MRs of Co/Au/Co(t)/Au nanopillars and macroscopic samples makes us believe that the easy axes directions in both cases are the same.

To compare the critical current densities of our nanopillars, we need to divide the currents by the areas of the samples. As it was mentioned in Chapter 3 getting the exact shape and size of these nanopillars is almost impossible using our fabrication technique. However, the value of the resistances of these nanopillars show little deviation from one another, suggesting that the areas are not grossly different. Our nanopillars have nominal sizes of $\sim 130 \times 70$ nm and we approximate the effective areas of our samples as $\sim 0.01\mu m^2$.

Fig. 10.5 shows a comparison of the difference in switching currents $\Delta J = I^+ - I^-$ vs. t_{Co}^{free} for our Co/Au/Co(t)/Au nanopillars (filled circles) and Co/Cu/Co(t)/Au nanopillars (open circles) of Ref. [141]. Interestingly the critical currents of our Co/Au/Co(t)/Au nanopillars are very similar to those for Co/Cu/Co(t)/Au nanopillars given in Ref. [141]. Since the samples in Ref. [141] have a Au capping layer on top of the free Co(t) layer, the demagnetizing fields for these samples may also be smaller. However, the MRs of those samples show little or no variation with the thickness of Co, making us believe that those samples have in-plane anisotropy. For an elliptical Co(1) nanomagnet of the size $\sim 130 \times 70$ nm lateral dimensions with in-plane anisotropy, the approximate demagnetizing field is nearly the same as the demagnetizing field of a macroscopic Co(1) film, which is in the order of a couple of Tesla. However, by sandwiching a Co(1) layer between two Au(10) layers, we reduce the demagnetizing field (~ 0.5 Tesla see Fig. 10.2) of the nanomagnet which in turn should switch at a current smaller than the critical currents of Co/Cu/Co(1)/Au nanopillars [141]. The similarities in the switching currents of Co/Au/Co(t)/Au and Co/Cu/Co(t)/Au nanopillars suggests that the demagnetizing field makes little con-

tribution to the STT, inconsistent with equations 10.1 and 10.2.

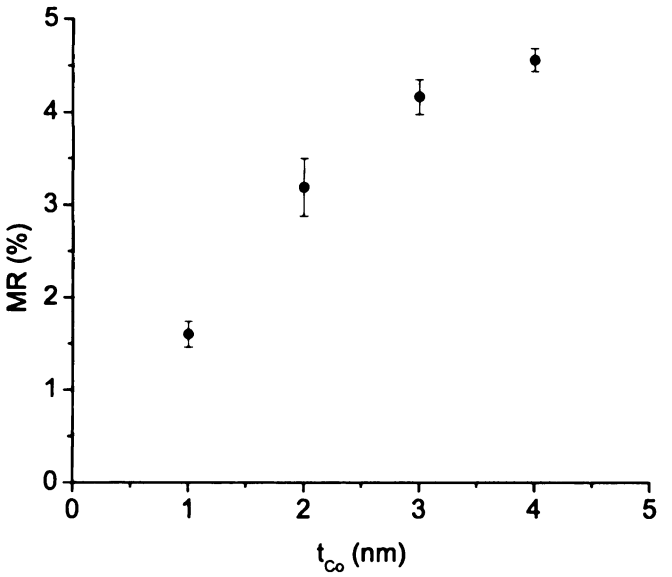

Figure 10.4: MR vs. t_{Co}^{free} of Co(20)/Au(10)/Co(t)/Au(115) nanopillars at room temperature. The MR increases as t increases up to 3-4 nm thick Co and then saturates.

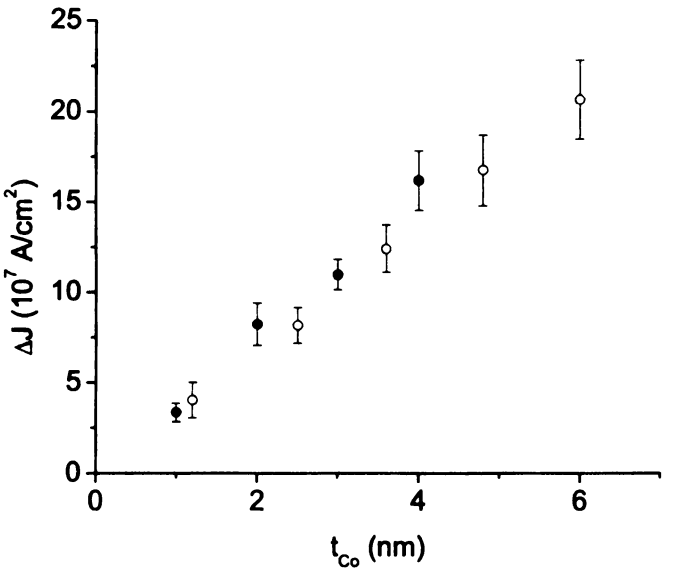

Figure 10.5: A comparison of $\Delta J = J_{+}^{P\rightarrow AP} - J_{-}^{AP\rightarrow P}$ vs. t_{Co}^{free} for Co(20)/Au(10)/Co(t)/Au(115) (filled circles) and Co/Cu(10)/Co(t)/Au (open circles) [141] nanopillars.

10.3 Summary

We observed that our sputtered large Au/Co(1)/Au samples have their easy axes normal to the plane, and therefore they should have lower demagnetizing fields than a Co(1) layer with in-plane anisotropy. The non-zero MR measurements of both mm^2 samples and nanopillars indicate that the net anisotropy of an Au/Co(t)/Au system is not perfectly perpendicular at least for t =1 and 2 nm. The critical switching currents of Co/Au/Co(t)/Au nanopillars with lower demagnetizing fields measured at room temperature surprisingly show almost no difference with the critical switching currents of Co/Cu/Co(t)/Au nanopillars of Ref. [141], inconsistent with equations 10.1 and 10.2. A linear decrease of the switching currents with decreasing thickness of the Co/Au/Co(t)/Au nanomagnets was also observed within the thickness ranges.

Chapter 11

Summary & Conclusions

In this thesis we have completed two studies involving current-perpendicular-to-plane magnetoresistance (CPP-MR)at 4.2K, and five studies of current-induced magnetization switching (CIMS) at room temperature and 4.2K.

CPP-MR

We have measured the spin diffusion lengths of sputtered N=Pd, Pt and Au. The interest in these metals arises from the fact that when combined with very thin layers of Co they give perpendicular anisotropy, which has potential uses in magnetic storage. To determine the effects of spin-orbit coupling on the spin memory loss at an interface formed by two nonmagnetic metals, we measured the spin memory losses at N/Cu interfaces and compared the results with previously published values of Nb/Cu and W/Cu. We found that the spin diffusion lengths of Pd, Pt, and Au are long enough so that these metals could be used in devices without excessive loss of spin polarization. Furthermore, the spin memory losses at Pt/Cu and W/Cu are similar, and spin memory losses at Pd/Cu and Nb/Cu are also similar, both of which are consistent with spin-orbit coupling being the major source of such losses at these N/N interfaces. However, for Au/Cu, the spin memory loss is smaller than those

for Pt/Cu and W/Cu. The sources of this weak spin-memory loss might be the low resistivity of Au, and the absence of d-electron states at the Au Fermi surface. We also measured the interface specific resistances of N/Cu and compared them with the no-free-parameter calculations for perfect and 50-50 alloy interfaces. For Ag/Au, Co/Cu, Fe/Cr, Pd/Cu, and Au/Cu, agreement (or disagreement) between the measured and calculated interface specific resistances correlates with small (large) lattice mismatch between the metals forming the interface.

Previous studies of CPP-MR with superconducting leads showed that the scattering anisotropy at a simple F/S interface is zero (i.e. no spin dependent scattering). Similar behavior was found with X = Ag or Cu inserts between various F-metals and S = Nb. Eid developed a 'null-detector' method for studying scattering anistropy at F/N/S 'interfaces', observing that inserting certain Xs could change (activate) the anisotropy. We reproduced his results and extended them to other X. We confirmed that X = Cu, Ag, or Cu/Ag, as well as the antiferromagnet FeMn, all gave no activation. In contrast, X = Au or Ru gave activation, even for thicknesses as small as 2 nm. Combinations of non-activating metals (Cu or Ag) next to F, with strong scattering metals next to S (Au, Ru, or FeMn) gave activation of the Cu or Ag. From these results, we concluded that activating an F/S interface seems to require strong spin-flipping at the N/S interface.

CIMS

Previous studies had shown that alloying F-metals with Cr produces negative bulk scattering anisotropies. By combining such alloys with themselves and with other

ferromagnets having positive bulk scattering anisotropies, we were able to produce all four combinations of normal and inverse CPP-MR and normal and inverse CIMS. In our samples, the direction of CIMS was set only by the net scattering anisotropy of the thick (polarizing) layer. The net scattering anisotropy of the thin (switching) layer was irrelevant. The importance of bulk properties of our F-layers in the observed behaviors of CIMS, shows that a diffusive treatment of the transport is crucial for explaining our results.

To test whether Ag and Au present viable alternatives to the commonly used Cu spacers, we compared CIMS switching currents for 10 nm thick N=Ag, Au and Cu spacers in a standard Py- based nanopillar structure. Since the Ag and Au spacers gave comparable switching currents to Cu, we concluded that Ag and Au could be used as alternative spacers in devices.

We used a synthetic antiferromagnet (SAF) as a polarizer layer in a nanopillar structure to successfully reduce the spin polarization and spin transfer into a nanomagnet, thereby increasing the switching currents by a factor of more than 3.6 relative to those for nanopillars with a Co(20) polarizer. Such increases in switching currents by using an SAF as a polarizer could be useful in devices that require higher switching currents, such as CPP-MR nanopillar read heads.

Using magnetically uncoupled (as stipulated by Manschot et al.) Co/Cu/Co nanopillar structures, we tested predictions by Manschot et al. that using asymmetric leads with very different effective resistances (resistivity times spin diffusion length) could: (a) reduce the positive switching current by up to a factor of 5, and (b) invert the switching current when these leads are reversed. Combining Pt (small

effective resistance) with AgSn (large effectiveresistance) did not significantly change the switching currents nor inverted the CIMS upon lead reversal.

A switching current formula written down by Katine et al. predicts lower switching currents for nanomagnets with lower demagnetizing fields. To study the effect of demagnetizing fields on the switching currents for CIMS, we fabricated magnetically uncoupled Co/Au/Co(t)/Au nanopillars (which should have perpendicular easy axes and therefore lower demagnetizing fields at least for $t = 1-2$ nm) and compared their switching currents with those of Co/Cu/Co(t)/Au nanopillars (which should have in-plane easy axes) of Albert et al. Interestingly, the difference between positive and negative switching currents for the two systems are almost the same, independent of t, suggesting that the demagnetizing fields do not have a strong effect on the switching currents of nanopillars.

Appendix A

Determining the resistivities of metals and alloys

A.1 Overview

To analyze our CPP-MR data we need to know the resistivities of the metals and alloys we use in our samples. To measure the resistivities of metals we used the van der Pauw [151] method, which can be used to measure the resistivity of any thin film metal or alloy of arbitrary shape without holes by measuring its sheet resistance.

The van der Pauw method gives us the resistivity in the CIP direction but actually what we need is the resistivity in the CPP direction. If we had perfect crystal cubic samples, the resistivities in both directions would be exactly the same but due to the columnar growth of our sputtered samples the CIP and CPP resistivities need not be the same.

Our technique developed for measuring the resistance R in the CPP direction involves sandwiching ferromagnetic (F) metals between two superconducting Nb strips. Such a resistance measurement is limited to temperatures below the superconducting transition temperature of Nb. A plot of AR (area times resistance) vs. thickness of F-metal is obtained by measuring the resistances (4.2K) and the areas of samples with

various thicknesses of the F-metal sandwiched between the Nb strips. The slope of this graph gives the resistivity of the F-metal. For normal (N) metals this technique can be used by putting F-layers next to both Nb leads to eliminate the proximity effect [59].

Test comparisons of CIP and CPP resistivities at 4.2K gave similar values as illustrated by the resistivities of Co and CoZr (2.5% Zr) in Table A.1 [57].

Metal	CIP $\rho_{4.2K}(\mu\Omega cm)$	CPP $\rho_{4.2K}(\mu\Omega cm)$
Co	5.1 ± 2	4.0 ± 0.7
CoZr (2.5% Zr)	20.7 ± 1.0	19 ± 1

Table A.1: A comparison between the CIP and CPP resistivities of Co and CoZr at 4.2 K [57].

Since these van der Pauw CIP resistivities and the trilayer CPP resistivities of similarly sputtered films agree, we choose to measure the CIP resistivities using the van der Pauw method, which is much easier.

A.2 Technique

Van der Pauw instructs us to measure the resistance of a thin metal film as shown in Fig. A.1 [151]. The resistivity of the metal in Fig. A.1, ρ, is then given by:

$$\rho = \frac{\pi t}{\ln 2}\left(\frac{R_1 + R_2}{2}\right) f, \tag{A.1}$$

where t is the thickness of the film and f is the correction factor to the resistivity, which is a function of R_1/R_2. If $R_1 = R_2$ then $f = 1$. However, if $R_1 \neq R_2$ (asymmetric cases) one has to determine the value of f from f vs. R_1/R_2 graph shown in Fig. A.2. Notice that in Fig. A.1 there is no current contact between

voltage leads and no voltage contact between current leads: as such connection would invalidate Equation. A.1.

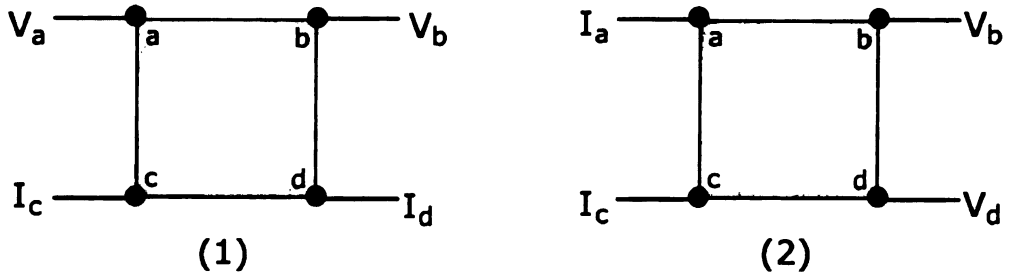

Figure A.1: The van der Pauw geometry for a thin film metal: (1) the resistance is $R_1 = |V_{ab}/I_{cd}|$, (2) the resistance is $R_2 = |V_{bd}/I_{ca}|$.

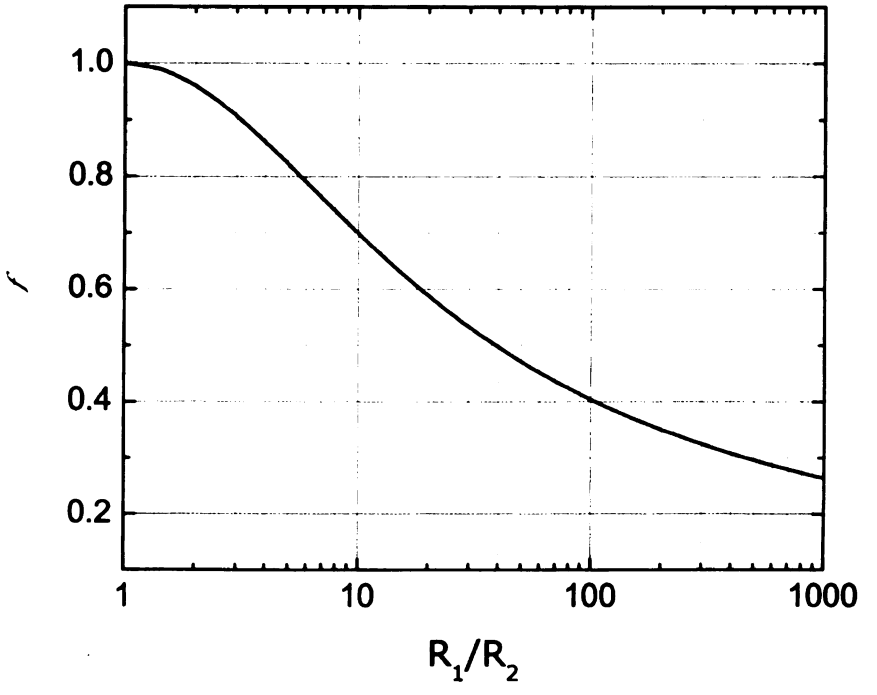

Figure A.2: The graph of correction factor f vs. R_1/R_2, which is plotted using a numerical solution to Equation A.2.

$$\cosh\left[\frac{(R_1/R_2)-1}{(R_1/R_2)+1}\cdot\frac{\ln 2}{f}\right] = \frac{1}{2}\exp\frac{\ln 2}{f} \qquad \text{(A.2)}$$

A.2.1 Samples and Measurement

Our samples are thin films of metals or alloys sputtered on Si substrates, and have close to square or rectangular shapes with 200-300nm thicknesses. The four-probe measurement was done by putting indium on each corner of our thin films and cold pressing on the leads. It is important to make the contacts on the periphery of the films because the van der Pauw derivation for resistivity assumes the contacts on the periphery of the film [151]. The samples were mounted on a "quick dipper" which we used to dip the sample into a liquid helium dewar to make low temperature (4.2K) measurements. We also used the same dipper to measure at room temperature.

Measurements were made using a dc current source and a nanovoltmeter. We used very low currents (< 30mA) and immediate voltage reading to prevent excess heating. To check the linearity in the resistances we used several different currents ranging between 1-30 mA. These measurements were also repeated with reversed currents to eliminate any thermoelectric effects and voltage offset of the nanovoltmeter.

A.3 Results

The metals studied in this thesis are Pd, Pt, Au and Nb. We also studied a silver and tin alloy $Ag_{0.95}Sn_{0.05}$. Using the van der Pauw technique we measured the resistivities of these conductors both at room temperature and at 4.2K except Nb, because Nb superconducts at 4.2K. We measured the transition temperatures of Nb samples and also measured the resistivities of Nb films at 12K. Following tables show the individual samples' resistivities calculated from their respective resistances using Equation A.1 and A.2.

Au Samples	$\rho(295K)(n\Omega m)$	$\rho(4.2K)(n\Omega m)$	$\Delta\rho(n\Omega m)$
h1387-8a	47.83	25.24	22.59
h1388-8a	32.40	9.16	23.24
h1388-8b	43.99	20.72	23.27
h1397-8a	36.05	12.64	23.41
h1397-8b	60.19	32.90	27.29
h1398-8a	43.46	18.79	24.67
h1398-8b	48.15	22.14	26.01
h1399-8a	38.06	13.80	24.26
Averages	44 ± 8	19 ± 6	24 ± 2

Table A.2: The resistivities of sputtered gold (Au) samples at 295K and 4.2K and their differences. $\Delta\rho = \rho(295K) - \rho(4.2K)$.

Pt Samples	$\rho(295K)(n\Omega m)$	$\rho(4.2K)(n\Omega m)$	$\Delta\rho(n\Omega m)$
h1363-8a	164.00	37.45	126.55
h1364-8a	168.17	50.79	117.38
h1368-8b	153.94	36.51	117.43
h1368-8a	167.20	47.08	120.12
h1364-8b	153.30	38.21	115.09
Averages	161 ± 7	42 ± 6	119 ± 4

Table A.3: The resistivities of sputtered platinum (Pt) samples at 295K and 4.2K and their differences. $\Delta\rho = \rho(295K) - \rho(4.2K)$.

Pd Samples	$\rho(295K)(n\Omega m)$	$\rho(4.2K)(n\Omega m)$	$\Delta\rho(n\Omega m)$
h1344-8b	155.0	42.28	112.72
h1345-8b	150.3	36.76	113.54
h1344-8a	166.7	40.75	125.95
Averages	157 ± 8	40 ± 3	117 ± 7

Table A.4: The resistivities of sputtered palladium (Pd) samples at 295K and 4.2K and their differences. $\Delta\rho = \rho(295K) - \rho(4.2K)$.

Nb Samples	$\rho(295K)(n\Omega m)$	$\rho(12K)(n\Omega m)$	$T_c(K)$	$\Delta\rho(n\Omega m)$
h1387-8b	194.55	43.58	8.88	150.97
h1369-8a	231.64	90.38	8.45	141.26
h1345-8a	203.34	46.57	9.00	156.77
Averages	210 ± 11	60 ± 15	8.78 ± 0.17	150 ± 5

Table A.5: The resistivities of sputtered niobium (Nb) samples at 295K and 12K and their differences. T_c represents superconducting transition temperatures. $\Delta\rho = \rho(295K) - \rho(12K)$.

$Ag_{0.95}Sn_{0.05}$ Samples	$\rho(295K)(n\Omega m)$	$\rho(4.2K)(n\Omega m)$	$\Delta\rho(n\Omega m)$
h1579-5a	170	149	21
h1579-5b	172	152	20
Averages	171 ± 1	150.5 ± 1.5	20.5 ± 0.5

Table A.6: The resistivity of sputtered silver-tin ($Ag_{0.95}Sn_{0.05}$) samples at 295K and 4.2K and their differences. $\Delta\rho = \rho(295K) - \rho(4.2K)$.

A.3.1 Discussion

Matthiessen's Rule

The electrical resistivity is a result of scattering of conduction electrons by other electrons, impurities, dislocations, phonons etc. If these scattering mechanisms are completely independent of each other, i.e. presence of one mechanism does not alter the way other mechanisms function, then, the total resistivity is simply the sum of resistivities due to all scattering mechanisms. This is known as Matthiessen's rule [1]. There are two types of scattering mechanisms in a metal:

1. Temperature independent e.g. elastic impurity scattering, (neither the concentration of impurities nor their interaction with electrons is affected by temperature).

2. Temperature dependent e.g. electron-electron and electron-phonon scattering.

According to the Matthiessen's rule the total resistivity is given by;

$$\rho(c,T) = \rho(T) + \rho(c), \tag{A.3}$$

where T is temperature and c is the concentration of impurities [1]. According to Eqn. A.3, the addition of impurities merely adds a constant component to the total resistivity, leaving the temperature dependent part unchanged. In reality Eqn. A.3 is

never exactly valid. There are always deviations from the Matthiessen's rule, which exist for several reasons which are explained in Ref. [152], but basically because the scattering mechanisms are not completely independent. However, in many cases these deviations are small compared to either $\rho(T)$ or to $\rho(c)$ or to both, and Matthiessen's rule represents quite a good approximation to the experimental results.

Let's consider two samples, one pure and the other has impurities. From Eqn. A.3 one can immediately see that the difference in the resistivities ($\Delta\rho = \rho(T_1) - \rho(T_2)$) at different temperatures depends only on temperature not impurities. Therefore, in theory both samples should have same $\Delta\rho$ because the impurity scattering is temperature independent.

Comparison with other measurements

Table A.7 shows that $\Delta\rho$ of our sputtered nominally-pure-metal samples differ from the $\Delta\rho$ of pure metal counterparts by $\sim$ 4.5-12 %, which is in the ballpark of observed deviations from Matthiessen's rule [152]. On the other hand, for a well defined alloy of $Ag_{0.95}Sn_{0.05}$ the difference between the $\Delta\rho$ of pure Ag and $\Delta\rho$ of sputtered $Ag_{0.95}Sn_{0.05}$ is 25% which is larger than those for sputtered pure metals.

Metal	$\Delta\rho_{pure}(n\Omega m)$	$\Delta\rho_{sputtered}(n\Omega m)$	Difference $_{\Delta\rho}(\%)$
Au	22	24 ± 2	10 ± 10
Pt	106.2	119 ± 4	12 ± 4
Pd	105.8	117 ± 7	11 ± 7
Nb	143.5	150 ± 5	4.5 ± 3.5
$Ag_{0.95}Sn_{0.05}$	16	20	25

Table A.7: A comparison between the $\Delta\rho$s of pure Au, Pt, Pd, Nb and Ag and their sputtered counterparts. $\Delta\rho = \rho(295K) - \rho(4.2K)$ except for Nb, for which $\Delta\rho = \rho(295K) - \rho(12K)$. The values of resistivities of the pure metals are taken from Ref. [103].

References

[1] N. W. Ashcroft and N. D. Mermin, *Solid State Physics* (Harcourt Brace College Publishers, Fort Worth, 1976).

[2] J. Bass, in *Magnetic Interactions and Spin Transport*, edited by S. W. A. Chtchelkanova and Y. Idzerda (Kluwer Academic/Plenum Publishers, NY, 2003), Chap. 4.Magnetotransport (Experimental), pp. 219–312.

[3] J. L. Olsen, *Electronic Transport in Metals* (John Wiley and Sons, NY, 1962).

[4] E. Fawcett, Adv. Phys. **13**, 139 (1964).

[5] R. M. Bozorth, *Ferromagnetism* (D. Van Nostrand Co., NY, 1951).

[6] I. A. Campbell, A. Fert, and O. Jaoul, J. Phys. C Suppl. **1**, S95 (1970).

[7] J. A. Brug *et al.*, J. Appl. Phys. **79**, 4491 (1996).

[8] G. Binasch, P. Grunberg, F. Saurenbach, and W. Zinn, Phys. Rev. B **39**, 4828 (1989).

[9] M. N. Baibich *et al.*, Phys. Rev. Lett. **61**, 2472 (1988).

[10] P. Grunberg *et al.*, Phys. Rev. Lett. **57**, 2442 (1986).

[11] P. M. Levy, in *Solid State Physics*, edited by H. Ehrenreich and D. Turnbull (Academic Press, Cambridge MA, 1994), Vol. 47, Chap. Giant magnetoresistance in magnetic layered and granular materials, pp. 367–462.

[12] T. Valet and A. Fert, Phys. Rev. B **48**, 7099 (1993).

[13] S. S. P. Parkin, N. More, and K. P. Roche, Phys. Rev. Lett. **64**, 2304 (1990).

[14] S. S. P. Parkin, R. Bhadra, and K. P. Roche, Phys. Rev. Lett. **66**, 2152 (1991).

[15] J. Noguésa and I. Schuller, J. Magn. Magn. Mater. **192**, 203 (1999).

[16] B. Dieny *et al.*, J. Appl. Phys. **69**, 4774 (1991).

[17] J. M. Slaughter, W. P. Pratt, Jr., and P. A. Schroeder, Rev. Sci. Instrum. **60**, 127 (1989).

[18] P. Dauguet, P. Gandit, and J. Chaussy, J. Appl. Phys **79**, 5823 (1996).

[19] L. Piraux *et al.*, Appl. Phys. Lett. **65**, 2484 (1994).

[20] A. Blondel, J. P. Meier, B. Doudin, and J.-P. Ansermet, Appl. Phys. Lett. **65**, 3019 (1994).

[21] K. Liu, K. Nagodawithana, P. C. Searson, and C. L. Chien, Phys. Rev. B **51**, 7381 (1995).

[22] S. Zhang and P. M. Levy, J. Appl. Phys. **69**, 4786 (1991).

[23] S. F. Lee *et al.*, J. Magn. Magn. Mater. **118**, L1 (1993).

[24] M. A. M. Gijs and G. E. W. Bauer, Adv. in Phys. **46**, 285 (1997).

[25] W. P. Pratt, Jr. *et al.*, Phys. Rev. Lett. **66**, 3060 (1991).

[26] http://www.nve.com.

[27] http://www.research.ibm.com/research/gmr.html.

[28] http://www.toshiba.co.jp/about/press/2004_12/pr1401.htm.

[29] http://www.hitachigst.com/hdd/research/.

[30] http://www.seagate.com/cda/newsinfo/newsroom/.

[31] S. F. Lee *et al.*, Phys. Rev. B **52**, 15426 (1995).

[32] M. A. M. Gijs, S. K. J. Lenczowski, and J. B. Giesbers, Phys. Rev. Lett. **70**, 3343 (1993).

[33] J. C. Slonczewski, J. Magn. Magn. Mater. **159**, L1 (1996).

[34] L. Berger, Phys. Rev. B **54**, 9353 (1996).

[35] L. Berger, J. Appl. Phys. **89**, 5521 (2001).

[36] M. D. Stiles and J. Miltat, in *Spin dynamics in confined structures*, edited by B. Hillebrands and A. Thiaville (Springer, NY, 2005).

[37] M. Tsoi *et al.*, Phys. Rev. Lett. **80**, 4281 (1998).

[38] J. C. Slonczewski, J. Magn. Magn. Mater. **195**, L261 (1999).

[39] S. I. Kiselev *et al.*, Nature **425**, 380 (2003).

[40] S. I. Kiselev *et al.*, Phys. Rev. Lett. **93**, 036601 (2004).

[41] M. R. Pufall *et al.*, Phys. Rev. B **69**, 214409 (2004).

[42] I. N. Krivorotov *et al.*, Science **307**, 228 (2005).

[43] W. H. Rippard *et al.*, Phys. Rev. B **70**, 100406(R) (2004).

[44] J. Z. Sun, J. Magn. Magn. Mater. **202**, 157 (1999).

[45] E. B. Myers *et al.*, Science **285**, 867 (1999).

[46] J. A. Katine *et al.*, Phys. Rev. Lett. **84**, 3149 (2000).

[47] J. Bass, S. Urazhdin, N. O. Birge, and W. P. Pratt, Jr., phys. stat. sol. (a) **201**, 1379 (2004).

[48] S. Urazhdin, N. O. Birge, W. P. Pratt, Jr., and J. Bass, Phys. Rev. Lett. **91**, 146803 (2003).

[49] C. Heide, Phys. Rev. Lett. **87**, 197201 (2001).

[50] C. Heide, P. E. Zilberman, and R. J. Elliott, Phys. Rev. B **63**, 064424 (2001).

[51] C. Heide, Phys. Rev. B **65**, 054401 (2001).

[52] Y. Ji, C. L. Chien, and M. D. Stiles, Phys. Rev. Lett. **90**, 106601 (2003).

[53] M. L. Polianski and P. W. Brouwer, Phys. Rev. Lett. **92**, 026602 (2004).

[54] M. D. Stiles, J. Xiao, and A. Zangwill, Phys. Rev. B **69**, 054408 (2004).

[55] B. Ozyilmaz *et al.*, Phys. Rev. Lett. **93**, 176604 (2004).

[56] J. Sun, Nature **425**, 359 (2003).

[57] K. F. Eid, Ph.D. thesis, Michigan State University, 2002.

[58] J. Manschot, A. Brataas, and G. E. W. Bauer, Appl. Phys. Lett. **85**, 3250 (2004).

[59] S.-F. Lee, Ph.D. thesis, Michigan State University, 1994.

[60] P. R. J. Holody, Ph.D. thesis, Michigan State University, 1996.

[61] J. Bass and W. P. Pratt, Jr., J. Magn. Magn. Mater. **200**, 274 (1999).

[62] J. Bass *et al.*, Mat. Sci. and Eng. B **31**, 77 (1995).

[63] D. Bozec *et al.*, Phys. Rev. Lett. **85**, 1314 (2000).

[64] E. Tsymbal and D. Pettifor, in *Solid State Physics* (Academic Press, San Diego, 2001), Vol. 56, p. 113.

[65] W. H. Butler, X.-G. Zhang, and J. M. MacLaren, J. Supercon. **13**, 221 (2000).

[66] E. Y. Tsymbal, Phys. Rev. B **62**, R3608 (2000).

[67] A. Shpiro and P. M. Levy, Phys. Rev. B **63**, 014419 (2001).

[68] K. Eid *et al.*, Phys. Rev. B **65**, 054424 (2002).

[69] W.-C. Chiang *et al.*, Phys. Rev. B **69**, 184405 (2004).

[70] R. J. Baxter, D. G. Pettifor, and E. Y. Tsymbal, Phys. Rev. B **71**, 024415 (2005).

[71] L. Berger, J. Appl. Phys. **81**, 4880 (1997).

[72] L. Berger, J. Appl. Phys. **93**, 7693 (2003).

[73] M. D. Stiles and A. Zangwill, J. Appl. Phys. **91**, 6812 (2002).

[74] A. Fert *et al.*, J. Magn. Magn. Mater. **272-276**, 1706 (2004).

[75] J. Barnas *et al.*, Phys. Rev. B **72**, 024426 (2005).

[76] J.-E. Wegrowe *et al.*, J. Appl. Phys. **91**, 6806 (2002).

[77] A. Fábián *et al.*, Phys. Rev. Lett. **91**, 257209 (2003).

[78] E. B. Myers *et al.*, Phys. Rev. Lett. **89**, 196801 (2002).

[79] S. Urazhdin, Phys. Rev. B **69**, 134430 (2004).

[80] S. Urazhdin, W. P. Pratt, Jr., and J. Bass, J. Magn. Magn. Mater. **272-276**, 1586 (2004).

[81] Z. Li and S. Zhang, Phys. Rev. B **69**, 134416 (2004).

[82] D. M. Apalkov and P. B. Visscher, cond-mat. **0405305**, (2004).

[83] D. M. Apalkov and P. B. Visscher, J. Magn. Magn. Mater. **286**, 370 (2005).

[84] K. J. Lee *et al.*, Nature Materials **3**, 877 (2004).

[85] I. N. Krivorotov *et al.*, Phys. Rev. Lett. **93**, 166603 (2004).

[86] J. Slonczewski, J. Magn. Magn. Mater. **247**, 324 (2002).

[87] A. Fert, J.-M. George, H. Jaffres, and G. Faini, J. Phys. D: Appl. Phys. **35**, 2443 (2002).

[88] J. Xiao, A. Zangwill, and M. D. Stiles, Phys. Rev. B **70**, 172405 (2004).

[89] M. AlHajDarwish *et al.*, Phys. Rev. Lett. **93**, 157203 (2004).

[90] G. K. White, *Experimental techniques in low-temperature physics*, 3rd ed. (Oxford University Press, Walton St. Oxford, 1979).

[91] *Handbook of Microlithography, Micromachining, and Microfabrication*, edited by P. Rai-Choudhury (SPIE Optical Engineering Press, Bellingham, Washington, 1997), Vol. 1: Microlithography.

[92] H. R. Kaufman, R. S. Robinson, and W. E. Hughes, *Characteristics, Capabilities, and Applications of Broad-Beam Sources* (Commonwealth Scientific Corporation, Alexandria, Virginia, 1987).

[93] W. Park *et al.*, Phys. Rev. B **62**, 1178 (2000).

[94] F. den Broeder, W. Hoving, and P. Bloemen, J. Magn. Magn. Mat. **93**, 562 (1991).

[95] K. Bussmann, G. A. Prinz, S.-F. Cheng, and D. Wang, Appl. Phys. Lett. **75**, 2476 (1999).

[96] J. A. Katine, F. J. Albert, and R. A. Buhrman, Appl. Phys. Lett. **76**, 354 (2000).

[97] K. Xia *et al.*, Phys. Rev. B **63**, 64407 (2001).

[98] G. E. W. Bauer, K. M. Schep, K. Xia, and P. J. Kelly, J. Phys. D: Appl. Phys. **35**, 2410 (2002).

[99] H. Kurt *et al.*, Appl. Phys. Lett. **81**, 4787 (2002).

[100] H. Kurt *et al.*, J. Appl. Phys. **93**, 7918 (2003).

[101] D. Baxter, S. Steenwyk, J. Bass, and W. P. Pratt, Jr., J. Appl. Phys. **85**, 4545 (1999).

[102] W. P. Pratt, Jr. *et al.*, IEEE Trans. Magn. **33**, 3505 (1997).

[103] J. Bass, in *Metals: Electronic Transport Phenomena*, Vol. 15a of *Landolt-Bornstein New Series Group III*, edited by K. H. Hellwege and J. L. Olsen (Springer, Berlin, 1982).

[104] P. Monod and S. Schultz, J. de Physique **43**, 393 (1982).

[105] M. Stiles and D. Penn, Phys. Rev. B **61**, 3200 (2000).

[106] L. L. Henry *et al.*, Phys. Rev. B **54**, 12336 (1996).

[107] J. Ji, A. Hoffmann, J. S. Jiang, and S. D. Bader, Appl. Phys. Lett. **85**, 6218 (2004).

[108] A. Zambano *et al.*, J. Magn. Magn. Mater. **253**, 51 (2002).

[109] C. Galinon *et al.*, Appl. Phys. Lett. **86**, 182502 (2005).

[110] P. Kraus, A. Battacharya, K. Nikolaev, and A. M. Goldman, Mater. Sci. Eng. B **84**, 63 (2001).

[111] J. Y. Gu *et al.*, Phys. Rev. B **66**, 140507 (2002).

[112] E. A. Demler, G. B. Arnold, and M. R. Beasley, Phys. Rev. B **55**, 15174 (1997).

[113] V. T. Petrashov *et al.*, Physica C **352**, 25 (2001).

[114] C. Bell *et al.*, Phys. Rev. B **68**, 144517 (2003).

[115] J. Y. Gu *et al.*, Phys. Rev. Lett. **89**, 267001 (2002).

[116] V. I. Falko, A. F. Volkov, and C. Lambert, Phys. Rev. B **60**, 15394 (1999).

[117] F. Taddei, S. Sanvito, J. H. Jefferson, and C. J. Lambert, Phys. Rev. Lett. **82**, 4938 (1999).

[118] F. Taddei, S. Sanvito, and C. J. Lambert, Phys. Rev. B **63**, 012404 (2000).

[119] N. Ryzhanova *et al.*, J. Magn. Magn. Mater. **226-230**, 750 (2001).

[120] N. Ryzhanova *et al.*, J. Phys.: Condensed Matter **13**, 4001 (2001).

[121] A. C. Reilly *et al.*, J. Magn. Magn. Mater. **195**, 269 (1999).

[122] S. D. Steenwyk *et al.*, J. Magn. Magn. Mater. **170**, L1 (1997).

[123] C. Fierz *et al.*, J. Phys.: Condensed Matter **2**, 9701 (1990).

[124] K. Eid, H. Kurt, W. P. Pratt, Jr., and J. Bass, Phys. Rev. B **70**, 100411 (2004).

[125] K. Eid *et al.*, J. Appl. Phys. **91**, 8102 (2002).

[126] C. Vouille *et al.*, Phys. Rev. B **60**, 6710 (1999).

[127] M. AlHajDarwish, A. Fert, W. P. Pratt, Jr., and J. Bass, J. Appl. Phys. **95**, 6771 (2004).

[128] I. Mertig *et al.*, J. Magn. Magn. Mater. **151**, 363 (1995).

[129] I. A. Campbell and A. Fert, in *Ferromagnetic Materials*, edited by E. P. Wolfarth (North-Holland, Amsterdam, 1982), Vol. 3, p. 747.

[130] X. Waintal, E. B. Myers, P. W. Brouwer, and D. C. Ralph, Phys. Rev. B **62**, 12317 (2000).

[131] M. D. Stiles and A. Zangwill, Phys. Rev. B **66**, 014407 (2002).

[132] S. Zhang, P. M. Levy, and A. Fert, Phys. Rev. Lett. **88**, 236601 (2002).

[133] W. Park *et al.*, J. Appl. Phys. **85**, 4542 (1999).

[134] J. Grollier *et al.*, Appl. Phys. Lett. **78**, 3663 (2001).

[135] F. B. Mancoff and S. E. Russek, IEEE Trans. Magn. **38**, 2853 (2002).

[136] B. Ozyilmaz *et al.*, Phys. Rev. Lett. **91**, 067203 (2003).

[137] M. Covington *et al.*, Phys. Rev. B **69**, 184406 (2004).

[138] W. P. Pratt, Jr. *et al.*, J. Appl. Phys. **79**, 5811 (1996).

[139] H. Kurt, R. Loloee, W. P. Pratt, Jr., and J. Bass, J. Appl. Phys. **97**, 10C706 (2005).

[140] F. J. Jedema, A. T. Filip, and B. J. van Wees, Nature **410**, 345 (2001).

[141] F. J. Albert *et al.*, Phys. Rev. Lett. **89**, 226802 (2002).

[142] N. C. Emley *et al.*, Appl. Phys. Lett. **84**, 4257 (2004).

[143] L. Piraux, S. Dubois, A. Fert, and L. Belliard, Eur. Phys. J. B **4**, 413 (1998).

[144] Q. Yang *et al.*, Phys. Rev. Lett. **72**, 3274 (1994).

[145] R. F. Soohoo, in *Magnetic Thin Films*, edited by F. Seitz (Harper and Row, NY, 1965).

[146] K. Hyomi, A. Murayama, J. Eickmann, and C. M. Falco, J. Magn. Magn. Mater. **198-199**, 378 (1999).

[147] F. Casoli *et al.*, Scripta Materialia **48**, 955 (2003).

[148] C. H. Lee *et al.*, Phys. Rev. B **42**, 1066 (1990).

[149] R. Clarke *et al.*, J. Appl. Phys. **70**, 5775 (1991).

[150] F. Albertini *et al.*, J. Magn. Magn. Mater. **240**, 526 (2002).

[151] L. J. van der Pauw, Philips Tech. Rev. **20**, 220 (1958).

[152] J. Bass, Adv. in Physics **21**, 431 (1972).